Deciphering osteoarthritis disease using multimodal mass spectrometry methodologies

Deciphering osteoarthritis disease using multimodal mass spectrometry methodologies

Maxime Eveque

ISBN: 978-94-6423-146-5
PhD thesis Maastricht University
Deciphering osteoarthritis disease using multimodal mass spectrometry methodologies

The research reported in this dissertation was carried out at Maastricht Multimodal Molecular Imaging Institute (M4I), Universiteitssingel 50, 6229ER, Maastricht, The Netherlands.

Cover design & layout: Maxime Eveque

Printed by: Proefschriftmaken (proefschriftmaken.nl)

Deciphering osteoarthritis disease using multimodal mass spectrometry methodologies

DISSERTATION

To obtain the degree of doctor at Maastricht University,
on the authority of the Rector Magnificus
Prof. dr. Rianne M. Letschert,
in accordance with the decision of the Board of Deans,
to be defended in public
on the 26th of February 2021 at 10 hours

by

Maxime Eveque
Born in Lille, France, on February 8th, 1992

Promotor

Prof. dr. R.M.A. Heeren

Co-Promotors

Dr. B. Cillero-Pastor

Dr. P. J. Emans

Assessment Committee

Prof. dr. M. Poeze, UM (Chairman)

Prof. dr. M. Honing, UM

Prof. dr. T.M. Hackeng, UM

Prof. dr. M.H.B.J. Karperien, UT

Prof. dr. G. Kloppenburg, LUMC

This research was part of the M4I research program financially supported by the Dutch Province of Limburg through the LINK program.

This research was also part of the collaboration between MUMC+ and M4I through MUMC+ institutional grant for clinical collaborative research.

To my parents, sister, brother, niece and grandparents
To my uncle

TABLE OF CONTENTS

CHAPTER 1

General introduction

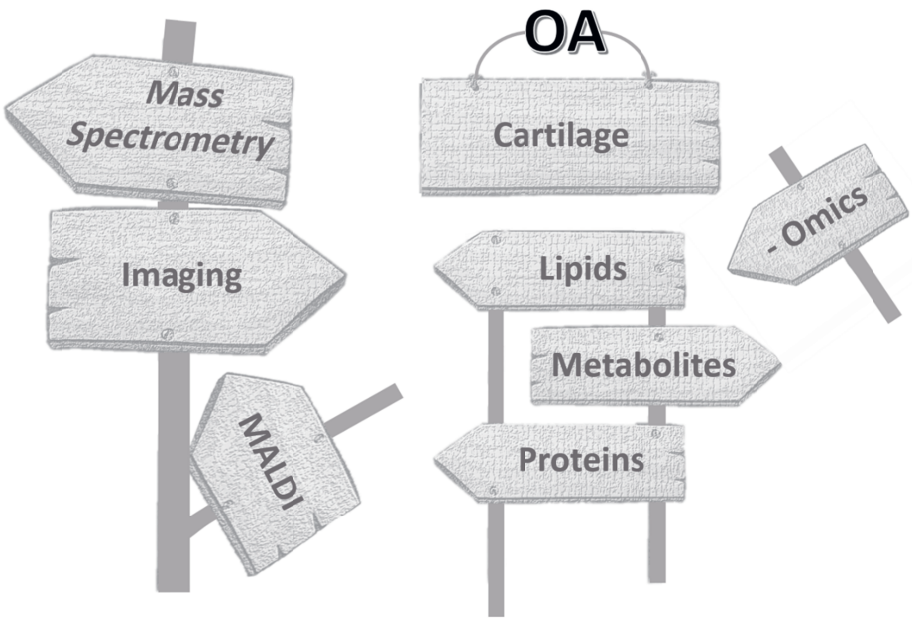

1. General introduction

1.1. Rheumatic diseases

Historically, Hippocrates associated the terms "Rheuma" and "catarrh" with a specific disease-causing process where "the mucus flux", coming from the brain, travelled to various locations in the body such as the entrails and the joints.[1] For the first time, Hippocrates also mentioned "the arthritic pain", one of the common symptoms of rheumatic diseases.

Rheumatic diseases are mainly characterized by pain and loss of motion or flexibility in one or several joints in the body. Within the current classification and response criteria, rheumatic diseases are associated with more than 100 different disorders. Among them, osteoarthritis (OA) is the most prevalent.

OA is characterized by the progressive deterioration of articular cartilage from any joint, but occurs more often in knees, hands, hips, lower back, and neck. OA is the world's oldest known disease, with evidence present in skeletons of dinosaurs.[2] OA is also considered an age-related pathology[3] and its prevalence varies depending on the joint under study and the characteristics of the study population.[4] Many factors contribute to the development of the pathology including lack of exercise, obesity, genetic predisposition, gender, bone density, or any trauma affecting joints, such as post-traumatic OA (PTOA).[5] The multifactorial aspect of the pathology leads to different phenotypes within the OA population. However, all the phenotypes receive similar treatments, regardless of their potential biological differences, which results in inadequate therapy. Therefore, new patient stratification based on phenotypes is needed for personalized therapeutic strategies.

Lately, several models for the classification of these phenotypes have been proposed.[6, 7] In particular, the metabolic syndrome (MetS) phenotype is defined by the role of obesity and by chronic low-grade inflammation, which leads to systemic and local change during OA.[8-10] MetS is a health disorder affecting 10–30% of the worldwide population with a prevalence of 59% in OA patients.[11] MetS is diagnosed when a patient has at least three of the following conditions: i) high blood pressure (≥130/≥85 mm Hg), ii) high blood glucose levels (≥110 mg/dL at fasting glucose), iii) high triglyceride levels (≥150 mg/dL), iv) low HDL-cholesterol (<40 mg/dL in men and <50 mg/dL in women), and v) a large waist circumference (>102 cm in men and >88 cm in women).[12] MetS also increases the risk of developing other diseases such as obesity, type 2 diabetes mellitus (T2DM), hypertension or dyslipidemia.[13,14] In particular, OA and T2DM frequently co-exist, and a higher prevalence of developing OA in T2DM patients has been shown.[15-18] The T2DM disease is characterized by insulin resistance and high blood sugar.[19, 20] Deciphering the molecular

mechanisms underlying the pathological processes of the OA/T2DM phenotype is one of the goals of this thesis.

Since rheumatic disease is a broad and complex disease, the following general introduction will focus exclusively on OA pathology. First, we will describe the knee and the different tissues involved in the structure of the joint. The knee is considered the most commonly affected area by OA[21] and the cartilage from this joint has been the primary tissue used in the research presented in this thesis. Second, we will stress the importance of mass spectrometry technology with a focus on mass spectrometry imaging, which played a pivotal role in this thesis.

The knee joint is constituted of cartilage, synovial membrane, synovial fluid (SF), subchondral bone and Hoffa's fat pad (HFP) tissues:

The cartilage tissue is composed of chondrocyte cells embedded in an extracellular matrix (ECM) mostly composed of collagen and proteoglycans,[22] but also containing other, non-collagenous, proteins and glycoproteins.[23] All these components help to retain water within the ECM to maintain the mechanical properties of the cartilage.[24] Moreover, the cartilage is composed of different layers: the superficial layer, the deep layer and the transitional layer. The superficial layer of the cartilage is in close contact with the synovial fluid and it is the only zone where articular cartilage progenitor cells have been found.[25] The deep layer remains closer to the subchondral bone. The superficial and the deep layers are separated by the transitional layer.

The synovial membrane (or synovium) consists of two layers, the intima and subintima. The intima is a continuous surface-layer of cells, composed of macrophages and synovial fibroblasts that are embedded in a collagen and hyaluronan-matrix.[26] The subintima is an underlying tissue that is composed of blood and lymphatic vessels. These two layers are separated by the intimal surfaces that contain a small amount of fluid. This fluid is usually rich in hyaluronan.[27] The synovial membrane is only found in synovial joints and functions mainly to release the SF.

SF is a hyaluronic acid-rich liquid released by the synovial membrane.[28] It brings nutrients for chondrocyte metabolism in cartilage. SF also lubricates joints by using mostly proteoglycan-4 and hyaluronan.[29] A major component of SF is proteins derived from plasma, although soluble molecules, like growth factors and cytokines are also present.[30, 31]

The subchondral bone is usually the transition zone between calcified cartilage and the rigid skeleton.[32] Cartilage and the rigid skeleton can also meet at a thin interface known as the cement line.[33] The osteochondral junction, where the subchondral bone resides, is not completely understood; however, several studies have demonstrated the involvement of the osteochondral junction in OA disease.[34, 35]

Finally, HFP tissue is an extra synovial structure mainly composed of adipocytes and connective tissue, containing collagen and glycosaminoglycans.[36]

All these joint components described are affected during OA. The disease results mainly in cartilage degeneration, but also includes synovial membrane inflammation and changes in the subchondral bone.[37, 38] Moreover, the inflammation of the synovial membrane leads to an elevated production of SF which produces joint swelling and pain.[39] Finally, the HFP tissue is now recognized to play a role in the pathological process of OA. [40] The involvement of all these tissues makes OA as a complex and heterogeneous disease. The identification of biomarkers, both for diagnosis and prognosis of OA, remains essential to measure the different pathological processes linked to the disease. Nowadays, different –omic approaches (transcriptomics, lipidomics, metabolomics, proteomics and glycomics) are employed to better understand the different pathological processes linked to OA and to improve treatment of the pathology based on the associated phenotypes we previously discussed.

1.2. Mass spectrometry as a multimodal approach

Mass spectrometry (MS) is an analytical technology used in many -omics based studies.[41] MS is a powerful, label-free analytical tool that can detect biomolecules (e.g., lipids, peptides, proteins, metabolites, and glycans) and can be used for many applications.[42-44] A mass spectrometer contains three main elements: the ionization source, the analyzer, and the detector. The ionization source enables the desorption and ionization of analytes from the surface and transforms them into the gas phase as ions. These ions are then separated based on their mass-to-charge ratios (*m/z*) using an electric or magnetic field from one of the many types of mass analyzers. The detector will produce a signal in response to these ions. This signal can be transformed into a mass spectrum, which displays the relative abundance of detected ions as a function of their *m/z* values. MS provides different capabilities in terms of accuracy, sensitivity and high throughput depending on different instrument configurations.[45]

Mass spectrometry imaging (MSI) is one of the major methodological developments in the mass spectrometry field. MSI investigates the distribution of a wide variety of biomolecules through *in-situ* analysis of tissue sections.[46, 47] MSI analysis of biological samples became possible with the development of soft ionization techniques such as matrix assisted laser desorption/ionization (MALDI) and electrospray ionization (ESI). The first MALDI-MSI experiment was performed in the late 1990s.[47] Since then, MALDI-MSI has been established as a useful imaging tool in the clinical field, where the number of applications is still increasing.

The ionization technique used in an MSI experiment also needs to be adapted according to the tissue type, the required spatial resolution and the targeted molecular class.[48] For this purpose, MALDI remains the most versatile MSI technique since it allows the detection of a wide range of molecular classes and can be used for high spatial resolution experiments.[49, 50] In a traditional MALDI-MSI experiment, a sample, often a tissue section, is placed on a glass slide or conductive surface. Then, a UV-absorbing matrix is applied to the sample surface to facilitate the desorption and ionization process. The UV laser is fired at predefined positions, or pixels, of the tissue. A mass spectrum is then collected at each of these measured positions/pixels on the sample. MALDI-MSI enables the selection of particular molecules or *m/z* peaks of interest to plot in a 2D heat map. These plots and heat maps display the distributions and relative intensities of molecules of interest within the tissue.

1.3. Mass spectrometry imaging: applications to knee OA disease

The application of MSI in the rheumatology field is recent, with only a few reports published so far. In the context of OA disease, MALDI also remains the most applicable ionization method used for imaging experiments, which is mainly due to the molecular composition of OA-affected tissues. MALDI-MSI has been applied to chondrocytes[51] and mesenchymal stem cells[52] to characterize the lipid profiles and lipid spatial distribution. Moreover, MALDI-MSI has been applied to the synovial membrane to spatially-resolve the protein/peptide distribution[53] and on subchondral bone to image N-glycans.[54] MALDI-MSI is also applied to cartilage, which is helpful in distinguishing superficial and deep layers of the tissue. Another study demonstrated a specific distribution of fibronectin and cartilage oligomeric matrix proteins in the deep layer of OA human cartilage samples.[55] A study conducted by Cillero-Pastor et al. using another imaging methodology such as time-of-flight (TOF) secondary ion mass spectrometry (SIMS), also demonstrated that lipids such as cholesterol accumulate in the superficial layer of cartilage during OA.[56] Cholesterol has a regulating role in growth plate chondrogenesis and skeletal development.[57]

1.4. Scope of the thesis

The work described in this thesis focuses on the development of mass spectrometry-based approaches to answer biological questions related to the OA pathology and subtyping.

In **chapter 2**, we discussed the general principles of the bottom-up proteomics approach. We reviewed the recent studies applied to different tissues involved in OA disease based on this approach and provide new methods which are not fully applied by the OA community yet. We finally discussed the spatially resolved proteomics approach because we believe that the spatial distribution of the proteins within the tissues is critical to understanding OA pathology.

The spatial distribution of endogenous metabolites has never been resolved in OA cartilage tissue. That is the main reason why in **chapter 3**, we developed a sensitive approach to detect endogenous metabolites on human cartilage by MALDI-MSI. We showed that heat stabilization performed immediately after total knee replacement surgery is a critical point, mainly by slowing-down the degradation of metabolites. This chapter also described the optimized method we used to reveal a higher presence of endogenous metabolites in the superficial layer of the human cartilage tissue.

In **chapter 4**, we described a multimodal MS approach which combined both label-free proteomics and MALDI-MSI methodologies. Our protocol was applied to samples of human cartilage and revealed distinct protein and lipid signatures between OA/T2DM^{-} and OA/T2DM^{+} phenotypes. The MALDI-MSI approach also demonstrated lipid differences between the superficial and deep layers of the cartilage. Together, these results suggested the need to consider different OA phenotypes in order to provide more personalized therapies.

The label-free proteomics strategy was combined with a transcriptomic approach in **chapter 5**, where we studied the role of the Sox9 gene during the early phase of chondrogenesis process in ATDC5 cells. The data presented show a connection between early Sox9 gene expression and ribosome biogenesis, in particular in terms of protein translational capacity.

Finally, the valorization chapter (**chapter 6**) describes the main outcomes of this thesis that could be addressed in the future to further impact the field of the OA disease, with a particular focus on patient care.

CHAPTER 2

Spatially resolved proteomics in osteoarthritis: state of the art and new perspectives

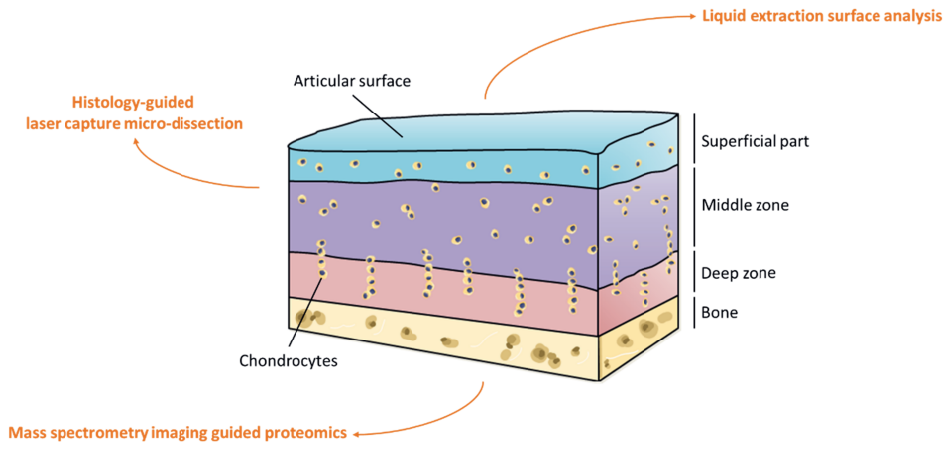

Adapted from:

Spatially resolved proteomics in osteoarthritis: State of the art and new perspectives

Eveque-Mourroux MR*, Rocha B*, Barré FPY, Heeren RMA, Cillero-Pastor B

Journal of Proteomics. **2020**, 215, 103637

2. Spatially resolved proteomics in osteoarthritis human research: state of the art and new perspectives

2.1. Abstract

Osteoarthritis (OA) is one of the most common diseases worldwide caused by chronic degeneration of the joints. Its high prevalence and the involvement of several tissues define OA as a highly heterogeneous disease. New biological markers to evaluate the progression of the pathology and improve its prognosis are needed. Among all the different -omic strategies applied to OA, solution phase bottom-up proteomics has made an extensive contribution to the field of biomarker research. However, new technologies for protein analysis should be considered for a better understanding of the disease.

This review focuses on complementary proteomic methodologies and new technologies for translational research of OA and other rheumatic pathologies, especially mass spectrometry imaging and protein imaging methods not applied by the OA community yet.

2.2. Introduction

Osteoarthritis (OA) is an age-related joint disease and the most common rheumatic disease affecting 10 to 20% of people over 50 years old. [58] The disease is characterized by an alteration of the whole joint structure, including progressive cartilage degradation [22-24], synovial membrane inflammation [26, 27], and changes to the subchondral bone. [32-35] Moreover, the inflammation of the synovial membrane leads to an elevated production of synovial fluid (SF) which produces joint swelling and pain. [30, 31] Due to the complexity of the joints, OA remains thereby a heterogeneous disease.

Nowadays, different –omic strategies are employed for discovery, characterization and quantification of biomarkers in order to improve prognosis and diagnosis. [59, 60] In particular, proteomic strategies are increasingly applied to OA research and OA biomarker discovery. [61-63]

Proteins fulfill essential functions in cells. These include enzymatic reactions to produce energy, immunological response and/or cellular communication. The panel of expressed proteins in a given cell type or organism defines the term "proteome". Contrary to the genome which is more static, the proteome is dynamic, making the comprehensive analysis more challenging. [64] Proteomic technologies focus on the

identification, quantification and/or characterization of proteins that are present in a sample using mass spectrometry (MS). [65] Proteomics provide information on protein identity and sequence, protein abundance, protein interactions, post-translational modifications (PTMs) and protein turnover. Although several methodologies are now available in the field, the bottom-up approach has been widely described and is now the most frequently used technique that allows high throughput analysis of complex samples. [66-68] The bottom-up approach relies on protein extraction prior separation using different methods such as isoelectric focusing (IEF) and sodium dodecyl sulfate polyacrylamide gel electrophoresis (SDS-PAGE). However, gel-free approaches are nowadays more frequently used. [69, 70] These approaches enable the reduction of the sample complexity and increase the proteome coverage. Proteins are then chemically processed by a reduction/alkylation step, before being enzymatically digested (commonly by trypsin [69] or LysC/trypsin [70]) to finally get peptides. The peptides are subsequently separated by reversed-phase liquid chromatography (RP-LC) before entering the mass spectrometer. Tandem mass spectra (MS/MS or MS2) are finally matched against *in silico* spectra by a search engine, which assigns peptide sequences and infers the corresponding proteins. [68]

As example of recent studies, a pilot analysis conducted by Folkesson et al. investigated the difference in protein expression on cartilage between the tibial condyle and the meniscus from human knees. [71] The results showed similar subset of differentially abundant proteins but with different fold changes depending on the analytical method that was employed. For instance, dermatopontin has been quantified with a 15-fold change in the meniscus using data independent acquisition (DIA), whereas a 29-fold change was reported using data dependent acquisition (DDA). Another study performed on SF from OA patients identified potential biomarkers and drug targets such as the complement C1r and the dickkopf-related protein 2. [72] Proteomics has also been used on SW1353 chondrocyte-like cells to explore the effects and mechanisms of Astragaloside IV (ASG-IV), a reported drug which promotes rapid proliferation of these cells. Quantitative results suggested that extracellular matrix (ECM) signaling pathways were modulated by ASG-IV, indicating its key role in OA chondrocyte apoptosis. [73] Another study performed on the chondrocyte secretome reported the relationship between smoking and the development of OA. Nineteen proteins have been found to be altered by nicotine including several cytokines and proteases. [74]

Most of the bottom-up work comprehends the analysis of peptides with a mass/charge ratio (*m/z*) below 3 kDa, due to the use of trypsin as a gold standard for digestion. Although this configuration is well-established, most of the PTMs and proteoforms are not preserved. [75-77] Consequently, other approaches may be

considered. Middle-down and top-down strategies are two other techniques used in the proteomics field. The middle-down approach focuses on the analysis of middle range peptides with a molecular weight comprised between 3 kDa and 10 kDa [69], thanks to the use of other enzymes. On the other hand, the top-down approach employs MS to study intact proteins and their proteoforms. [78, 79] In the context of OA disease, both methods could be considered to improve the sequence coverage of OA-related proteins such as collagens or to study specific PTMs such as phosphorylation. [80]

The above-mentioned proteomic approaches have been also applied to study the interactome. The proteome becomes more complex when considering all the possible networks of physical and functional interactions between proteins but also with other biomolecules such as DNA, RNA, lipids and metabolites. [81-85] Protein cross-linking coupled with mass spectrometry (XL-MS) provides a platform to freeze the transient interactions through the formation of covalent bonds. In this way XL-MS provides a vital insight into both the structure and organization of proteins. [86]

These previously described approaches allow protein analysis from whole tissue lysates or cell extracts. However, due to the importance of the cross-talk of the different joint tissues, the spatial location of proteins is critical, especially when tissues contain regions with diverse cell subpopulations. The study of tissue protein distribution defines a new area namely spatially resolved proteomics. In this review, we discuss how spatially resolved proteomics can be employed in the field of rheumatic pathologies and especially in OA.

2.3. Mass Spectrometry imaging

Mass spectrometry imaging (MSI) is a label free technology that allows the multiplex analysis of a broad variety of analytes in tissue sections such as proteins, peptides, lipids, drugs, and metabolites. [87] Usually, MSI spatial resolution ranges from nano- to micrometers depending primarily on the type of ionization technique employed. [88] This approach can reliably indicate the specific molecular location within a tissue. MSI records a mass spectrum at every measured position (x and y coordinates) on the sample. Consequently, each mass spectrum reflects the local molecular composition at every coordinate. The *m/z* of interest can be then selected and plotted in a heat map to display their respective distribution and relative intensity. The tissue sections can optionally be stained after the imaging experiment with hematoxylin/eosin, alcian blue, or immunostained [89] before co-registration with the MSI data.

2.3.1 Matrix-assisted laser desorption/ionization mass spectrometry imaging of joint-derived tissues

Among all the ionization techniques, matrix-assisted laser desorption/ionization (MALDI) is the most applicable method to the rheumatology field due to the molecular composition of OA-affected tissues. MALDI-based ionization imaging is the most versatile MSI platform that allows the *in-situ* detection of a large number of peptides and proteins.
In a general MALDI-MSI workflow, tissue sections are placed on regular microscope or conductive glass slides and coated with a suitable matrix solution that assists in desorption and ionization of the analytes. During the experiment, the tissue is locally irradiated by a laser beam generating a mass spectrum for each measured position.

MALDI-MSI has been applied in the past years to investigate joint tissues in rheumatic disorders. Mainly, specific MALDI-MSI protocols have been developed to explore the differences in the composition and distribution of peptides between healthy and OA tissues. In this workflow, trypsin is deposited directly on the tissue surface after performing washing steps and before matrix application. Once the peptide map is generated, direct MS/MS fragmentation of the detected peptides is carried out to identify the corresponding protein. This method offers the advantage of identifying proteins from tissues without separation and homogenization, while preserving the information on their spatial distribution. [90, 91] Using this methodology, the spatial distribution of well-known OA related peptides/proteins in cartilage has been previously reported. In this work, fibronectin peptides displayed a stronger intensity in OA cartilage compared to control tissues and were found to be more abundant in the deep areas of the cartilage. [55] Moreover, cartilage oligomeric matrix protein (COMP) peptides showed a similar spatial distribution as fibronectin. MALDI-MSI has also been employed to investigate the distribution of ECM proteins in young, old and OA equine cartilage. [92] In this work, peptides corresponding to COMP showed a higher expression in old equine samples compared to young and OA cartilage, whereas collectin-43 protein was specific to young cartilage.

Recent advances in MS instrumentation have allowed improvements in terms of mass resolution, spatial resolution and acquisition time (Figure 2.1). As shown in the figure, high mass resolution mass spectrometry is required to differentiate between peptide ions (*m/z* 1004.4503 and *m/z* 1004.4817) that possess a different spatial distribution.

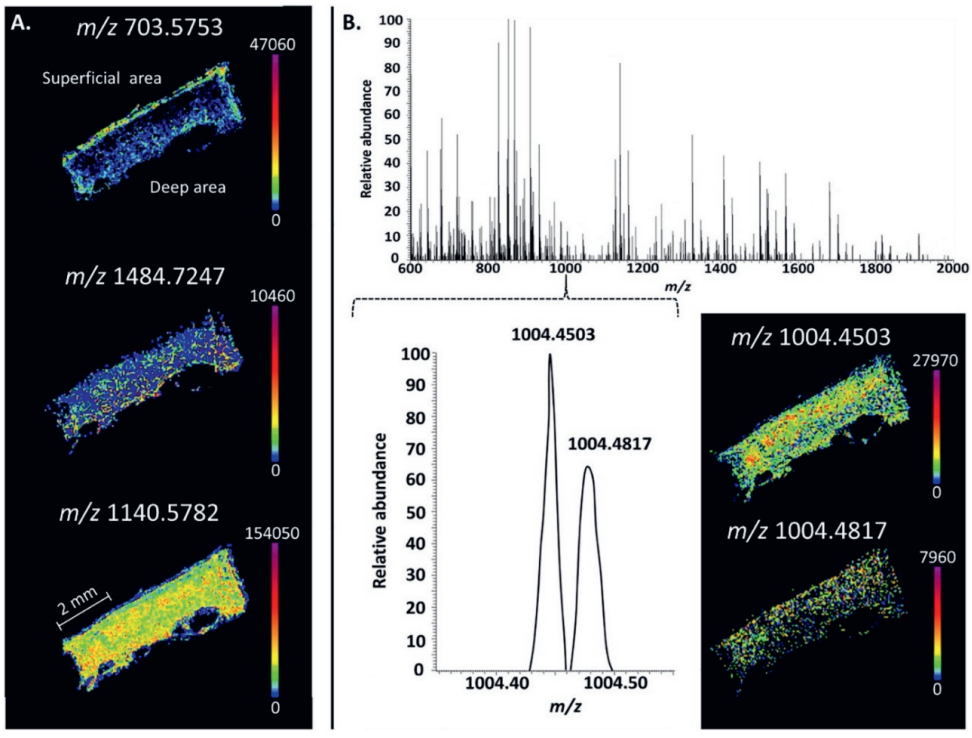

Figure 2.1. Molecular distribution in human knee cartilage acquired at 30 µm on a MALDI-Orbitrap mass spectrometer. (**A**) Positive ion-mode images show the spatial distribution of peptides (*m/z* 1484.7247 and *m/z* 1140.5782). The color scale indicates the relative intensity. The *m/z* 1484.7247 is mainly distributed in the deep area of the cartilage while the *m/z* 1140.5782 shows homogeneous distribution within the tissue. The distribution of a lipid (*m/z* 703.5753) is also displayed with a specific distribution in the superficial area of the cartilage and has been identified as sphingomyelin 34:1 by tandem mass spectrometry. (**B**) Average peptide mass spectrum of human cartilage. MALDI-enabled Orbitrap Elite spectra showing the differentiation of two peptide ions (*m/z* 1004.4503 and *m/z* 1004.4817) with differential spatial distribution.

Differences in the composition and distribution of intact proteins have been investigated in synovial tissues with MALDI-MSI. [93] In this work, synovial samples of patients with rheumatoid arthritis (RA) and OA were compared and specific proteins were correlated with disease-associated synovial changes. Among them, defensins and S100 proteins were located in both synovial membrane layers, the subintima and the intima, and displayed a higher abundance in RA samples compared to OA. On the other hand, thymosin beta truncated proteins were differentially distributed across tissue layers, showing a higher intensity in the sublining layer of RA patients. Moreover, protein thymosin beta 4 was predominantly observed in the hypertrophic lining layer of OA and RA samples. In

this study, MALDI-MSI was applied for the first time to synovial tissue providing tissue-specific protein biomarker candidates of patients with RA and OA.

Another MSI based-study performed on synovial membrane described a specific protein profile discriminating control from OA synovium tissues. [53] Interestingly, fibronectin-related peptides were mainly located in hypertrophic areas of OA synovial membranes, which are characterized by an increased tissue inflammation. As stated above, these peptides were also previously detected by MSI in OA cartilage. These findings suggest that fibronectin is a common feature in OA tissues (cartilage and synovium) and could be used as a potential biomarker to discriminate between healthy and OA related tissues using MALDI-MSI.

Spatial peptide alterations have been recently reported in other musculoskeletal diseases by MSI such as in severely injured skeletal muscles in response to transplantation of autologous bone marrow mesenchymal stromal cells (MSC-TX). [94] In this work, the pathophysiological muscle areas in primary traumatized and adjacent areas were analyzed and compared pointing out differential peptide distributions between groups. These results also demonstrated the capability of MALDI-MSI to unravel novel regions not previously reported by histology.

Apart from trypsin, other enzymes can be applied directly on tissue. For instance, tissue sections can be treated with N-glycosidase F (PNGase F), which releases N-linked glycans, or N-glycans, from glycoproteins. [95] The analysis of N-glycans is especially relevant in OA since these analytes are associated with the progression of the disease. [96] In fact, MALDI-MSI has been recently applied to spatially characterize the N-glycome in cartilage and subchondral bone of knee OA patients. [54] In this work, approximately 40 N-glycan structures were identified from cartilage and subchondral bone proteins by MALDI-MSI. Among them, high mannose N-glycans showed differential spatial distribution through the OA tissues. Particularly, $(Man)_3$ + $(Man)_3$ $(GlcNAc)_2$ was found increased in cartilage compared to subchondral bone. In addition, OA patients with different bone marrow lesion stages were discriminated according to the $(NeuAc)_2$ $(Hex)_2$ $(HexNAc)_2$+ $(Man)_3$ $(GlcNAc)_2$ profiles. The use of PNGase F and trypsin in combination with MSI can also increase the number of protein identifications while maintaining the spatial information. As an example, MALDI-MSI analysis of both N-linked glycans and proteolytic peptides from the same tissue section has been recently described. In this work, cancer tissue sections are sequentially digested using a combination of PNGase and trypsin enzymes. [97]

Collagens are highly abundant proteins in the ECM of cartilage. As well as proteoglycans, collagens are key molecules for the maintenance of the ECM architecture facilitating chondrocyte-matrix signaling. The high degree of cross-linking between ECM and collagens blocks the access of trypsin to these proteins, so other relevant proteins cannot be easily analyzed and localized in cartilage by proteomic methods. [66] The combination of trypsin with other enzymes such as collagenases, can improve the extraction and detection of these proteins. A cocktail of collagenase 3 and matrix metalloproteinase 12 has been recently employed reporting the spatial localization of collagens and other ECM proteins such as elastin in different human tissues (liver, hepatocellular carcinoma, colorectal cancer and aortic valves tissues) by MSI, but not yet in joint tissues. [98]

These studies taken all together demonstrate that MALDI-MSI is a novel technology to investigate joint-derived tissues providing specific peptide or glycan markers of OA disease. Nevertheless, the lack of direct protein identification when using trypsin or other enzymes in MALDI-MSI workflow is still a challenge. Therefore, different approaches are needed to overcome and improve the methodology (Figure 2.2). In the following sections, we highlight the latest developments that, in combination with MSI (Figure 2.2A), can be used to improve protein detection and identification in the OA field.

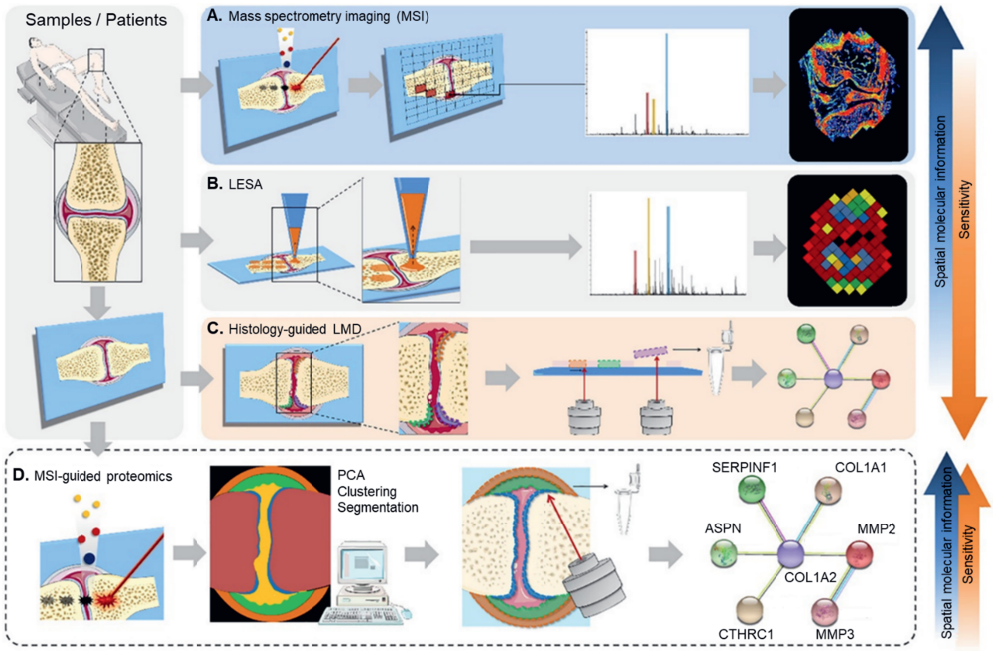

Figure 2.2. ***Ex-vivo*** **spatially-resolved proteomics applied to OA research.** (**A**) Mass spectrometry imaging (MSI) workflow. (**B**) Liquid Extraction Surface Analysis (LESA) workflow. (**C**) Histology-guided Laser Micro-Dissection (LMD) workflow: High spatial molecular information (≤10 µm) can be reached by MSI but with limited protein sensitivity. LESA or LMD technologies can achieve a better sensitivity but low spatial information. (**D**) MSI-guided proteomics workflow: In order to take advantage of the spatial molecular information as well as the sensitivity, MSI approach can be combined with LMD.

2.4. Liquid extraction surface analysis

Liquid Extraction Surface Analysis (LESA) involves the deposition of a droplet of solvent from a pipette tip to the surface. The solvent contacts the surface forming a liquid microjunction between the surface and the pipette tip allowing the analyte extraction from the tissue. Finally, the sample is re-aspirated, introduced into the mass spectrometer and ionized *via* ESI (Figure 2.2B) or transferred for LC-MS analysis. The technique can be coupled to bottom-up proteomics when introducing a proteolytic digestion step. [99, 100] As an example, Quanico et al. used a MALDI MSI-guided approach to identify regions of anatomical interest. Using adjacent sections, these tissue regions were analyzed by LESA coupled to LC-MS/MS to improve sensitivity for protein identification. [100]

The combination of MALDI-MSI and LC-based proteomics is an alternative to enhance the protein identification rates. In this approach, a tissue section is analyzed by MSI while a consecutive section is homogenized and analyzed by LC-MS/MS. LC-MS/MS identification of peptides from parallel tissue sections allows the generation of specific peptide databases that benefit the identification of proteins in an imaging experiment. Therefore, different *on-tissue* protocols combined with bottom-up proteomics could be extremely useful to improve the detection and location of ECM proteins. However, a drawback of using consecutive sections here is that a full tissue extract is analyzed losing the specific signature of each region of interest (ROI) defined by MSI.

2.5. Histology-guided laser capture micro-dissection

Laser capture micro-dissection (LMD) was initially used to isolate cells or ROIs from tissues after staining (Figure 2.2C). [101] Among other methodologies, the samples can be then analyzed by LC-based proteomics. [102-104] A recent study conducted by Ezzoukhry, Z et al. demonstrated the possibility to perform fluorescence guided LMD using a modified cell line emitting red fluorescence. [105] In this case, the same tissue section can be used to correlate both histology and proteomics. LMD technology has been used to collect cartilage matrix from the territorial and

interterritorial regions at different depths (superficial, middle and deep) of cartilage derived from healthy and OA knees and hips. The proteomics results demonstrated that the degradation of the interterritorial regions is one of the main consequences of the disease, providing therefore direct evidence for dynamic remodeling of cartilage. [106]

2.6. MSI-guided proteomics

Recently, a new approach has been developed combining both MSI analysis and protein identification on the same tissue section (Figure 2.2D). In this strategy, specific ROIs identified by MALDI-MSI can be excised from the same tissue using LMD and then subjected to LC-MS/MS.[107, 108] Alberts et al. have used this combination of MALDI-MSI with LMD-based microproteomics to investigate heterogeneity in breast tumors. [109] In this study, MALDI-MSI revealed differential protein signatures that discriminated heterogeneous regions within tumors. Each ROI was then isolated using LMD, subjected to trypsin digestion and analyzed by LC-MS/MS reporting >3000 proteins per region. This method could be applied to study cartilage heterogeneity, in order to gain more insight into regions with different proteomic profiles highlighted by MSI.

2.7. Mass cytometry and multiplexed ion beam imaging as targeted spatially-resolved proteomics

Imaging mass cytometry (IMC, or also called CyTOF) and multiplexed ion beam imaging (MIBI) are two new imaging methods that have been recently introduced in the biomedical field (Figure 2.3). [110] In IMC, different antibodies, selected to target specific proteins or protein modifications, are tagged with metal isotopes and used as reporters. Then, tissue samples are simultaneously stained with a maximum of 32 metal-labeled antibodies, and the isotopes are visualized using MS. The two methods differ in how these tags are liberated from the sample, ionized and detected. In IMC, the UV laser ablates the tissue spot by spot, and the generated ions are transferred in a gas stream (usually a mixture of argon and helium) into the CyTOF mass spectrometer. The laser desorbed material is transferred to an inductively coupled plasma (ICP) ion source where the molecules are ionized. The metal isotope content and, therefore, protein expression and distributions, are then determined in the TOF mass analyzer. The method has been fully applied for cancer studies. [111, 112] On the other hand, in MIBI, secondary ion mass spectrometry is used to image metal isotopes. In this case, the tissue sample is incubated with different metal-labeled antibodies simultaneously. A primary (oxygen) ion beam is employed to raster the tissue surface to generate secondary ions together with the metal isotopes that were

bound to the antibodies. Then, these ions are analyzed in a magnetic sector mass analyzer to determine metal isotope abundance in the tissue.[113] Recently, MIBI has been used to image breast tumor formalin-fixed, paraffin-embedded tissue sections with different immunophenotypes. [113]

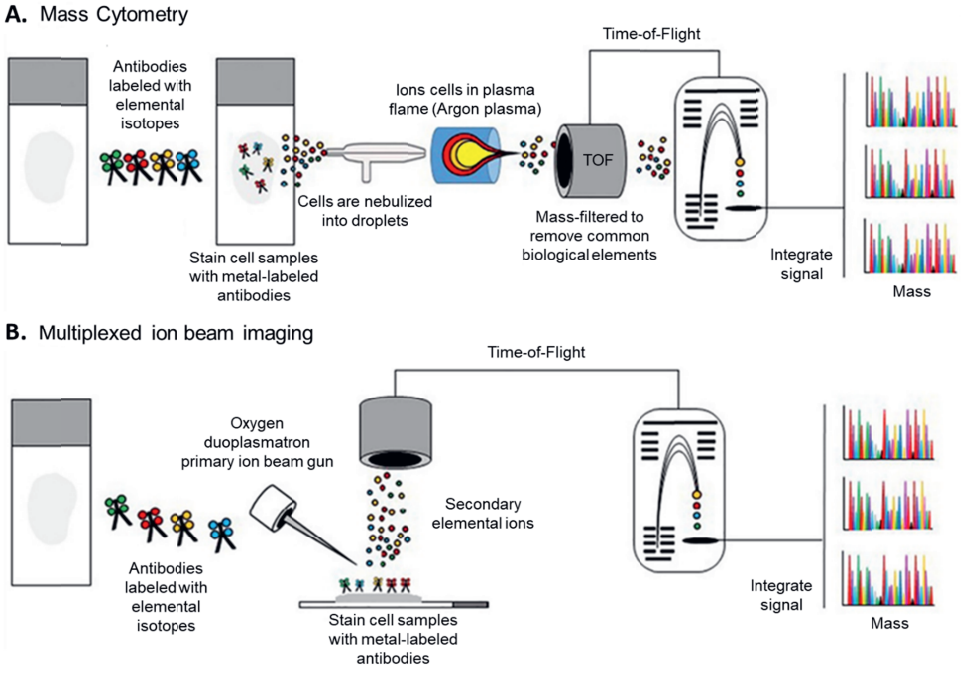

Figure 2.3. Representative workflows of imaging mass cytometry (IMC) and multiplexed ion beam imaging (MIBI). (**A**) IMC experimental procedure. Tissue sections are incubated with metal-chelated antibodies targeted against proteins of interest using IHC protocols. Then, tissue samples are positioned in a laser ablation chamber. The tissue is ablated and the resulting molecules are transported by an inductively-coupled argon plasma into the CyTOF for mass cytometry analysis. The measured isotope signals are plotted using the coordinates of each single laser shot, and a multidimensional tissue image is generated allowing the investigation of different cell subpopulations. (**B**) Similar to IMC, in MIBI samples are incubated with antibodies tagged with isotopically pure elemental metal reporters. The samples are then rasterized with an oxygen ion beam that sputters the antibody-specific metal isotopes from the sample surface as secondary ions, which are measured and quantified by a TOF mass spectrometer. A mass spectrum is recorded for each physical pixel in the tissue, representing the abundance of the antigens in that location. Reprinted from [110].

Both imaging technologies provide spatially resolved multiple protein detection and at the same time overcome some of the drawbacks of chromogenic or fluorescence detection methods. A recent review by Bodenmiller compares the imaging characteristics of IMC and MIBI to those of immunofluorescence, in terms of

sensitivity, resolution, complexity, and throughput. [114] For instance, there is no background signal due to autofluorescence, there are no matrix effects and neither secondary labeling nor amplification steps are required as is often used in immunohistochemistry. Additionally, both approaches have a wider dynamic range compared to immunofluorescence. IMC and MIBI can be combined with other complementary approaches such as MALDI-MSI data to have a more comprehensive view of different tissue components.

One example of the utility of mass cytometry in OA research is illustrated by Paleja and collaborators in a study where CyTOF is employed in combination with next generation RNA-sequencing to immunophenotype the peripheral knee joint fluid and to identify pathways involved in the pathogenesis of the OA disease. [115] Recently, the potential of CyTOF to enhance the discovery of cellular biomarkers for rheumatoid arthritis has also been illustrated. [116]

2.8. Conclusions and future perspectives

Proteomic approaches are widely used and should be still considered to discover, quantify and characterize biomarkers due to their well-established capabilities. In the meantime, complementary technologies that retain the spatial information have rapidly evolved and already demonstrated their importance in the field. Spatially resolved proteomic approaches constitute a useful tool to reveal molecular key interactions and the interplay among different joint tissues. Particularly, MSI provides an ideal platform to reveal intra-tissue heterogeneity and precisely describe the spatial characteristics of pathophysiological protein changes in OA tissues including cartilage and synovium, as we outlined in this review. Moreover, MSI might constitute an alternative to measure protein PTMs, such as glycosylation, phosphorylation or other modifications affecting proteins such as histones. [117] As we stated above, an optimum combination of MSI techniques with further development of different methodologies is required to overcome the existing challenges for protein identification. Multimodal (imaging) approaches offer new opportunities to tackle these challenges and provide a better insight on the molecular mechanisms that lead to OA and other rheumatic pathologies.

Acknowledgements

This work has been performed as part of the M4I research program that was financially supported by the Dutch Province of Limburg through the "LINK" program and by the MUMC+ institutional grant for clinical collaborative research.

CHAPTER 3

Spatially resolved endogenous improved metabolite detection in human osteoarthritis cartilage by matrix assisted laser desorption ionization mass spectrometry imaging

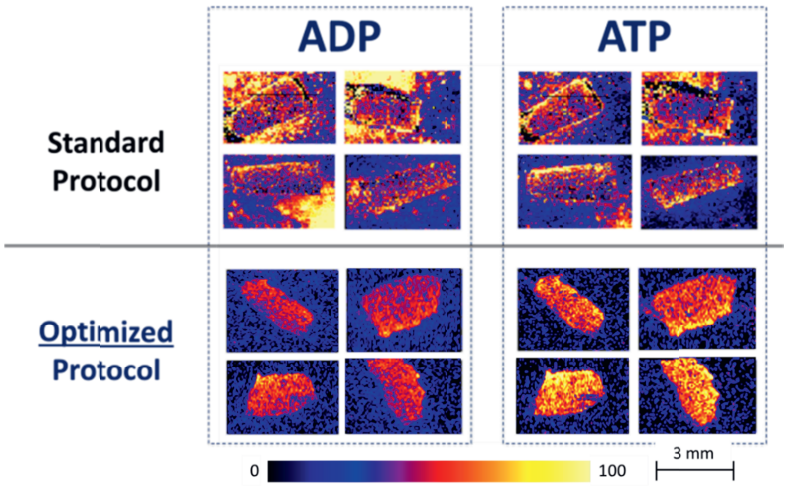

Adapted from:

Spatially resolved endogenous improved metabolite detection in human osteoarthritis cartilage by matrix assisted laser desorption ionization mass spectrometry imaging

Eveque-Mourroux MR, Emans PJ, Zautsen RRM, Boonen A, Heeren RMA, Cillero-Pastor B

Analyst. **2019**, 144, 5953-5958

3. Spatially resolved endogenous improved metabolite detection in human osteoarthritis cartilage by matrix assisted laser desorption ionization mass spectrometry imaging

3.1. Abstract

Osteoarthritis (OA) is one of the most common musculoskeletal diseases, characterized by the progressive deterioration of articular cartilage. Although the disease has been well studied in the past few years, the endogenous metabolic composition and more importantly, the spatial information of these molecules in cartilage, is still poorly understood.

Matrix-assisted laser desorption/ionization (MALDI) mass spectrometry imaging (MSI) has been previously used for the investigation of the bimolecular distribution of proteins and lipids through the *in situ* analysis of cartilage tissue sections. MALDI-MSI as a tool to detect metabolites remains challenging, as these species are low abundant and degrade rapidly.

In this work, we present a complete methodology, from sample preparation to data analysis for the detection of endogenous metabolites on cartilage by MSI. Our results demonstrate for the first time the ability to detect small molecules in fragile, challenging tissues through an optimized protocol, and render MSI as a tool towards a better understanding of OA.

3.2. Introduction

Osteoarthritis (OA) is the most common form of arthritis and is mainly characterized by the progressive deterioration of articular cartilage. [118-120] The disease is also combined with structural changes to the entire joint, including the synovium[121], the meniscus (for the knee)[122], the periarticular ligaments [123] and the subchondral bone.[124] Many factors contribute to the complexity and heterogeneity of the disease. Genetic predisposition, trauma, mechanical loading and lifestyle have an impact on the various molecular pathways that define loadbearing and regenerative capacity of cartilage. It is this heterogeneity that needs the development of targeted personalized medicine for the treatment of OA.[125] Classical approaches such as genomics, metabolomics or proteomics still remain essential to better understand the disease.[126] However, these approaches require whole cartilage extracts and therefore they do not provide any spatial information of the biomolecules within the different layers of the tissue. One way to overcome this drawback is

to use matrix-assisted laser desorption/ionization (MALDI) mass spectrometry imaging (MSI) technology.

MALDI-MSI allows for the investigation of the biomolecular distribution of proteins, lipids or metabolites through the analysis of a variety of tissue sections.[46, 47] For cartilage, studies have been conducted on lipids[52, 127] and peptides.[53, 55, 92, 128] Nevertheless, the endogenous metabolic composition and more importantly the spatial information of these compounds have never been described. Amongst the matrices for metabolite detection, N-(1-naphthyl) ethylenediamine dihydrochloride (NEDC), 1,5-Diaminonapthalene (DAN) and 9-Aminoacridine (9AA) are the most commonly used in the field of MSI.[129, 130] These matrices exhibit very few matrix-related interferences in the low-mass range, which remains advantageous for the simultaneous detection of a variety of cellular metabolites in negative ion mode such as adenosine tri/di/mono/phosphate compounds.[131-133] MALDI-MSI applied to metabolites still remains challenging, especially due to the low abundance of these molecular species and their fast degradation. In addition, the low number of chondrocytes in the avascular, collagen rich extracellular matrix from cartilage tissue increases the difficulty to detect these compounds. As a consequence, an extensive sample preparation optimization i) to avoid tissue degradation as much as possible and ii) to increase extraction and detection of molecular signals by MALDI-MSI is required. Methods such as microwave irradiation[134, 135] and freeze-blowing[136] have been used in studies to prevent enzymatic tissue degradation.[137] One alternative to these methods is the stabilizor system, a device able to preserve proteins[138] or the phosphorylation state [139] for tissue-based proteomic studies with a heat stabilization process. More interestingly, approaches using this technology have been recently applied to preserve amino neurotransmitters[140] or metabolites[141] in MSI experiments on soft tissues. The application of this technology on cartilage can be combined with an optimized MALDI-MSI protocol in order to improve the detection of metabolites. However, protocol optimization remains time-consuming, especially in MALDI-MSI experiments, and can lead to ambiguous results if the important parameters are not well established. One way to efficiently optimize a protocol is to use a statistical design of experiment approach.[142-144] This approach reduces the number of experiments needed for protocol optimization and allows researchers to evaluate the influence of several parameters at once.

In this study, we demonstrated the possibility to extract metabolites from cartilage using 9AA matrix for the first time. These metabolites could be

especially meaningful to assess the disease state of cartilage. The first experiments enabled us to evaluate the capabilities of the stabilizor system to permanently prevent biological changes from the moment of sampling. Then, a statistical design of experiments software was used to optimize the matrix deposition parameters in the MALDI-MSI workflow, in order to increase the detection of metabolites while retaining their spatial distribution. Finally, optimized imaging experiments were executed, revealing metabolite information from cartilage tissue that could previously not be retrieved.

3.3. Materials and methods

Sample preparation

The Maastricht University Medical Centre institutional policy on the use of residual human surgical material states that no informed consent is needed in the case of residual surgical material. Human OA cartilage was obtained from three OA patients undergoing total knee joint replacement. Unwounded cartilage explants of 8*8mm were either heat stabilized by a stabilizor system (Denator, Uppsala) before freezing or immediately snap frozen and stored at -80°C. Snap-frozen tissues were sectioned at 12 µm thickness with a cryostat (Leica Microsystems, Wetzlar) at -20°C and thaw mounted on cleaned indium tin oxide (ITO) glass slides (Delta Technologies, CO, USA).

MALDI-MS profiling

Ten µL of 9AA matrix (Sigma-Aldrich, Zwijndrecht, The Netherlands) was used (7 mg/mL in 70% Ethanol) for the extraction of metabolites from cartilage sections and analyzed in duplicate by MALDI-MS in negative ion mode. Norharmane matrix (Sigma-Aldrich) at 7 mg/mL in chloroform/methanol (2:1, (v/v)) was used for lipid analysis in negative ion mode.

Metabolite analysis was performed using a MALDI-FT-ICR-MS instrument (SolariX, Bruker Daltonik GmbH, Bremen, Germany) at 300-600 *m/z* with 230 laser shots at a laser repetition frequency of 2000 Hz and ion accumulation time of 5 milliseconds in the cell. Instrument external calibration was performed in negative ion mode using a standard calibration mixture of red phosphorous (Sigma-Aldrich). Instrument internal calibration was performed with reference masses of metabolites; adenosine monophosphate (AMP) at *m/z* 346.0558, adenosine diphosphate (ADP) at *m/z* 426.0221 and adenosine triphosphate (ATP) at *m/z* 505.9884, using FTMS Processing V2.1 (Bruker

Daltonik GmbH) and Compass Isotope Pattern V3.0 (Bruker Daltonik GmbH) to reach a mass error below 1 ppm.

Lipids were detected with norharmane matrix over the mass range *m/z* 400-1400 Da using a Bruker RapifleX MALDI Tissue-typer instrument operating in reflectron mode.
MS/MS experiments were performed using a SYNAPT G2Si instrument (Waters Corporation, Manchester, U.K.) to confirm the identification of selected compounds.

MALDI-MSI

The HTX TM-Sprayer (HTX Imaging, Chapel Hill) was used to spray 9AA matrix for sample preparation. A SYNAPT G2Si instrument was used to compare the different protocols and acquire the imaging data over the mass range *m/z* 100-1000 in negative ion mode using the sensitivity mode and a scan time of 1 second per pixel. The Nd:YAG MALDI laser was operated at a firing rate of 1000 Hz with a lateral resolution of 100 µm. A SolariX FT-ICR-MS instrument was used to validate the experimental model in imaging mode. FT-ICR MSI data was acquired with a lateral resolution of 40 µm. Ion accumulation time in the cell was set up at 5 milliseconds and 400 laser shots at a laser repetition frequency of 2000 Hz were used.

Data analysis

Compass DataAnalysis software V4.4 and FTMS Processing V2.1 were used to visualize the mass spectra and to calculate the signal to noise for each metabolite of interest in profiling mode.

For the experimental design approach, acquired data were processed and analyzed using HDI Imaging software V1.4 (Waters Corporation) by extracting the 1000 most abundant ions with the following settings: *m/z* window = 0.02 Da and MS resolution = 15000. Intensities were normalized by Total Ion Count (TIC) and Regions of Interest (ROIs) were manually created. Finally, intensities of ATP, ADP and UDP from these ROIs were used for elaborating the experimental design response variables as input into Aexd.net (Alleviating Science).[145]

Aexd.net was used to generate an experimental design in a six steps approach: *i*) creation of the first experimental design table, *ii*) acquisition of the data through the first set of experiments and data input into the dedicated software,

iii) statistical analysis of the results with generation of a model and definition of significant parameters of the HTX TM-Sprayer, *iv*) creation of the second experimental design table, *v*) acquisition of the data through the second set of experiments and data input into the software, *vi*) statistical analysis and visualization of the final results. The experimental design used a Plackett-Burman (PB-12+3) design followed by a surface response analysis of a central composite rotatable design (CCRD 2^2+2x2+3). Importantly, the step *vi* allowed for the creation of regression models for each response variable to describe the influence of variation in the dependent variables on the response variables. The parameters of the HTX TM-Sprayer used in the experimental design were the following: temperature, flow rate, drying time, number of layers, matrix concentration and percentage of solvent used to dissolve the matrix.

SCiLS lab 2019b software was used to calculate the metabolite intensities inside and outside the tissues (SCiLS lab, GmbH, Bremen, Germany) after root mean square (RMS) normalization for the imaging experiments acquired by FT-ICR-MS. The SQLite files generated were converted at a bin size of *m/z* 0.001 to MATLAB 2016b (The MathWorks, MA, USA) and in-house developed PEAPI software[146] was then used for peak-picking.
Finally, principal component analysis (PCA) followed by cluster analysis were applied to study the spatial metabolic distribution using an in-house ChemomeTricks toolbox for MATLAB. The Human Metabolome Database (HMDB) V4.0 and Metlin software V3.7.1 were used for molecular assignments with a tolerance up to 1 ppm. Drugs and exogenous compounds were automatically excluded for the assignments.

Histological staining

Safranin O staining procedure was used to discern the superficial area from the deep area of the cartilage. For this, matrix was removed by immersion in 70% ethanol and the sections were then stained using hematoxylin (Sigma-Aldrich) for 8 min, Safranin O (Sigma-Aldrich) 0.1% dissolved in ultrapure H_2O for 2 min and Fast Green FCF (Sigma-Aldrich) 0.1% dissolved in ultrapure H_2O for 4 min. Finally, digital images were acquired with the Mirax desk slide scanner V2.6 software (Carl Zeiss, Gottingen, Germany) after dehydrating steps.

3.4. Results and discussion

Heat stabilization slows-down the degradation of endogenous metabolites on cartilage

We evaluated the capability of heat stabilization to preserve the integrity of different endogenous metabolites when using 9AA matrix. Results showed for the first time the detection of nucleotides and nucleotide sugars from human cartilage tissue using 9AA (Figure 3.1). UTP was only detected when the samples were heat-stabilized before being snap frozen. When the samples were heat-stabilized, the observed metabolic patterns changed dramatically with a gain of sensitivity except for GDP and GMP. However, the triphosphate form (GTP) was detected 1.5-fold enhanced after heat stabilization. Interestingly, these experiments showed that triphosphate analytes (UTP, GTP and mostly ATP) were well-preserved after heat stabilization.

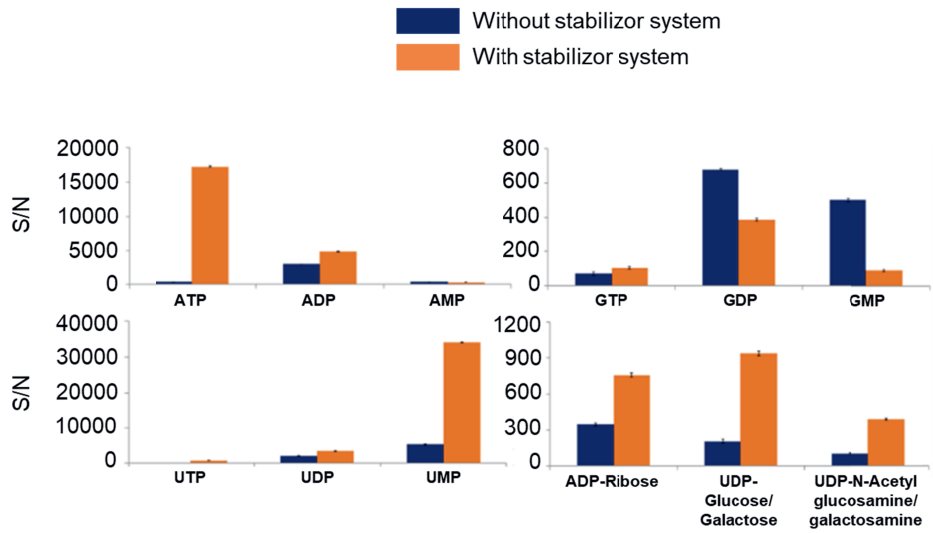

Figure 3.1. Metabolite detection on cartilage and their slowed-down degradation using the stabilizor system.

A previous study showed and confirmed that the inactivation of the proteolytic activity preserves the metabolic state better, which is in line with our data.[147] This improved preservation allowed us to perform MS/MS fragmentation to identify the detected compounds (Table 3.1). ATP, ADP, AMP, UDP and ADP-Ribose were assigned due to the presence of two or more specific fragments.[148]

Table 3.1. List of detected metabolites. Five metabolites (in bold) were assigned with high confidence by their accurate mass (MS1) and their MS/MS information. Eleven (*) were assigned based on their

accurate mass (MS1). HMDB and METLIN software were used for molecular assignments with a tolerance up to 1 ppm. Drugs and exogenous compounds were excluded during the search.

Assignment	Designation	Theoretical *m/z* value	Experimental *m/z* value	PPM error	Chemical Formula	MS/MS fragments
CMP*	$[M-H]^-$	322.0446	322.0448	0.70	$C_9H_{14}N_3O_8P$	-
UMP*	$[M-H]^-$	323.0286	323.0288	0.65	$C_9H_{13}N_2O_9P$	-
AMP*	$[M-H_2O-H]^-$	328.0452	328.0458	1.70	$C_{10}H_{14}N_5O_7P$	-
AMP	$[M-H]^-$	346.0558	346.0558	0.02	$C_{10}H_{14}N_5O_7P$	78.95 96.96 134.05 210.99
GMP*	$[M-H]^-$	362.0507	362.0507	0.06	$C_{10}H_{14}N_5O_8P$	-
UDP*	$[M-H_2O-H]^-$	384.9844	384.9848	1.15	$C_9H_{14}N_2O_{12}P_2$	-
UDP	$[M-H]^-$	402.9949	402.9948	0.30	$C_9H_{14}N_2O_{12}P_2$	78.95 158.91
ADP*	$[M-H_2O-H]^-$	408.0116	408.0118	0.55	$C_{10}H_{15}N_5O_{10}P_2$	-
UDP*	$[M+Na-2H]^-$	424.9769	424.9778	2.20	$C_9H_{14}N_2O_{12}P_2$	-
ADP	$[M-H]^-$	426.0221	426.0228	1.50	$C_{10}H_{15}N_5O_{10}P_2$	78.95 96.96 134.04 158.92 290.96 328.05
GDP*	$[M-H]^-$	442.0171	442.0170	0.12	$C_{10}H_{15}N_5O_{11}P_2$	-
ADP*	$[M+Na-2H]^-$	448.0041	448.0048	1.60	$C_{10}H_{15}N_5O_{10}P_2$	-
UTP*	$[M-H]^-$	482.9612	482.9620	1.66	$C_9H_{15}N_2O_{15}P_3$	-
ATP	$[M-H]^-$	505.9885	505.9888	0.65	$C_{10}H_{16}N_5O_{13}P_3$	78.95 96.96 134.04 158.92
GTP*	$[M-H]^-$	521.9834	521.9840	1.15	$C_{10}H_{16}N_5O_{14}P_3$	-
ATP*	$[M+Na-2H]^-$	527.9704	527.9708	0.73	$C_{10}H_{16}N_5O_{13}P_3$	-
ADP-Ribose	$[M-H_2O-H]^-$	540.0538	540.0538	0.06	$C_{15}H_{23}N_5O_{14}P_2$	158.91 408.01
Sodium ATP*	$[M+Na-2H]^-$	549.9524	549.9528	0.80	$C_{10}H_{15}N_5NaO_{13}P_3$	-
UDP-Glucose/Galactose*	$[M-H]^-$	565.0477	565.0484	1.20	$C_{15}H_{24}N_2O_{17}P_2$	-
UDP-N-Acetyl Glucosamine/Galactosamine*	$[M-H]^-$	606.0743	606.0754	1.80	$C_{17}H_{27}N_3O_{17}P_2$	-

Complementary data showed the possibility to detect enhanced intensities of lipid species. As an example, the *m/z* at 885.5 was 3-fold enhanced when using norharmane on heat stabilized cartilage samples (Figure 3.2). 885.5 *m/z* was identified as phosphatidylinositol [PI 18:0_20:4-H]$^-$, a well-known lipid detectable from a large variety of tissues in MSI experiments.[149-151] These data indicate that the use of the stabilizor system boosts the detection of other biomolecular classes.

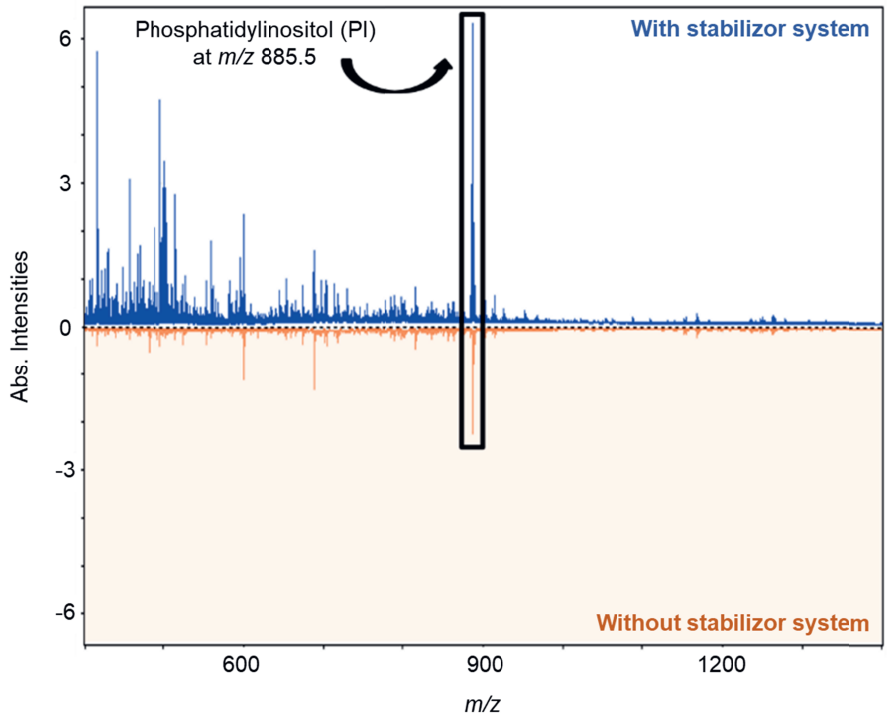

Figure 3.2. Profiling experiment with norharmane matrix in negative ion mode showed an enhanced lipid spectrum when using the stabilizor system.

Experimental design for metabolite detection on cartilage

Although profiling experiments showed interesting results using the stabilizor system such as higher intensities and better preservation of metabolic compounds, direct on-tissue detection of these species using MSI still remains challenging. This is mainly due to the low abundance of metabolites in contrast to other analytes such as lipids and the well-known ion suppression effect.[152] In addition, metabolite extraction for profiling experiments was performed using a very wet method, prone to compound delocalization, which is not suitable for imaging as the spatial distribution of the metabolites needs to be preserved. Therefore, method optimization for the detection of metabolites by MALDI-MSI is needed, especially considering the number of parameters to test in an imaging experiment. We applied this design of experiment strategy by optimizing the HTX TM-Sprayer settings (temperature, flow rate, drying time, number of layers, matrix concentration and percentage of solvent used to dissolve the matrix) as independent variables utilizing Aexd.net (Table 3.2) to improve the detection of metabolites on cartilage by MALDI-MSI.

Table 3.2. List of TM-SPRAYER™ settings. According to the experiments performed in step 1, the matrix concentration, the temperature, the number of layers and the flow rate were defined as non-significant parameters. Only the percentage of solvent used to dissolve the matrix was defined as a significant setting. Drying time was added to step 2 to confirm the non-significance of this setting.

		STEP 1			STEP 2		
TM-SPRAYER™ Settings	Unit	Lower value	Center value	High value	Lower value	Center value	High value
Matrix Concentration	mg/mL	7	8.5	10	fixed value: 10		
Solvent	%	60	65	70	50	75	100
Temperature	°C	65	72.5	80	fixed value: 80		
Number of layers	N	4	5	6	fixed value: 10		
Flow rate	mL/min	0.12	0.135	0.15	fixed value: 0.1		
Drying time	Sec	22	26	30	2	31	60

We evaluated the effects of these six independent variables on the overall imaging data quality which included i) the metabolite intensities within the tissue as well as ii) the delocalization outside the cartilage. A total of two response variables (i and ii) were then defined based on averages of ATP, ADP and UDP intensities on cartilage due to their overall good detectability in the profiling experiments. ROIs corresponding to tissue areas were created to calculate metabolite intensities within the tissues (i). Based on the imaging data, ROIs were also created at 5mm of distance from the edge of the sample to evaluate the analyte diffusion (ii) with an average number of 1200 pixels per region. The ratio between the average intensity of ATP, ADP and UDP inside (i)/outside the tissue defined the de-localization (ii). Final calculated values for each experiment were entered in the software to statistically define the most significant independent variables. Defining multiple response variables did not increase the number of experiments to be executed, but augmented the probability of achieving a valid prediction model: if a regression model can be established for at least one of these response variables, optimal settings of the independent variables can be predicted from that model. The final approach is described in figure 3.3.

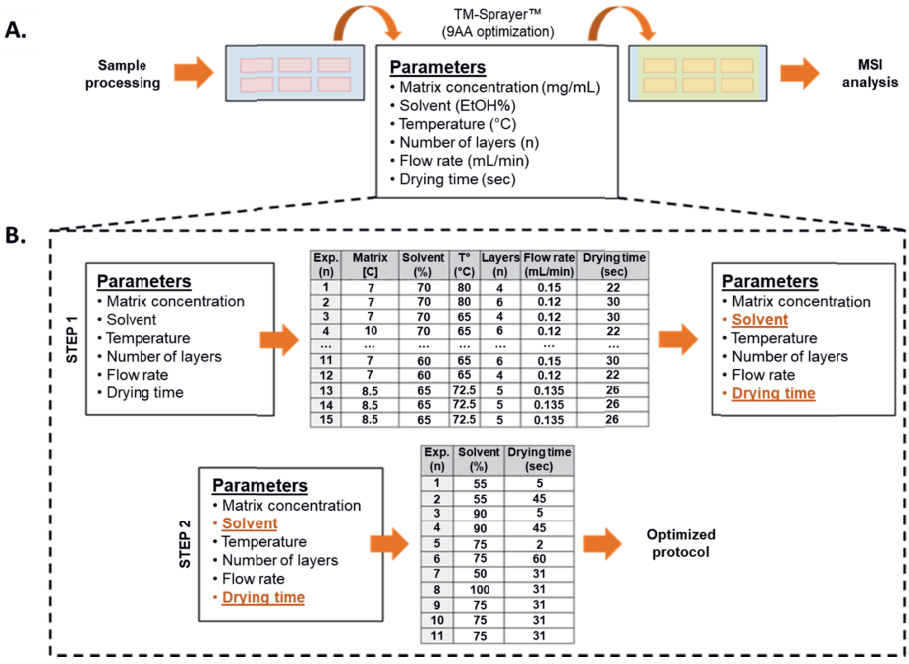

Figure 3.3. MSI workflow optimization for metabolite detection on cartilage using an experimental design approach. (**A**) Standard MSI workflow. (**B**) Schematic of the experimental design approach.

Briefly, a first step of 15 experiments performed in duplicate was designed to determine the significant settings of the HTX TM-Sprayer, meaning the settings influencing the most on (i) the metabolite intensities within the tissue and on (ii) the spatial distribution of these metabolites. In this way response variables were based on either metabolite intensity or spatial distribution. A second set of experiments was subsequently conducted to optimize these significant settings and increase the sensitivity for metabolite detection while preserving their spatial information as much as possible. Results from the first set of experiments showed that EtOH percentage was the most significant parameter influencing the quality of the data, meaning high intensity and good spatial preservation (Figure 3.4A, B). The t-values (t(8) and t(5)) represent the effect divided by the standard error. The effects are estimated alterations of the response-variable caused by changes of independent variables (concentration of matrix, percentage of solvent, temperature, layers, flow rate and drying time). Squared factors as (drying time)2 and (Solvent %)2 are factors responsible for the curvature of the model. We decided to add the drying time to the second step as an independent variable to verify if the statistical non-significance of this feature could be confirmed or negated for a wider value

range. This second step was conducted on 11 experiments. Three different solvent percentages (50, 75 and 100) as well as three different drying times (2, 31 and 60 seconds) were used as lower, center, and high values, respectively. As the other parameters were not significant, fixed values were chosen based on the first step (Table 3.2). The same response variables were used as described in the first step. Results showed that EtOH percentage for the solvent used for the matrix is still a significant parameter, confirming results of the first step of 15 experiments (Figure 3.4C, D). The drying time still appeared to be statistically non-significant (Figure 3.4C, D).

A.

	Effects	Standard Error	t(8)	p-value
Mean	2.55	0.30	8.57	<0.0001
Matrix C	-0.37	0.75	-0.50	0.63
Solvent %	-1.62	0.75	-2.17	0.06
Temperature	1.03	0.75	1.38	0.20
Layers	-0.62	0.75	-0.83	0.43
Flow rate	0.60	0.75	0.81	0.44
Drying time	-0.72	0.75	-0.97	0.36

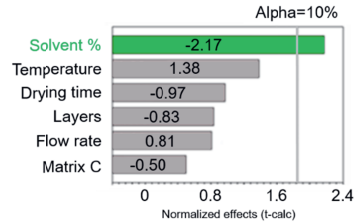

B.

	Effects	Standard Error	t(8)	p-value
Mean	2.12	0.25	8.43	<0.0001
Matrix C	-0.68	0.63	-1.07	0.31
Solvent %	-2.05	0.63	-3.26	0.01
Temperature	0.05	0.63	0.07	0.94
Layers	0.66	0.63	1.05	0.33
Flow rate	0.83	0.63	1.32	0.22
Drying time	-0.09	0.63	-0.15	0.88

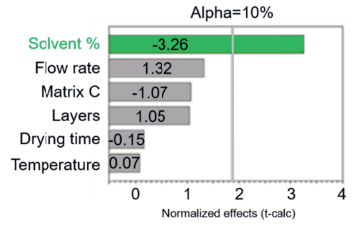

C.

	Effects	Standard Error	t(5)	p-value
Mean	0.08	0.05	1.62	0.17
Drying time	-0.11	0.07	-1.63	0.16
Solvent %	-0.45	0.06	-6.98	0.00
(Drying time)²	-0.02	0.07	-0.23	0.83
(Solvent %)²	0.48	0.07	6.56	0.00
Drying time * Solvent %	0.01	0.09	0.13	0.90

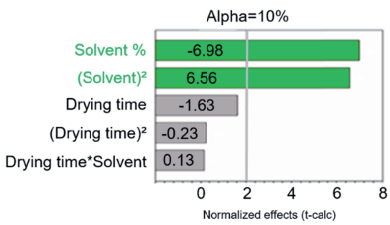

D.

	Effects	Standard Error	t(5)	p-value
Mean	3.95	2.57	1.54	0.18
Drying time	-4.00	3.44	-1.16	0.30
Solvent %	-10.45	3.38	-3.09	0.03
(Drying time)²	-0.58	3.60	-0.16	0.88
(Solvent %)²	4.87	3.84	1.27	0.26
Drying time * Solvent %	3.06	4.49	0.68	0.53

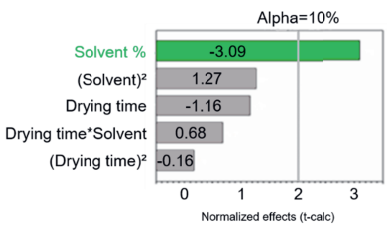

Figure 3.4. Effects of the HTX TM-Sprayer settings on the metabolite intensities inside the tissue (A) and their delocalization outside the tissue (B) in the first step of the experimental design. The same statistics were applied to the second step of the experimental design (**C**, **D**).

Validation of the experimental design on cartilage metabolic distribution

In order to validate our approach, three experiments on consecutive sections were carried out in duplicate using FT-ICR instrument with different solvent percentages and drying times within the range of the experimental design (Figure 3.5).

A.

TM-SPRAYER™ Settings	Unit	Experiments (in duplicate)		
		1	2	3
Drying time	sec	5	45	30
Solvent	%	55	55	50
Temperature	°C	80		
Number of layers	N	10		
Flow rate	mL/min	0.1		
Matrix concentration	mg/mL	10		

B.

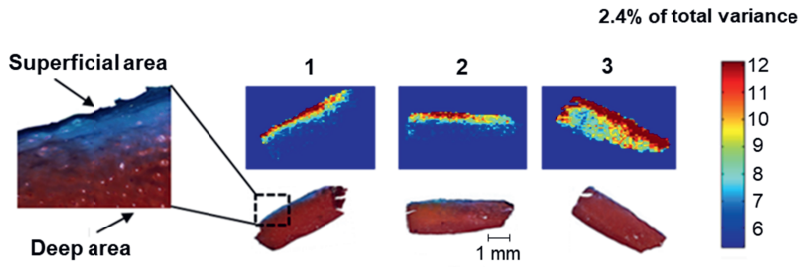

C.

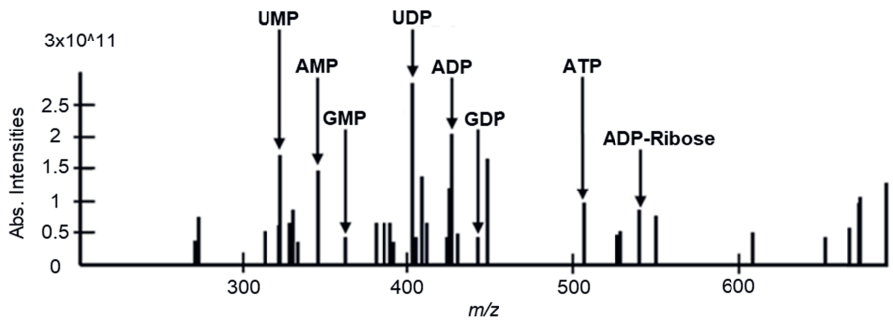

Figure 3.5. Model validation based on MALDI-FT-ICR data. (**A**) HTX settings used to validate the experimental design model. (**B**) Cluster images with the subsequent stained tissue. (**C**) Reconstructed cluster spectrum.

The other settings from the HTX TM-Sprayer were set-up as depicted in the step 2 of the table 3.2. All three experiments showed more intensity inside than outside the tissue according to the calculated ratios (Figure 3.6).

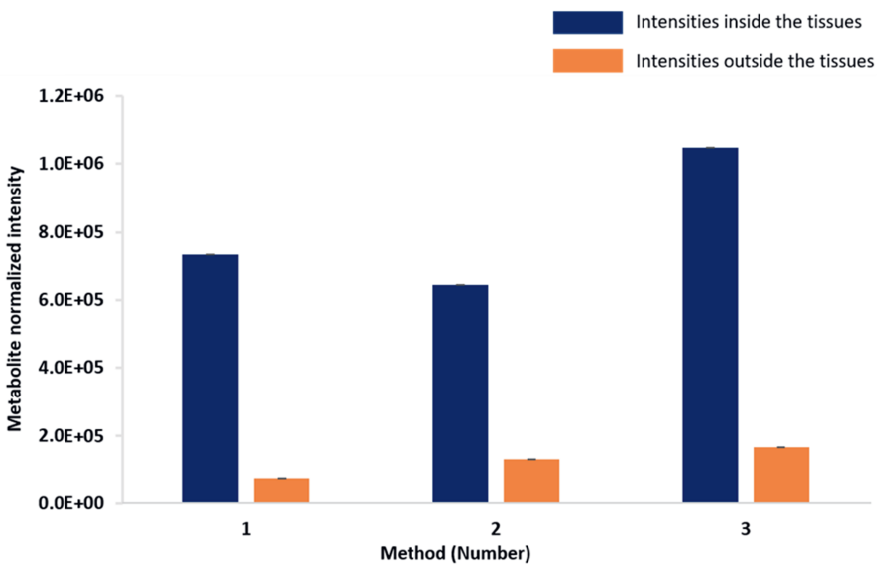

Figure 3.6. Validation of the experimental design model. Intensities of ATP, ADP and UDP were normalized by root mean square (RMS) for each experiment performed in duplicate.

From these, experiments 1 and 2 showed similar results in terms of metabolite intensity confirming that drying time had no significant effect (Figure 3.6). Experiments using 50% EtOH showed a better metabolite extraction than using 55% EtOH. These results confirmed the significance of the solvent percentage in the detection of metabolite species. In addition to this validation, PCA and clustering analysis showed here for the first time the specific metabolic distribution of a cluster of species (ATP, ADP, AMP, UDP, UMP, GDP, GMP and ADP-ribose) in human cartilage (Figure 3.5B, C).

In particular the experiments 1 and 2 demonstrated that this panel of metabolites are distributed in the superficial area of the human OA cartilage when compared to the histological safranin O staining (Figure 3.5B). This result showed the importance of the safranin O staining for accurate co-registration with the MSI data. This specific distribution is in particular relevant since the superficial area of the cartilage is in close contact with the synovial fluid and it's the only zone where articular cartilage progenitor cells have been found.[153] 50% EtOH seemed to improve the extraction of metabolites but compromising the intra-tissue spatial heterogeneity and therefore resulting in intra-tissue metabolic de-localization (Figure 3.5B). Here,

the data showed that ethanol percentage and drying time might be critical to keep the spatial intra-tissue metabolic distribution, meaning to differentiate superficial and deep areas of the cartilage. Another experimental design model should be considered to statistically validate this hypothesis. Based on our results, methods 1 and 2 are equally optimal to study the metabolic spatial distribution in cartilage.

3.5. Chapter conclusions

To the best of our knowledge, this is the first study that reports the detection of endogenous metabolites in cartilage using MALDI-MSI. We showed the efficiency of heat stabilization to preserve endogenous metabolites within the cartilage and demonstrated for the first time the potential of experimental design to optimize MALDI-MSI sample preparation protocols. Especially, the optimized results revealed a higher presence of metabolites in the superficial area of the cartilage. This method could be employed to further study metabolic spatial abnormalities in human OA cartilage.

Acknowledgements
The work was performed as part of the M4I research program that was financially supported by the Dutch Province of Limburg through the "LINK" program and by the MUMC+ institutional grant for clinical collaborative research.

CHAPTER 4

Heterogeneity in lipid and protein cartilage profiles associated with human osteoarthritis with or without type 2 diabetes mellitus

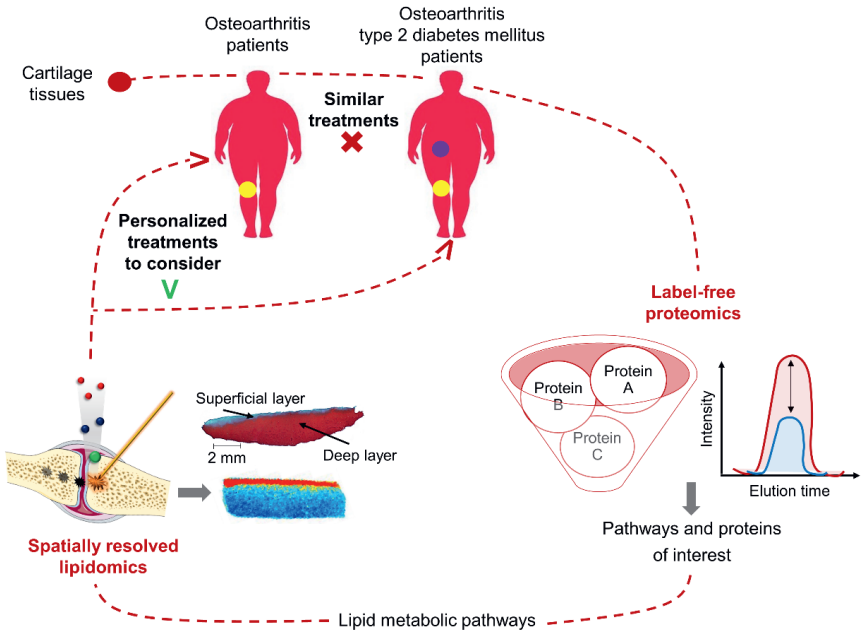

Adapted from:

Heterogeneity in lipid and protein cartilage profiles associated with human osteoarthritis with or without type 2 diabetes mellitus

Eveque-Mourroux MR, Emans PJ, Boonen A, Claes BSR, Bouwman FG, Heeren RMA, Cillero-Pastor B

Submitted to Journal of Proteome Research – In revision (**2020**)

4. Heterogeneity in lipid and protein cartilage profiles associated with human osteoarthritis with or without type 2 diabetes mellitus

4.1. Abstract

Osteoarthritis (OA) is a multifactorial pathology and comprises a wide range of distinct phenotypes. In this context, the characterization of the different molecular profiles associated with each phenotype can improve the classification of OA for better therapies. In particular, OA can co-exist with type 2 diabetes mellitus (T2DM). This study investigates lipidomic and proteomic differences between human OA/T2DM$^-$ and OA/T2DM$^+$ cartilage through a multimodal mass spectrometry approach.

Human cartilage samples were obtained after total knee replacement from OA/T2DM$^-$ (n=10) and OA/T2DM$^+$ patients (n=10). Label-free proteomics was employed to study differences in protein abundance and matrix-assisted laser desorption/ionization (MALDI) mass spectrometry imaging (MSI) for spatially resolved-lipid analysis.

Label-free proteomic analysis showed differences between OA/T2DM$^-$ and OA/T2DM$^+$ phenotypes in several metabolic pathways such as lipid regulation. Interestingly, the phospholipase A2 protein (PLA2G2A), was found overexpressed within the OA/T2DM$^+$ cohort. In addition, MALDI-MSI experiments revealed that phosphatidylcholine (PC) and sphingomyelin (SM) species were characteristic of the OA/T2DM$^-$ whereas lysolipids were more characteristic of the OA/T2DM$^+$ phenotype. The data also pointed out differences in phospholipid content between superficial and deep layers of the cartilage.

Our study shows distinctively different lipid and protein profiles between OA/T2DM$^-$ and OA/T2DM$^+$ human cartilage, demonstrating the importance of sub-classification of the OA disease for better personalized treatments.

4.2. Introduction

Osteoarthritis (OA) is mainly characterized by the progressive deterioration of articular cartilage and it is the most common form of arthritis worldwide, affecting over 10% of the population above 60 years.[4, 118, 154] OA is recognized as an age-related joint disease[3, 155] but an increasing number of risk factors have been associated with the development of the pathology.[5] Therefore, OA is considered as a multifactorial pathology which suggests a wide range of distinct phenotypes rather than a single

disease.[156] However, all the patients receive similar treatments regardless of these phenotypes.[157]

Models for patient classification have been proposed to try to establish different OA phenotypes.[7, 158] The classification of OA patients into different groups can significantly transform OA clinical trials and enhance their efficiency towards a personalized medicine approach. From the phenotypes proposed in the literature, the metabolic syndrome phenotype is defined by chronic low-grade inflammation, which leads to systemic and local molecular changes.[8] The metabolic syndrome is defined as a health disorder that increases the risk of type 2 diabetes mellitus (T2DM), hypertension, or dyslipidemia.[13] Interestingly, different studies have shown a correlation between T2DM and OA[15, 16] and a higher prevalence of OA in T2DM patients.[17, 159] To better understand this predisposition, the basic molecular (i.e. proteins and lipids) mechanisms underlying the pathological processes of both diseases need to be considered.

In this work, we hypothesized that OA/T2DM$^-$ and OA/T2DM$^+$ human knee cartilage present differential molecular profiles. For this purpose, label-free proteomics and spatially resolved lipidomics using a matrix-assisted laser desorption/ionization (MALDI) mass spectrometry imaging (MSI), have been employed.

4.3. Materials and methods

Sample collection

The Maastricht University Medical Centre's institutional policy on the use of residual human surgical material states that no informed consent is needed in the case of residual surgical material (METC number of the WMO approval waste material TKA: 2017-0183). Human cartilage from OA/T2DM$^-$ (n=10) and OA/T2DM$^+$ patients (n=10) was obtained from donors undergoing total knee joint replacement. Additional information such as age, gender, affected knee, body mass index (BMI), and Kellgren-lawrence (KL) scores can be found in table 4.1.

Table 4.1. Patient information. The (*) displayed the samples used for the comparative MALDI-MSI experiments. (BMI: Body mass index; KL: Kellgren-Lawrence).

	Sample number	Age	Gender	Affected knee	BMI	KL score
OA/T2DM⁻ patients (n=10)	1*	78	Male	Left	25.0	2
	2*	61	Male	Left	32.0	3
	3*	80	Female	Left	30.5	4
	4*	82	Male	Left	24.3	4
	5*	59	Female	Right	25.7	3
	6*	71	Male	Left	26.9	3
	7	67	Female	Left	24.0	3
	8	77	Female	Left	Not specified	Not specified
	9	75	Male	Left	28.0	4
	10	66	Female	Right	27.0	4
OA/T2DM⁺ patients (n=10)	1*	86	Male	Left	24.9	4
	2*	70	Female	Right	34.9	3
	3*	72	Male	Right	32.4	4
	4*	78	Male	Left	35.6	4
	5*	81	Male	Right	24.9	3
	6*	75	Male	Left	27.7	3
	7	75	Female	Left	33.3	2
	8	56	Female	Left	37.2	Not specified
	9	73	Male	Right	28.4	4
	10	58	Male	Right	23.9	4

Unwounded cartilage areas were selected macroscopically, cut into punches of 8 mm and heat stabilized (Denator, Uppsala, Sweden) to avoid molecular degradation before being snap-frozen in liquid nitrogen and stored at -80°C. [160-162] The punches were finally sectioned at 12 µm thickness with a cryostat (Leica Microsystems, Wetzlar, Germany) at -20°C (Figure 4.1).

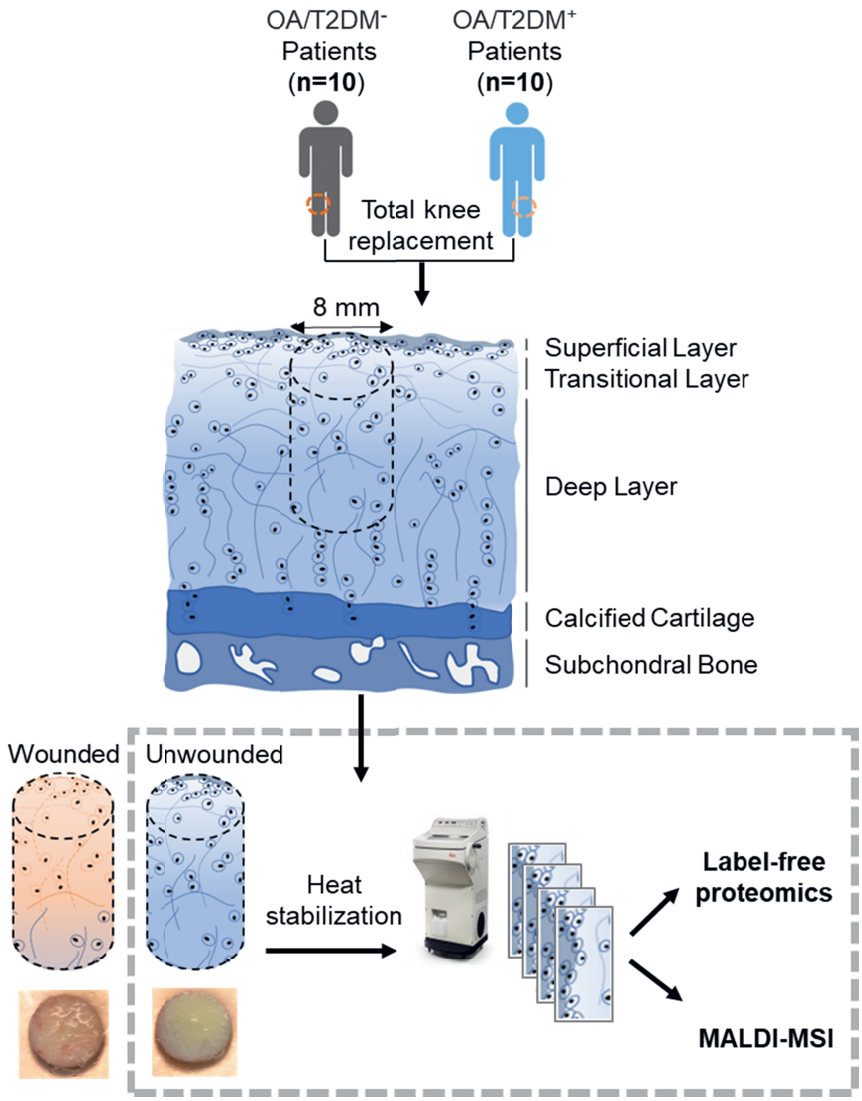

Figure 4.1. Sample collection and processing. Human cartilage was obtained from patients undergoing total knee replacement. The tissues were cut into punches of 8 mm. Unwounded cartilage punches were isolated from the wounded tissue macroscopically. The unwounded cartilage punches were heat stabilized to avoid molecular degradation before being snap-frozen in liquid nitrogen. Finally, 12 µm thick sections were prepared for either label-free proteomics or MALDI-MSI experiments.

Label-free proteomics – Protein extraction

For label-free proteomics experiments, 30 consecutive tissue sections per patient were collected in Eppendorf tubes. 100 µL of 50 mM ammonium bicarbonate (ABC) buffer

(Sigma-Aldrich, Zwijndrecht, the Netherlands) containing 5 M Urea (GE Healthcare, Eindhoven, the Netherlands) and 0.2% Rapigest (Waters Corporation, MA, USA) were added to the 20 samples. Proteins were then extracted by freeze-thaw cycles (3X), with 1 minute of sonication step between each cycle. After 30 minutes of centrifugation at 14.000 rpm at 4°C, the supernatant containing proteins was finally transferred into new tubes and stored at -80° until further analysis. Bradford assay (Biorad, Lunteren, The Netherlands) was performed to assess the protein concentration.

***Label-free proteomics* – Gel electrophoresis**

10 µg of proteins of each patient were loaded on a 12% sodium dodecyl sulfate polyacrylamide gel electrophoresis (SDS-PAGE) and run shortly for 4 minutes at 180 volts. The gel was stained with Coomassie blue (Sigma-Aldrich) for protein visualization. The protein bands were excised from the gel and processed on a MassPREP digestion robot (Waters, Manchester, UK). The destaining of the Coomassie was performed using 50 mM of ABC buffer mixed with 50% acetonitrile (Biosolve, Valkenswaard, the Netherlands). Then, cysteines were reduced with 10 mM dithiothreitol (Sigma-Aldrich) in 100 mM ABC for 30 minutes followed by alkylation with 55 mM iodoacetamide (Sigma-Aldrich) in 100 mM ABC for 20 minutes in the dark. Spots were washed with 100 mM ABC to remove excess reagents and dehydrated with 100% acetonitrile. Trypsin (Promega, Leiden, the Netherlands) at 6 ng/ul in 50 mM ABC was added to the gel plugs and incubated at 37°C for 5 hours. The peptides were finally extracted three times with 50 µl of 1% formic acid (Biosolve) and 2% acetonitrile. The volume of the peptide extract was reduced in a speedvac until a final volume of 50 µl was reached.

***Label-free proteomics* – Data acquisition and processing**

400 ng of protein were injected for liquid-chromatography mass spectrometry (LC-MSMS) analysis. The separation of the peptides was performed on a Thermo Fisher Scientific Dionex Ultimate 3000 Rapid Separation ultrahigh-performance liquid-chromatography (HPLC) system (Thermo Scientific, MA, USA) equipped with an Acclaim PepMap C18 analytical column (2µm, 75µm*500 mm, 100Å). The samples were first trapped on an online C18 column for desalting. The peptides were then separated on the analytical column with a 180-minutes linear gradient from 5% to 45% acetonitrile/0.1% formic acid and a flow rate set at 300 nL/min. The HPLC system was coupled on-line to a high-mass resolution orbitrap MS Q-Exactive instrument (Thermo Scientific) with a nano-electrospray Flex ion source (Proxeon, Thermo Scientific, MA, USA). The mass spectrometer was operated in positive ion polarity in data-dependent acquisition (DDA) mode with the following settings: Full

MS scan of the mass range *m/z* 250-1,250 at a resolution of 70,000 at *m/z* 200 with a maximum injection time of 120 ms, followed by tandem mass spectrometry (MS/MS) scans for the fragmentation of the 10 most intense ions at a resolution of 17,500. Isolation of precursors was performed with a 1.8 *m/z* window and a maximum injection time of 200 ms. The ions already selected for fragmentation were dynamically excluded for 30s. External calibration of the instrument was performed using a standard calibration solution for positive ion mode (Thermo Scientific).
For protein identification, raw files were processed within the Proteome Discoverer software version 2.2 (Thermo Scientific) using the search engine Sequest with the Swiss-Prot human database *Homo sapiens* version 2020-02-10 (TaxID 9606). The following parameters were used for the database search: Carbamidomethylation of C for fixed modifications; oxidation of M and acetylation of protein *N*-term for variable modifications; trypsin for enzyme with a maximum of two missed cleavages; the precursor mass tolerance was set at 10 ppm and the fragment tolerance at 0.02 Da; minimum and maximum peptide length of 6 and 144 amino acids, respectively. Normalization of the data was performed on the total peptide amount. Percolator was used for the decoy database search and the FDR was fixed at 1% maximum. For protein quantitation, the Minora Feature Detector node in the processing step and the Feature Mapper node combined with the Precursor Ions Quantifier node in the consensus step were used with default settings.

***Label-free proteomics* – Data analysis**

ANOVA test was performed within the Proteome Discoverer software to analyze the statistical significance of variation observed in protein abundance between the OA/T2DM$^-$ and OA/T2DM$^+$ patients. The proteins were considered modulated with an adjusted p-value≤0.05 and a fold change (FC) cut-off set at 1.5-fold. The modulated proteins were then imported within the EnrichR software [163] to display the top 10 pathways of down or up-regulated proteins ranked by the combined score. WikiPathways and KEGG were used as databases (version 2019, Human).

***MALDI-MSI* – Matrix application**

12 µm tissue sections were thaw mounted over cleaned indium tin oxide (ITO) glass slides (Delta Technologies, CO, USA) coated with double-sided conductive copper tape 1182 (3M Science, MN, USA). Norharmane (Sigma-Aldrich) was used as a matrix for lipid analysis. Eight layers of the matrix at 7 mg/mL in chloroform/methanol (2:1, (v/v)) were sprayed at 30°C with a flow rate of 0.12 mL/min using the HTX TM-Sprayer system (HTX Imaging, NC, USA). A drying time of 30s between each layer and a velocity set at 1200 mm/min were used to enable homogeneous matrix application.

***MALDI-MSI* – Data acquisition and processing**

MALDI-MSI experiments were performed in positive ion polarity at 50 µm of lateral resolution using a RapifleX MALDI Tissue-typer instrument operating in reflectron mode (Bruker, Bremen, Germany) to compare the lipidomic profiles of OA/T2DM$^-$ and OA/T2DM$^+$ patients. Lipids were detected over the mass range *m/z* 300-1600.

A Waters Synapt G2Si coupled to a µMALDI source (Waters) with a lateral resolution of 15 µm in combination with the Waters Research Enabled Software (WREnS) was employed for high spatial resolution MALDI-MSI experiments. [164] The following settings were used for the data acquisition: mass range *m/z* 400-1200, automatic quadrupole mode profile and laser pulse energy of 300 (a.u). External calibration on both instruments was performed using the standard calibration mixture of red phosphorous (Sigma-Aldrich) with a mass error below 10 ppm.

For the DDA-imaging experiments, a MALDI-MSI method that enables data-dependent acquisition (DDA) of tandem mass spectrometry data in parallel with a high-mass resolution mass spectrometry imaging experiment was employed. [165] The experiments were carried out on OA/T2DM$^-$ and OA/T2DM$^+$ tissue sections with a stage step size of 25 µm (horizontal) × 50 µm (vertical) and performed in positive ion polarity using the orbitrap Elite hybrid ion trap mass spectrometer over the mass range *m/z* 200-2000. A resolution of 240,000 at *m/z* 400 with a maximum injection time of 250 ms for the orbitrap was used. The MSMS were performed in the ion trap using the following settings: isolation of precursors set at 0.7 *m/z* window and activation q: 0.17. The CID was used using a normalized collision energy (NCE) set up at 30 eV. External calibration of the instrument was performed as described in the label-free proteomics section.

***MALDI-MSI* – Data analysis**

For the MALDI-MSI comparative approach, raw data were processed by SCiLS lab software version 2019b (SCiLS, Bremen, Germany). Principal component analysis (PCA) and linear discriminant analysis (LDA) were performed after peak picking using an in-house-built ChemomeTricks toolbox for MATLAB version 2012B (The MathWorks, MA, USA). [146]

For the µMALDI experiment, data were processed using the High Definition Imaging software version 1.4 (Waters) by extracting the 1000 most abundant ions with the following settings: *m/z* window set at 0.02 Da and MS resolution at 15000. Processed data were then exported to imzML format before being imported into SCiLS lab

MultiVendor Support (MVS) software version 2019b. Within the software, the standard segmentation pipeline using bisecting k-means algorithm and a pLSA analysis with random initialization were performed on the data normalized by total ion current (TIC) with weak denoising and with an *m/z* interval width set to ± 0.1 Da.

For the DDA-imaging approach, lipid assignments were performed within lipostarMSI software version 1.0 and manually checked using Xcalibur software version 4.2. [166] Within the lipostarMSI software, the following settings were used: the precursor and the fragments mass tolerances were set at 3 ppm and 0.25 ppm, respectively, and the lipid assignments were based in at least 10 or more MS/MS scans.

***MALDI* – Lipid identification**

Lipids of interest were identified using targeted MS/MS analysis performed in the ion trap of the orbitrap Elite hybrid ion trap mass spectrometer (Thermo Scientific). The collision induced dissociation (CID) was used to fragment the precursors within an isolation window of 1 Da and with a normalized collision energy (NCE) set up at 30 eV. Each precursor from the inclusion list was measured for 1 minute in a continuous acquisition mode. For low abundant species, lipid extraction was performed in chloroform/methanol (2:1, (v/v)) with 50 µmol of ammonium formate (Biosolve). The extract was then analysed using the high-mass resolution orbitrap MS Q-Exactive instrument using electrospray ionization (ESI). External calibration of the instrument was performed as described in the label-free proteomics section. Lipids were assigned manually using Xcalibur software version 4.2 and tentatively assigned using the online ALEX^{123} library. [167]

Histological staining

Matrix was removed by immersion in 70% ethanol. The sections were then stained using hematoxylin (Sigma-Aldrich) for 8 minutes, Safranin O (Sigma-Aldrich) 0.1% dissolved in ultrapure H_2O for 2 minutes and Fast Green FCF (Sigma-Aldrich) 0.1% dissolved in ultrapure H_2O for 4 minutes. Finally, digital images were acquired with the M8 scanner (Precipoint, Freising, Germany) after dehydrating steps.

4.4. Results and discussion

Lipid pathway differences between OA phenotypes

Label-free proteomics followed by enrichment analysis of the differentially expressed proteins, is a powerful tool to investigate specific pathways associated with OA subgroups. After data processing, a total of 1605 proteins were identified. Among them, 115 displayed statistically significant differences (adjusted p-value≤0.05; FC cut-off set at 1.5-fold) between the two conditions (Table 4.2).

Table 4.2. Significantly up and down-regulated proteins found in OA/T2DM$^-$ compared to OA/T2DM$^+$. The FC cut-off is at 1.5-fold and adjusted p-value is ≤ 0,05. 75 proteins were found overexpressed in OA/T2DM$^-$ samples whereas 40 were found overexpressed in OA/T2DM$^+$ patients.

Protein ID	Protein Name	Fold change	p-value
O75828	Carbonyl reductase [NADPH] 3	0.01	1.99E-16
P13796	Plastin-2	0.01	1.99E-16
P02778	C-X-C motif chemokine 10	0.01	1.99E-16
P43121	Cell surface glycoprotein MUC18	0.01	1.99E-16
P15144	Aminopeptidase N	0.01	1.99E-16
P02730	Band 3 anion transport protein	0.01	1.99E-16
P36269	Glutathione hydrolase 5 proenzyme	0.01	1.99E-16
Q99439	Calponin-2	0.01	1.99E-16
Q6UWY5	Olfactomedin-like protein 1	0.01	1.99E-16
P13591	Neural cell adhesion molecule 1	0.01	1.99E-16
P35222	Catenin beta-1	0.01	1.99E-16
P35542	Serum amyloid A-4 protein	0.01	1.99E-16
P13686	Tartrate-resistant acid phosphatase type 5	0.01	1.99E-16
P27918	Properdin	0.01	1.99E-16
Q08397	Lysyl oxidase homolog 1	0.01	1.99E-16
P55290	Cadherin-13	0.01	1.99E-16
Q08188	Protein-glutamine gamma-glutamyltransferase E	0.01	1.99E-16
Q9Y333	U6 snRNA-associated Sm-like protein LSm2	0.01	1.99E-16
Q9NZ08	Endoplasmic reticulum aminopeptidase 1	0.01	1.99E-16
Q13451	Peptidyl-prolyl cis-trans isomerase FKBP5	0.01	1.99E-16
P47985	Cytochrome b-c1 complex subunit Rieske, mitochondrial	0.01	1.99E-16
P49821	NADH dehydrogenase [ubiquinone] flavoprotein 1, mitochondrial	0.01	1.99E-16
P10451	Osteopontin	0.08	1.99E-16
Q9BRX8	Peroxiredoxin-like 2A	0.11	1.99E-16
O60938	Keratocan	0.24	2.71E-05
P10620	Microsomal glutathione S-transferase 1	0.24	3.72E-08
P00915	Carbonic anhydrase 1	0.24	7.42E-13
P68400	Casein kinase II subunit alpha	0.28	4.49E-06
Q16647	Prostacyclin synthase	0.29	1.13E-03
P27487	Dipeptidyl peptidase 4	0.30	2.93E-03
P02452	Collagen alpha-1(I) chain	0.30	4.33E-09
Q4ZHG4	Fibronectin type III domain-containing protein 1	0.31	1.79E-03
P02647	Apolipoprotein A-I	0.31	1.35E-08
P62834	Ras-related protein Rap-1A	0.31	1.41E-06
P61086	Ubiquitin-conjugating enzyme E2 K	0.32	6.00E-04
Q7Z304	MAM domain-containing protein 2	0.32	2.17E-03
P16219	Short-chain specific acyl-CoA dehydrogenase, mitochondrial	0.32	4.33E-03
P02652	Apolipoprotein A-II	0.34	4.50E-03
Q9BX68	Histidine triad nucleotide-binding protein 2, mitochondrial	0.35	2.21E-02
P08572	Collagen alpha-2(IV) chain	0.35	6.38E-03
Q9UI09	NADH dehydrogenase [ubiquinone] 1 alpha subcomplex subunit 12	0.36	3.06E-02

P56385	ATP synthase subunit e, mitochondrial	0.36	9.09E-03
P78539	Sushi repeat-containing protein SRPX	0.37	8.86E-03
P49327	Fatty acid synthase	0.40	4.01E-02
P23141	Liver carboxylesterase 1	0.41	4.77E-02
Q13103	Secreted phosphoprotein 24	0.42	1.74E-02
P36955	Pigment epithelium-derived factor	0.43	2.53E-04
P24592	Insulin-like growth factor-binding protein 6	0.44	4.16E-02
P02750	Leucine-rich alpha-2-glycoprotein	0.44	8.81E-03
P21589	5'-nucleotidase	0.44	5.68E-04
P55854	Small ubiquitin-related modifier 3	0.44	2.46E-03
P09486	SPARC	0.45	1.13E-04
P04179	Superoxide dismutase [Mn], mitochondrial	0.47	2.32E-03
Q96CX2	BTB/POZ domain-containing protein KCTD12	0.47	3.10E-02
P08123	Collagen alpha-2(I) chain	0.48	3.19E-03
Q07507	Dermatopontin	0.49	5.12E-03
P05452	Tetranectin	0.49	5.41E-03
Q6UXI7	Vitrin	0.49	5.51E-03
P21980	Protein-glutamine gamma-glutamyltransferase 2	0.49	5.72E-03
P62750	60S ribosomal protein L23a	0.49	3.39E-02
P62424	60S ribosomal protein L7a	0.50	7.94E-03
P36542	ATP synthase subunit gamma, mitochondrial	0.50	1.53E-02
Q96CG8	Collagen triple helix repeat-containing protein 1	0.50	9.20E-03
P08294	Extracellular superoxide dismutase [Cu-Zn]	0.51	1.08E-02
Q9UBI6	Guanine nucleotide-binding protein G(I)/G(S)/G(O) subunit gamma-12	0.51	1.73E-02
Q8IUE6	Histone H2A type 2-B	0.51	3.67E-02
Q5T749	Keratinocyte proline-rich protein	0.52	5.82E-03
P40429	60S ribosomal protein L13a	0.53	3.33E-02
Q53TN4	Cytochrome b reductase 1	0.54	3.47E-02
P52566	Rho GDP-dissociation inhibitor 2	0.54	3.99E-02
Q99715	Collagen alpha-1(XII) chain	0.54	3.39E-02
Q9BXN1	Asporin	0.54	3.75E-02
O60814	Histone H2B type 1-K	0.54	4.01E-02
P02790	Hemopexin	0.55	2.46E-02
P29279	CCN family member 2	0.57	4.41E-02
O75339	Cartilage intermediate layer protein 1	1.51	8.64E-03
P83110	Serine protease HTRA3	1.52	6.97E-03
P34096	Ribonuclease 4	1.55	4.77E-03
P03950	Angiogenin	1.57	4.09E-03
P06727	Apolipoprotein A-IV	1.59	2.83E-03
Q9NRA1	Platelet-derived growth factor C	1.63	2.50E-03
Q92743	Serine protease HTRA1	1.63	1.64E-03
P61626	Lysozyme C	1.71	5.68E-04
P35625	Metalloproteinase inhibitor 3	1.73	4.28E-04
Q02818	Nucleobindin-1	1.78	2.17E-02
P02489	Alpha-crystallin A chain	1.79	1.80E-04
O15232	Matrilin-3	1.81	1.34E-04
Q9UHY7	Enolase-phosphatase E1	1.83	8.52E-03
P14555	Phospholipase A2, membrane associated	1.90	3.30E-05
Q687X5	Metalloreductase STEAP4	1.94	5.97E-06
P63220	40S ribosomal protein S21	1.94	2.20E-05
P00352	Retinal dehydrogenase 1	2.42	9.10E-07
P02766	Transthyretin	2.95	4.90E-12
A8K7I4	Calcium-activated chloride channel regulator 1	3.00	6.17E-09
Q7L211	Protein ABHD13	3.85	1.99E-16
P07316	Gamma-crystallin B	4.96	1.99E-16

P07315	Gamma-crystallin C	5.05	1.99E-16
P11844	Gamma-crystallin A	5.43	1.99E-16
P05813	Beta-crystallin A3	6.35	1.99E-16
Q06141	Regenerating islet-derived protein 3-alpha	10.72	1.99E-16
P17661	Desmin	100.00	1.99E-16
Q03013	Glutathione S-transferase Mu 4	100.00	1.99E-16
Q01524	Defensin-6	100.00	1.99E-16
P07148	Fatty acid-binding protein, liver	100.00	1.99E-16
P17096	High mobility group protein HMG-I/HMG-Y	100.00	1.99E-16
P53672	Beta-crystallin A2	100.00	1.99E-16
P50440	Glycine amidinotransferase, mitochondrial	100.00	1.99E-16
Q14956	Transmembrane glycoprotein NMB	100.00	1.99E-16
Q14258	E3 ubiquitin/ISG15 ligase TRIM25	100.00	1.99E-16
Q14117	Dihydropyrimidinase	100.00	1.99E-16
P08246	Neutrophil elastase	100.00	1.99E-16
P53674	Beta-crystallin B1	100.00	1.99E-16
O00175	C-C motif chemokine 24	100.00	1.99E-16
P08473	Neprilysin	100.00	1.99E-16
Q8TF66	Leucine-rich repeat-containing protein 15	100.00	1.99E-16

Among those, 75 were more abundant in OA/T2DM$^-$ samples whereas 40 were more abundant in OA/T2DM$^+$ patients. Enrichment analysis performed on these proteins revealed specific pathways of interest (Table 4.3).

Table 4.3. Top 10 enriched pathways from WikiPathways and KEGG databases. The highlighted pathways in blue are related to lipid-related pathways.

WikiPathways database (Human) – OA/T2DM- group

Pathway ID	Pathway description	P-value (p)	Adjusted p-value (q)	Combined score
WP3601	composition of lipid particles	4.91E-04	2.58E-02	451.49
WP1533	vitamin B12 metabolism	3.69E-05	8.70E-03	217.78
WP4522	metabolic pathway of LDL, HDL and TG, including diseases	1.61E-03	6.91E-02	214.40
WP12	osteoclast signaling	1.61E-03	7.60E-02	214.40
WP408	oxidative stress	2.55E-04	1.72E-02	200.60
WP3967	miR-509-3p alteration of YAP1/ECM axis	1.82E-03	7.16E-02	197.94
WP176	folate metabolism	1.10E-04	1.04E-02	147.28
WP2911	miRNA targets in ECM and membrane receptors	3.05E-03	1.11E-01	140.40
WP100	glutathione metabolism	3.34E-03	1.13E-01	132.24
WP111	electron transport chain (OXPHOS system in mitochondria)	4.26E-05	6.70E-03	130.27

KEGG database (Human) – OA/T2DM- group

Name	P-value (p)	Adjusted p-value (q)	Combined score
protein digestion and absorption	2.22E-05	6.84E-03	158.74
Riboflavin metabolism	2.96E-02	3.80E-01	117.32
ECM-receptor interaction	2.56E-04	1.58E-02	107.60
glutathione metabolism	1.22E-03	6.25E-02	95.87
oxidative phosphorylation	1.43E-04	1.10E-02	88.73
arachidonic acid metabolism	1.71E-03	6.59E-02	80.90
taurine and hypotaurine metabolism	4.05E-02	4.30E-01	77.74
huntington disease	8.66E-05	1.33E-02	77.55
focal adhesion	1.02E-04	1.05E-02	73.86
fatty acid biosynthesis	4.77E-02	4.90E-01	62.42

WikiPathways database (Human) – OA/T2DM+ group

Pathway ID	Pathway description	P-value (p)	Adjusted p-value (q)	Combined score
WP1589	folate-alcohol and cancer pathway hypotheses	1.79E-02	1	223.62
WP4225	pyrimidine metabolism and related diseases	1.79E-02	1	223.62
WP4146	macrophage markers	1.79E-02	1	223.62
WP206	fatty acid omega oxidation	2.96E-02	1	117.34
WP497	urea cycle and metabolism of amino groups	3.93E-02	1	80.93
WP2533	glycerophospholipid biosynthetic pathway	4.12E-02	1	75.94
WP3580	methionine de novo and salvage pathway	4.31E-02	1	71.45
WP1539	angiogenesis	4.69E-02	1	63.73
WP2878	PPAR alpha pathway	5.08E-02	1	57.32
WP167	eicosanoid synthesis	5.27E-02	1	54.52

KEGG database (Human) – OA/T2DM+ group

Name	P-value (p)	Adjusted p-value (q)	Combined score
fat digestion and absorption	7.49E-05	2.31E-02	347.52
pantothenate and CoA biosynthesis	3.73E-02	1	86.52
renin-angiotensin system	4.50E-02	1	67.40
vitamin digestion and absorption	4.69E-02	1	63.73
alpha-linolenic acid metabolism	4.89E-02	1	60.38
linoleic acid metabolism	5.64E-02	1	49.56
beta-alanine metabolism	6.02E-02	1	45.32
pancreatic secretion	1.64E-02	1	41.93
drug metabolism	1.97E-02	1	36.35
glycine, serine and threonine metabolism	7.70E-02	1	32.04

Interestingly, a high number of lipid-related pathways were found in both OA/T2DM$^-$ (composition of lipid particles; vitamin B12 metabolism; metabolic pathway of LDL, HDL, and TG, including diseases; folate metabolism) and OA/T2DM$^+$ phenotypes (fatty acid omega oxidation; glycerophospholipid biosynthetic pathway; PPAR alpha pathway; eicosanoid synthesis). In particular, composition of lipid particles, vitamin B12 metabolism, and metabolic pathway of LDL, HDL and TG were considered significantly characteristic of the OA/T2DM$^-$ group.

Using the KEGG database, we also identified three lipid metabolic pathways upregulated in the OA/T2DM$^-$ group (riboflavin metabolism; arachidonic acid metabolism; fatty acid biosynthesis). In addition, fat digestion and absorption,

pantothenate and CoA biosynthesis, vitamin digestion and absorption, alpha-linolenic acid metabolism and linoleic acid metabolism were upregulated in the OA/T2DM$^+$ group.

From all the differently regulated proteins, the apolipoprotein A-1 (APOA1) has been found in 4/7 of the lipid metabolic pathways in the OA/T2DM$^-$ group (composition of lipid particles; vitamin B12 metabolism; metabolic pathway of LDL, HDL and TG, including diseases; folate metabolism). APOA1 protein is the major constituent of HDL, and therefore plays a key role in the lipoprotein metabolism. [168] De Seny *et al*. demonstrated the potential pro-inflammatory properties of the protein in the context of OA disease. [169] A higher level of APOA1 was observed in the serum of healthy control individuals compared to OA patients. [170] Moreover, T2DM has been recently correlated with low levels of APOA1 also in the serum. [171]

In the OA/T2DM$^+$ cohort, the phospholipase A2 protein, membrane associated (PLA2G2A) has been found linked to 5/9 lipid metabolic pathways (glycerophospholipid biosynthetic pathway; eicosanoid synthesis; fat digestion and absorption; alpha-linolenic acid metabolism; linoleic acid metabolism). PLA2G2A is an enzyme that hydrolyzes phospholipid species, liberating free fatty acids (most importantly arachidonic acid) and lysophospholipids. Arachidonic acid is the common precursor of the eicosanoids, a family of compounds with multiple roles in the inflammation process. [172] Interestingly, the protein has been found to be linked to T2DM [173, 174] and OA pathologies [175, 176], but no comparison between OA/T2DM$^-$ and OA/T2DM$^+$ groups has been performed so far. The relative intensities of APOA1 and PLA2G2A are displayed in figure 4.2.

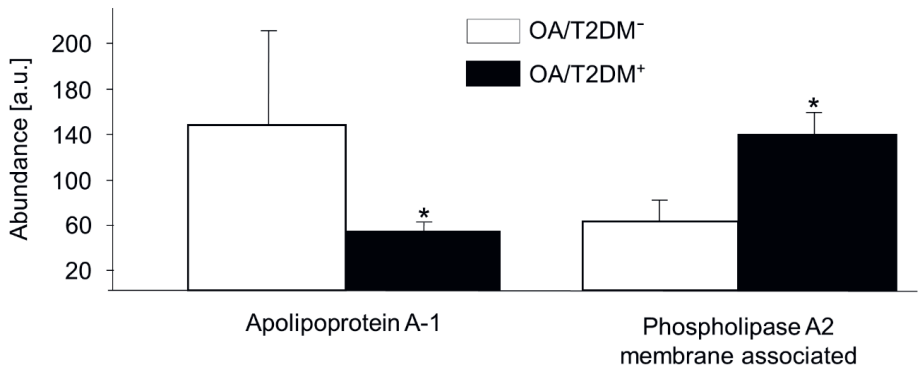

Figure 4.2. Relative intensities of apolipoprotein A-1 and phospholipase A2 proteins in OA/T2DM$^-$ and OA/T2DM$^+$ cohorts. Apolipoprotein A-1 protein has been found increased in the OA/T2DM$^-$ group (FC: 0.31) whereas phospholipase A2 protein has been found increased in the OA/T2DM$^+$ group (FC: 1.9), (*adjusted p-value ≤ 0.05), (n=10).

In addition to lipid metabolic pathways, the proteome analysis implicated other biological processes to be relevant. For instance, four pathways associated with cellular oxidative stress (oxidative stress; glutathione metabolism; oxidative phosphorylation; electron transport chain [OXPHOS system in mitochondria]) have been found increased in the OA/T2DM$^-$ group. This biological process is related to OA disease in the literature. [177-179] The oxidative stress reflects the imbalance between free radicals such as radical oxygen species (ROS) and antioxidants in the body, which can induce inflammatory responses and contribute to the pathophysiology of diseases. [180] Interestingly, the superoxide dismutase (SOD2) and the extracellular superoxide dismutase (SOD3) proteins are associated to these pathways. SOD2 and SOD3 represent two out of three members of the SOD family and are the most important line of antioxidant defense systems against the ROS. [181] In our case, we hypothesized that more ROS could be generated by the coexistence of both OA and T2DM diseases when compared to OA/T2DM$^-$ patients, which might be caused by a lower expression of both SOD2 and SOD3 in OA/T2DM$^+$ patients.

Moreover, to cellular oxidative stress pathways, Extracellular matrix (ECM) related pathways (osteoclast signaling; miR-509-3p alteration of YAP1/ECM axis; miRNA targets in ECM and membrane receptors; ECM-receptor interaction; focal adhesion) have been found enriched in the OA/T2DM$^-$ group. The degradation of ECM is known to be linked to the cartilage loss over the progression of OA pathology. In comparison, site-specific advanced glycation end-products (AGEs) modifications in the ECM proteins have been shown in T2DM disease. [182] Future studies applied on cartilage comparing both phenotypes and targeting specifically the ECM structure should be considered to investigate the key molecules associated to each disease.

Five pathways related to organic compounds metabolism (pyrimidine metabolism and related diseases; urea cycle and metabolism of amino groups; methionine de novo and salvage pathway; beta-Alanine metabolism; glycine, serine, and threonine metabolism) have been found enriched in OA/T2DM$^+$ patients. From these pathways, the organic compounds displayed have been associated with T2DM [183-185], but so far no studies investigated the complete role of these metabolites in the context of the disease.

Lipid profile differences between OA phenotypes

Since lipid regulation is one of the key factors in T2DM disease combined with the fact that several lipid metabolism-related proteins were altered between both OA phenotypes, spatially resolved MALDI-MSI experiments have been performed next. MALDI-MSI is a powerful method to investigate the biomolecular distribution of lipids through cartilage tissue sections. Especially, the technology applied on

cartilage enables the differentiation of the superficial layer and the deep layer of the cartilage, and provides spatial molecular information. [55, 160] This lipid content differences between the two layers have already been studied with another molecular imaging method called Time-of-Flight Secondary Ion Mass Spectrometry (TOF-SIMS). [56] However, this technology causes extensive fragmentation patterns in the mass spectra and need long acquisition times.

The MALDI-MSI experiments followed by PCA-LDA analysis on 1354 spectra showed overall differences between OA/T2DM$^-$ and OA/T2DM$^+$ patients based on their specific lipidomic profiles, with a PCA and DA variances of 38.1% and 1.15%, respectively. The projection of the discriminant function 1 (DF1) scores confirmed the lipid content differences between OA/T2DM$^-$ and OA/T2DM$^+$ patients (figure 4.3A and table 4.4). Interestingly, more lysolipid species were found in OA/T2DM$^+$ whereas sphingomyelin (SM) and phosphatidylcholine (PC) species were more characteristic of OA/T2DM$^-$ patients (figure 4.3B and table 4.4).

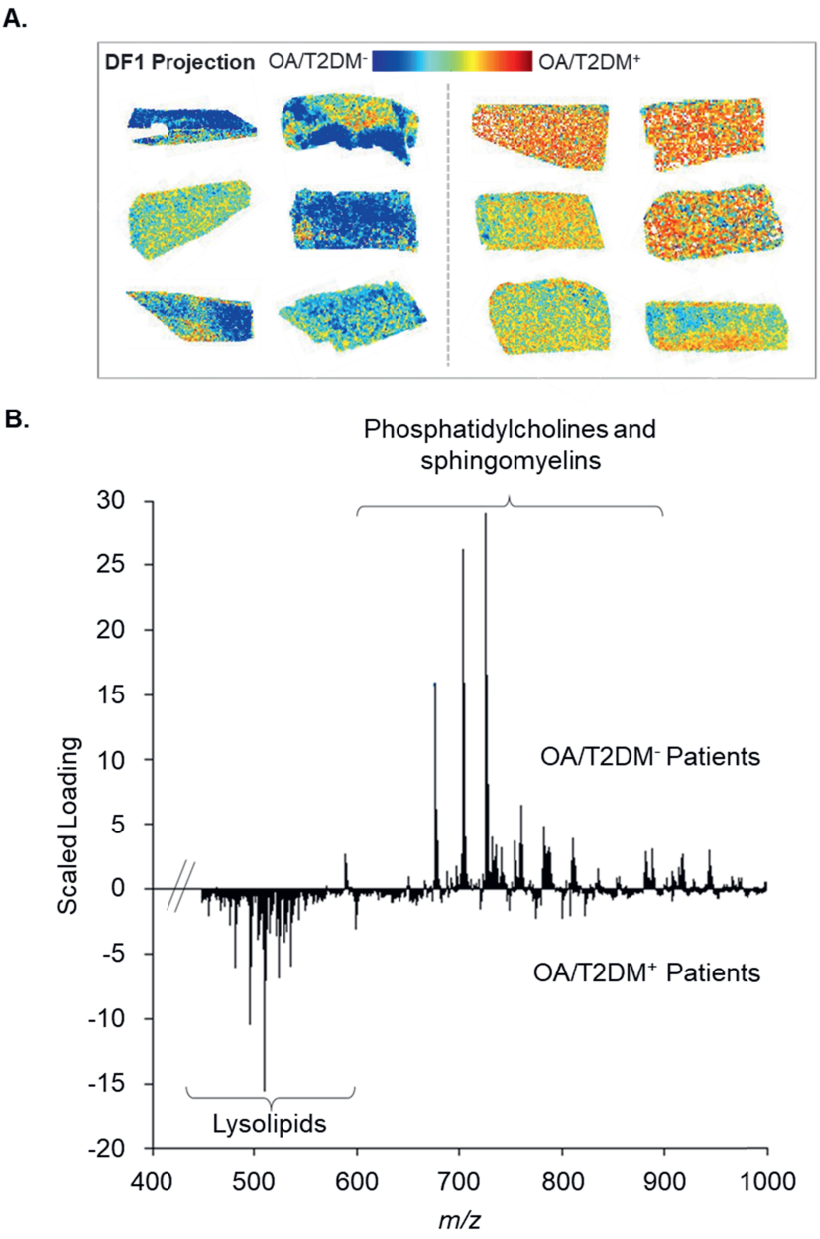

Figure 4.3. Linear discriminant analysis of OA/T2DM- and OA/T2DM+ patients based on specific lipid signature. (**A**) Discriminant function 1 (DF1) score projection. (**B**) DF1 scaled loading spectrum.

Table 4.4. Top 30 of the *m/z* and their corresponding loadings that differentiate the OA/T2DM$^-$ and the OA/T2DM$^+$ conditions.

OA/T2DM- Patients		OA/T2DM+ Patients	
m/z	Scaled loadings	*m/z*	Scaled loadings
725.57	1,50E+07	510.35	-8,22E+06
703.61	1,34E+07	496.34	-4,33E+06
676.80	8,69E+06	511.36	-3,17E+06
726.58	8,59E+06	536.35	-2,69E+06
704.62	8,39E+06	401.09	-2,61E+06
727.59	4,34E+06	524.36	-2,56E+06
760.60	3,64E+06	497.35	-2,52E+06
677.81	3,37E+06	482.33	-2,49E+06
782.56	2,76E+06	508.33	-1,97E+06
731.57	2,26E+06	529.21	-1,72E+06
705.56	2,23E+06	503.21	-1,57E+06
678.49	2,21E+06	440.23	-1,51E+06
810.65	2,19E+06	412.27	-1,40E+06
759.52	2,08E+06	515.20	-1,36E+06
753.59	2,08E+06	525.37	-1,36E+06
735.54	2,01E+06	532.31	-1,36E+06
761.61	2,00E+06	522.41	-1,34E+06
758.58	1,98E+06	505.23	-1,33E+06
786.60	1,98E+06	402.37	-1,30E+06
787.61	1,97E+06	512.31	-1,30E+06
783.57	1,93E+06	430.39	-1,24E+06
732.58	1,82E+06	400.08	-1,21E+06
788.62	1,73E+06	599.13	-1,16E+06
741.54	1,71E+06	476.20	-1,14E+06
784.58	1,64E+06	537.30	-1,12E+06
734.60	1,62E+06	530.22	-1,10E+06
589.23	1,57E+06	483.27	-1,07E+06
887.71	1,55E+06	504.22	-9,80E+05
704.02	1,53E+06	506.24	-9,55E+05
702.33	1,53E+06	543.22	-9,51E+05

MALDI-MSI experiments also revealed overall differences between deep and superficial layers of the cartilage tissues based on their specific lipidomic profiles. PCA followed by LDA was performed, resulting in variances of 38.2% and 8.2%, respectively. The projection of the DF1 scores (figure 4.4A and table 4.5) and the associated loading spectrum (figure 4.4B and table 4.5) confirmed the differences between superficial and deep layers.

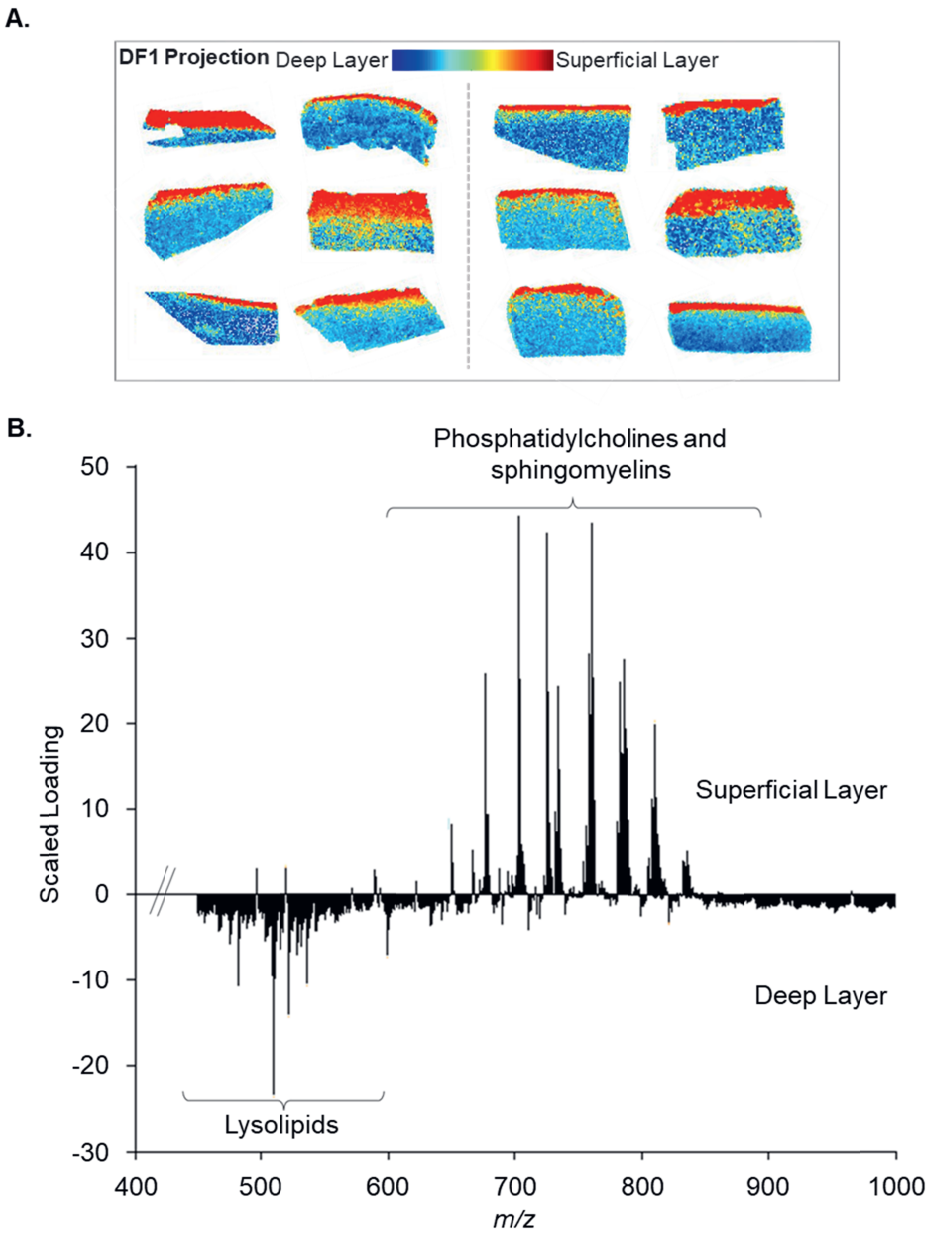

Figure 4.4. Linear discriminant analysis of superficial and deep cartilage layers based on their specific lipid signature. (**A**) DF1 score projection. (**B**) DF1 scaled loading spectrum of the superficial and deep layers of human cartilage.

Table 4.5. Top 30 of the *m/z* and their corresponding loadings that differentiate the superficial layer and the deep layer conditions.

Superficial Layer		Deep Layer	
m/z	Scaled loadings	*m/z*	Scaled loadings
703.61	2,38E+07	510.35	-1,07E+07
725.57	2,29E+07	522.41	-5,69E+06
760.60	2,28E+07	536.35	-4,68E+06
758.58	1,49E+07	482.33	-4,48E+06
786.60	1,49E+07	511.36	-4,39E+06
676.80	1,47E+07	508.33	-4,04E+06
704.62	1,38E+07	529.21	-2,82E+06
761.61	1,35E+07	523.35	-2,75E+06
782.56	1,33E+07	599.13	-2,64E+06
726.58	1,30E+07	532.31	-2,56E+06
734.60	1,30E+07	515.20	-2,49E+06
759.52	1,13E+07	512.31	-2,27E+06
787.61	1,06E+07	401.09	-2,25E+06
810.65	1,05E+07	476.20	-2,20E+06
788.62	9,25E+06	530.22	-2,15E+06
783.57	9,03E+06	537.30	-2,14E+06
784.58	8,90E+06	440.23	-1,97E+06
735.54	8,01E+06	483.27	-1,96E+06
808.63	6,23E+06	509.27	-1,93E+06
762.55	6,16E+06	503.21	-1,80E+06
811.66	6,10E+06	504.22	-1,77E+06
809.64	5,75E+06	477.08	-1,70E+06
732.58	5,55E+06	517.22	-1,68E+06
678.49	5,44E+06	543.22	-1,59E+06
677.81	5,34E+06	467.11	-1,59E+06
785.59	5,32E+06	468.18	-1,58E+06
727.59	5,17E+06	533.32	-1,57E+06
789.63	5,02E+06	505.23	-1,53E+06
756.56	4,67E+06	538.31	-1,52E+06
650.40	4,64E+06	431.14	-1,48E+06

Since MALDI-MSI preserves the spatial molecular information, a second PCA-LDA analysis was performed after manual annotation to compare the superficial and deep layers of both groups independently. These results showed that PCs and SMs species were characteristic of the superficial layers and more abundant in OA/T2DM$^-$ patients whereas lysolipid species were more characteristic of the deep layers and more present in the OA/T2DM$^+$ cohort (Figure 4.5 and table 4.6).

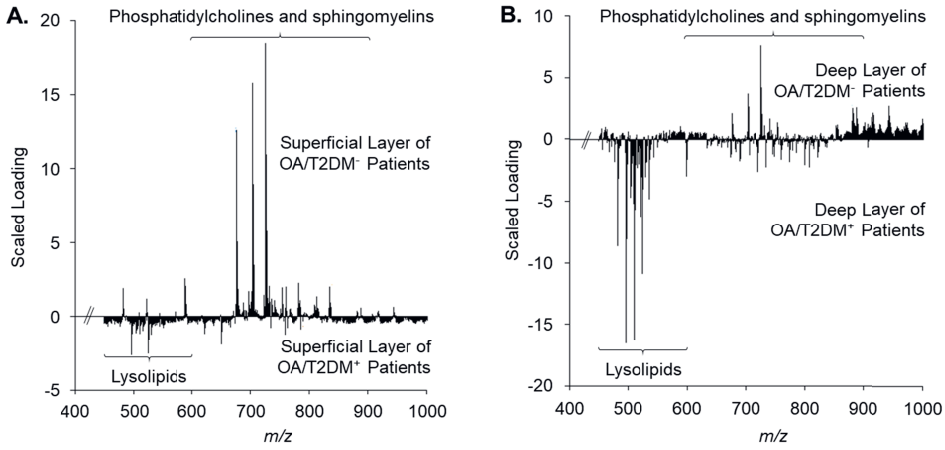

Figure 4.5. Linear discriminant analysis of superficial and deep layers of both groups independently. Discriminant function 1 scaled loading spectrum of (**A**) the OA/**T**2DM^{-} & OA/T2DM^{+} superficial layer and (**B**) OA/T2DM^{-} & OA/T2DM^{+} deep layer.

Table 4.6. Top 30 of the *m/z* and their corresponding loadings that differentiate the OA/T2DM^{-} and OA/T2DM^{+} superficial layers and the OA/T2DM^{-} and OA/T2DM^{+} deep layers.

Superficial Layer OA/T2DM- Patients		Superficial Layer OA/T2DM+ Patients		Deep Layer OA/T2DM- Patients		Deep Layer OA/T2DM+ Patients	
m/z	Scaled loadings	*m/z*	Scaled loadings	*m/z*	Scaled loadings	*m/z*	Scaled loadings
725.57	1,04E+07	496.34	-8,10E+05	725.57	3,30E+06	496.34	-7,90E+06
703.61	8,95E+06	524.36	-7,95E+05	726.58	1,80E+06	510.35	-7,68E+06
676.80	7,38E+06	650.40	-7,43E+05	703.61	1,54E+06	524.36	-5,28E+06
726.58	6,18E+06	525.37	-6,00E+05	704.62	1,16E+06	482.33	-4,03E+06
704.62	5,22E+06	622.31	-4,76E+05	943.75	1,14E+06	497.35	-3,83E+06
727.59	3,39E+06	529.21	-4,67E+05	881.71	1,09E+06	401.09	-3,06E+06
677.81	2,96E+06	402.37	-4,26E+05	887.71	1,09E+06	522.41	-2,98E+06
705.56	2,07E+06	497.35	-4,02E+05	915.73	8,74E+05	511.36	-2,71E+06
760.60	1,66E+06	430.39	-3,97E+05	882.72	8,65E+05	508.33	-2,48E+06
782.56	1,63E+06	503.21	-3,94E+05	676.80	8,12E+05	412.27	-2,37E+06
589.23	1,59E+06	510.35	-3,92E+05	727.59	8,02E+05	536.35	-2,36E+06
731.57	1,36E+06	515.20	-3,63E+05	944.70	7,93E+05	503.21	-2,26E+06
678.49	1,33E+06	651.41	-3,56E+05	917.69	7,93E+05	525.37	-1,98E+06
590.18	1,28E+06	403.32	-3,31E+05	916.68	7,76E+05	505.23	-1,82E+06
835.64	1,27E+06	652.15	-3,24E+05	913.71	7,15E+05	402.37	-1,58E+06
753.59	1,23E+06	428.37	-2,97E+05	888.72	6,46E+05	529.21	-1,52E+06
482.33	1,17E+06	440.23	-2,88E+05	741.54	6,31E+05	483.27	-1,51E+06
702.33	1,10E+06	506.24	-2,88E+05	941.73	6,20E+05	523.35	-1,48E+06
697.55	1,09E+06	623.32	-2,72E+05	879.69	5,90E+05	599.13	-1,40E+06
728.54	1,09E+06	505.23	-2,68E+05	753.59	5,70E+05	504.22	-1,38E+06
735.54	1,01E+06	456.26	-2,66E+05	914.65	5,45E+05	400.08	-1,37E+06
704.02	1,00E+06	550.36	-2,66E+05	945.71	5,32E+05	720.59	-1,33E+06
784.58	9,68E+05	526.32	-2,58E+05	889.66	5,30E+05	430.39	-1,32E+06
813.68	9,06E+05	426.22	-2,49E+05	971.71	5,27E+05	440.23	-1,32E+06
723.48	9,05E+05	517.22	-2,46E+05	901.65	5,25E+05	515.20	-1,16E+06
522.41	8,68E+05	624.19	-2,29E+05	973.73	5,13E+05	734.60	-1,10E+06
729.28	8,53E+05	530.22	-2,25E+05	907.72	5,07E+05	509.27	-1,08E+06
783.57	8,32E+05	476.20	-2,08E+05	883.67	4,98E+05	807.62	-1,06E+06
733.52	8,16E+05	498.29	-2,06E+05	677.81	4,95E+05	512.31	-1,01E+06
701.32	7,48E+05	638.41	-2,01E+05	918.70	4,88E+05	498.29	-9,92E+05

Additional high spatial resolution MALDI-MSI was performed to confirm this differential lipid distribution through the cartilage. Experiments at 15 µm of lateral resolution followed by segmentation and pLSA analysis are in line with the previous data (Figure 4.6) with additional spatial information: transitional layers (represented by yellow and pink colors), lacunae (represented in light blue color) and chondrocyte cells (represented in blue color).

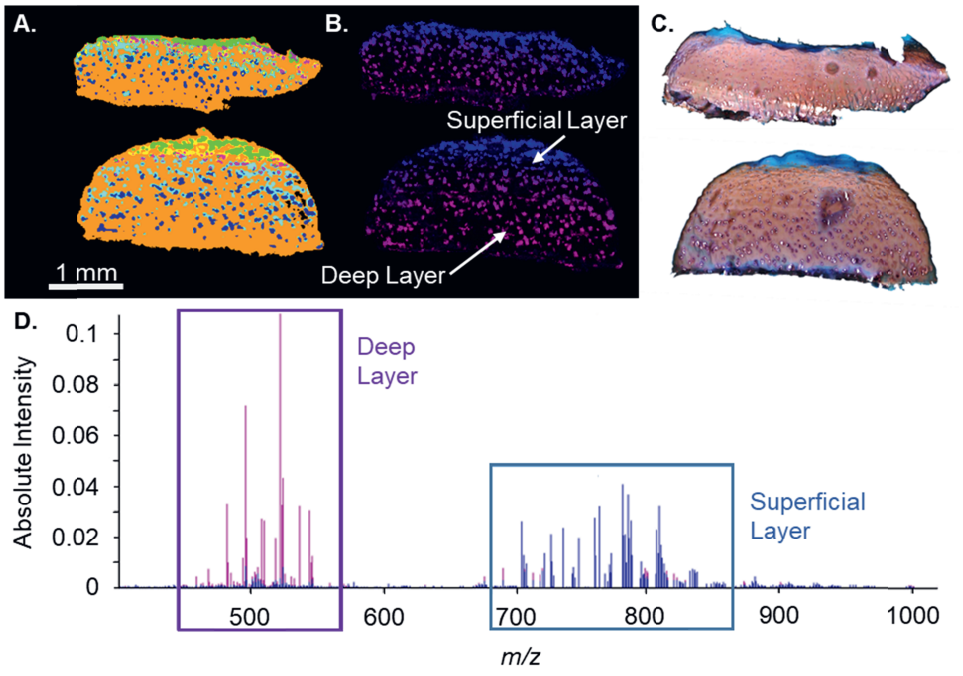

Figure 4.6. µMALDI experiment at 15 µm spatial resolution. (**A**) Segmentation of OA/T2DM$^-$ tissue (top) and OA/T2DM$^+$ tissue (Bottom). The transitional layers are represented by yellow and pink colors, the lacunae in light blue color and the chondrocyte cells in blue color. (**B**) pLSA analysis with random initialization. The superficial layer (blue) is represented by component 1 and the deep layer (purple) is represented by component 4. (**C**) Safranin O staining. (**D**) pLSA loading spectra of selected components 1 and 4.

Finally, targeted MS/MS experiments were performed to identify the lipids of interest that showed significant differences between OA/T2DM$^-$ and OA/T2DM$^+$ phenotypes as well as between superficial and deep layers (Table 4.7). Low abundances prohibited the complete identification of some of the lipids and resulted in tentative assignments.

Table 4.7. Assignments of 15 lipid species based on targeted MS/MS experiments performed at high-mass resolution. (*) 3 lipids were tentatively assigned.

Precursor *m/z*	MS/MS fragments	Assignment	Δppm error	Characteristic of
732.55406	714.59 (H_2O loss) 673.34 ($N(CH3)_3$ neutral loss) 184.00 (Phosphocholine)	$[PC\ 32:1+H]^+$	0.1	Superficial layer
734.56996	716.50 (H_2O loss) 675.34 ($N(CH_3)_3$ neutral loss) 184.00 (Phosphocholine)	$[PC\ 32:0+H]^+$	0.8	Superficial layer
756.55189	697.42 ($N(CH3)_3$ neutral loss) 573.50 (Headgroup neutral loss) 184.00 (Phosphocholine) 146.83 (Cyclophosphane + Na)	$[PC\ 32:0+Na]^+$	0.8	Superficial layer
758.57007	740.42 (H_2O loss) 699.42 ($N(CH_3)_3$ neutral loss) 575.50 (Headgroup neutral loss) 184.00 (Phosphocholine)	$[PC\ 34:2+H]^+$	0.9	Superficial layer
760.58559	742.59 (H_2O loss) 701.42 ($N(CH_3)_3$ neutral loss) 577.42 (Headgroup neutral loss) 184.00 (Phosphocholine)	$[PC\ 34:1+H]^+$	0.7	Superficial layer
780.55218 *	721.50 ($N(CH3)_3$ neutral loss) 597.50 (Headgroup neutral loss) 184.00 (Phosphocholine)	$[PC\ 34:2+Na]^+$	0.3	Superficial layer
782.56773	723.50 ($N(CH_3)_3$ neutral loss) 599.50 (Headgroup neutral loss) 577.33 (Headgroup (Na) neutral loss) 184.00 (Phosphocholine)	$[PC\ 34:1+Na]^+$	0.9	Superficial layer
785.65389	767.59 (H_2O loss) 726.50 ($N(CH_3)_3$ neutral loss) 602.50 (Headgroup neutral loss) 184.00 (Phosphocholine)	$[SM\ 40:2;2+H]^+$	1.0	Superficial layer
786.60121	768.59 (H_2O loss) 727.50 ($N(CH_3)_3$ neutral loss) 184.00 (Phosphocholine)	$[PC\ 36:2+H]^+$	0.6	Superficial layer
787.66935	769.67 (H_2O loss) 728.42 ($N(CH_3)_3$ neutral loss) 604.33 (Headgroup neutral loss) 184.00 (Phosphocholine)	$[SM\ 40:1;2+H]^+$	0.8	Superficial layer
788.61708	770.67 (H_2O loss) 729.42 ($N(CH_3)_3$ neutral loss) 605.42 (Headgroup neutral loss) 184.00 (Phosphocholine)	$[PC\ 36:1+H]^+$	0.9	Superficial layer
806.56757 *	747.50 ($N(CH3)_3$ neutral loss) 623.50 (Headgroup neutral loss) 184.00 (Phosphocholine)	$[PC\ 36:3+Na]^+$	0.4	Superficial layer
703.57548	685.50 (H_2O loss) 644.42 ($N(CH_3)_3$ neutral loss) 184.00 (Phosphocholine)	$[SM\ 34:1;2+H]^+$	0.8	$OA/T2DM^-$ patients
725.55744	707.42 (H_2O loss) 666.42 ($N(CH_3)_3$ neutral loss) 542.42 (Headgroup neutral loss) 184.00 (Phosphocholine)	$[SM\ 34:1;2+Na]^+$	0.8	$OA/T2DM^-$ patients

731.60674	713.59 (H_2O loss) 672.42 ($N(CH_3)_3$ neutral loss) 184.00 (Phosphocholine)	[SM 36:1;2+H]$^+$	0.7	OA/T2DM$^-$ patients
753.58865 *	694.50 ($N(CH3)_3$ neutral loss) 570.25 (Headgroup neutral loss) 184.08 (Phosphocholine)	[SM 36:1;2+Na]$^+$	0.7	OA/T2DM$^-$ patients
552.33050	492.31 ($C_2H_4O_2$ loss) 267.23 (FA 17:1(+O)) 153.00 (Lysophosphocholine)	[LPC 17:1+HCOO]$^-$	0.4	OA/T2DM$^+$ patients & Deep layer
554.34672	494.32 ($C_2H_4O_2$ loss) 269.25 (FA 17:0(+O)) 153.00 (Lysophosphocholine)	[LPC 17:0+HCOO]$^-$	0.7	OA/T2DM$^+$ patients

In parallel to the targeted analysis, a DDA imaging approach has been also used to spatially resolve 19 other lipids at high-mass resolution which have never been found in the cartilage tissue yet (Table 4.8 and figure 4.7).

Table 4.8. Assignments of 19 lipids species based on DDA imaging experiment.

Precursor *m/z*	MS/MS fragments	Assignment	Δppm error
468.3077	450.191 (H_2O loss) 183.950 (Phosphocholine) 104.009 (Choline)	[LPC 14:0+H]$^+$	1.6
494.3234	476.238 (H_2O loss) 183.960 (Phosphocholine) 104.000 (Choline)	[LPC 16:1+H]$^+$	1.4
496.3391	478.267 (H_2O loss) 183.995 (Phosphocholine) 104.022 (Choline)	[LPC 16:0+H]$^+$	1.4
520.3391	502.236 (H_2O loss) 461.193 ($N(CH3)_3$ neutral loss) 183.961 (Phosphocholine) 103.998 (Choline)	[LPC 18:2+H]$^+$	1.3
522.3546	504.255 (H_2O loss) 183.996 (Phosphocholine) 104.026 (Choline)	[LPC 18:1+H]$^+$	1.5
524.3703	506.276 (H_2O loss) 183.997 (Phosphocholine) 104.021 (Choline)	[LPC 18:0+H]$^+$	1.5
675.5426	183.969 (Phosphocholine)	[SM 32:1;2+H]$^+$	1.3
703.5739	685.514 (H_2O loss) 183.963 (Phosphocholine)	[SM 34:1;2+H]$^+$	1.3
705.5896	687.453 (H_2O loss) 183.961 (Phosphocholine)	[SM 34:0;2+H]$^+$	1.3

731.6052	713.601 (H_2O loss) 183.951 (Phosphocholine)	[SM 36:1;2+H]$^+$	1.3
734.5685	183.953 (Phosphocholine)	[PC 32:0+H]$^+$	1.2
758.5685	740.417 (H_2O loss) 699.364 ($N(CH3)_3$ neutral loss) 575.448 (Head group neutral loss) 183.959 (Phosphocholine)	[PC 34:2+H]$^+$	1.3
759.6365	183.965 (Phosphocholine)	[SM 38:1;2+H]$^+$	1.2
760.5841	701.354 ($N(CH3)_3$ neutral loss) 183.965 (Phosphocholine)	[PC 34:1+H]$^+$	1.3
785.6521	726.483 ($N(CH3)_3$ neutral loss) 183.956 (Phosphocholine)	[SM 40:2;2+H]$^+$	1.3
786.5998	727.486 ($N(CH3)_3$ neutral loss) 183.956 (Phosphocholine)	[PC 36:2+H]$^+$	1.2
787.6677	183.943 (Phosphocholine)	[SM 40:1;2+H]$^+$	1.3
813.6833	754.490 ($N(CH3)_3$ neutral loss) 183.967 (Phosphocholine)	[SM 42:2+H]$^+$	1.3
815.699	797.556 (H_2O loss) 183.947 (Phosphocholine)	[SM 42:1+H]$^+$	1.3

Figure 4.7. Spatial distribution of 19 lipids based on DDA imaging experiment.

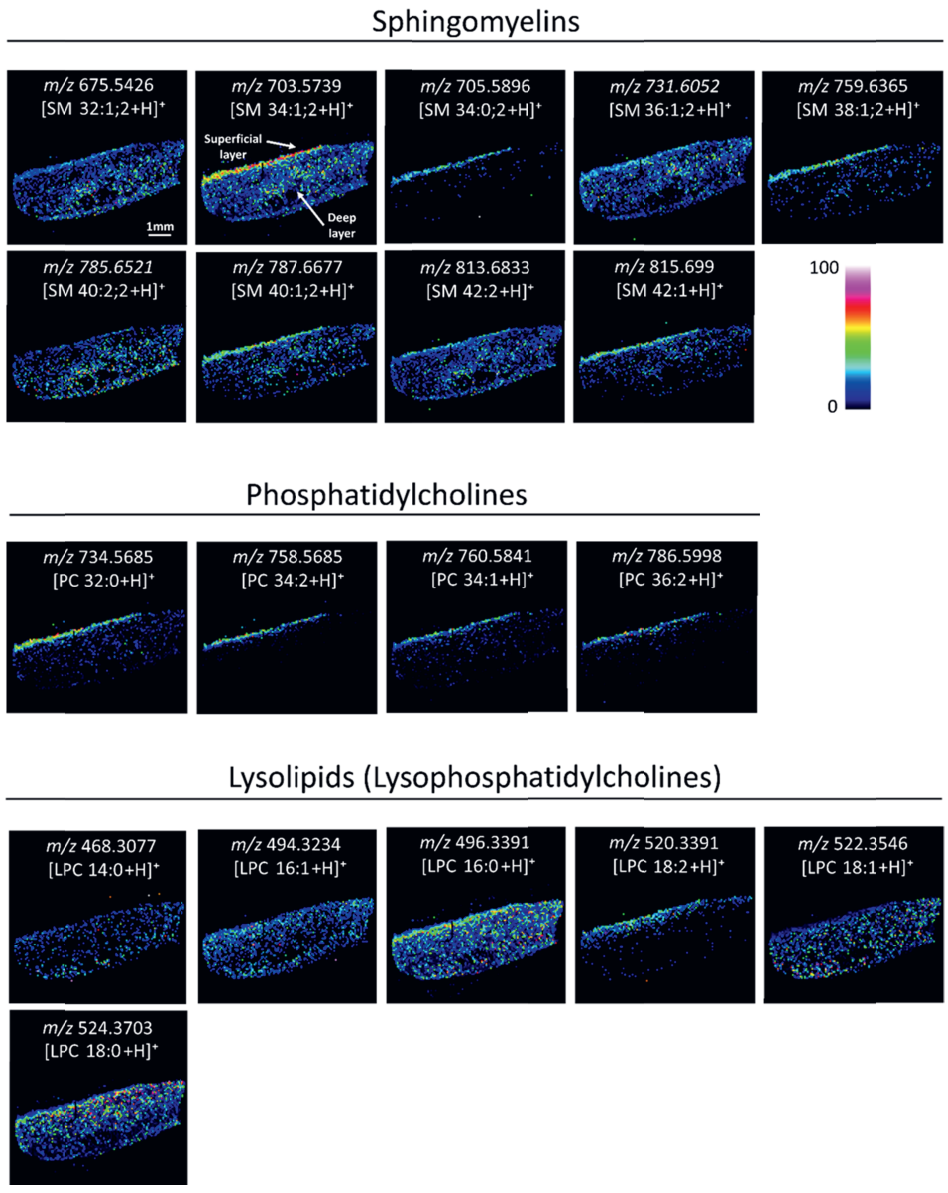

In our study, SMs, PCs, and lysolipids (mostly lysophosphatidylcholines (LPC)) species have been detected. On one hand, SMs are structural components of the cell membrane and play a role in cell growth, cell differentiation, and programmed cell death.[186-188] On the other hand, PCs species are one of the most abundant

phospholipids in all mammalian cell membranes [189] whereas LPCs are lipids with pro-inflammatory properties produced under pathological conditions.[190]

According to Zhang *et al.*, the ratio between LPC and PC in the serum could be used to predict advanced knee OA.[191] Indeed, the activation of the PC to LPC pathway seems to be associated with OA knee cartilage volume loss over time.[175] Here, the higher level of LPC in OA/T2DM$^+$ compared to OA/T2DM$^-$ condition could be linked to the co-existence of the two diseases, accentuating the inflammatory process and the view of the OA pathology as a systemic rather than a local pathology. This hypothesis is supported by studies showing an increased level of LPC in the plasma of diabetes patients [192] and the link between saturated fatty acids to insulin resistance.[193] This insulin resistance can also be associated to the pancreatic secretion pathway found within the OA/T2DM$^+$ group.

Interestingly we also observed a higher abundance of PLA2G2A protein in the OA/T2DM$^+$ group, which could be in line with the higher LPC content also associated with this group. Indeed, studies have found that PLA2G2A protein was enriched in the deep layer of the cartilage, which is supporting this hypothesis as LPCs species have been mainly localized in the same area.[194, 195] We therefore postulated that the overexpression of PLA2G2A protein within the OA/T2DM$^+$ cohort could explain an increased production of lysophospholipids in the deep layers of the cartilage tissue.

PCs and SMs have been mainly detected in the superficial layer of the cartilage. Interestingly, a study conducted by Sarma *et al.* showed that these species were the major components of the lipid layer present at the surface of articular cartilage.[196] This specific localization of PCs and SMs species could also be linked to a different chondrocyte type/role in the superficial and the deep layers.[197] Interestingly, SM 34:1 is the most abundant SM species in synovial fluid (SF) and its level is elevated in OA and rheumatoid arthritis.[198] This specie has been also found in chondrocyte cell pellets cultured in hypoxia condition (2.5% O_2).[51]

4.5. Chapter conclusions

In this study, the main limitation remains the number of patients (n=20) and efforts should focus on the validation of these findings in a larger cohort. In addition, a small sample size restricts the possibility to correct for other biological parameters such as BMI, age or gender differences. Considering this last point, all patients from this study were over weighted or obese.

In summary, in this work we have provided a panel of distinctive proteins and lipids between OA/T2DM$^-$ and OA/T2DM$^+$ phenotypes. Therefore, we clearly showed the need to consider knee OA as a complex disease that requires potentially different and more personalized therapies.

Acknowledgements
This work has been performed as part of the M4I research program that was financially supported by the Dutch Province of Limburg through the "LINK" program and by the MUMC+ institutional grant for clinical collaborative research.

CHAPTER 5

Sox9 determines translational capacity during early chondrogenic differentiation by regulating expression of ribosome biogenesis factors and ribosomal proteins

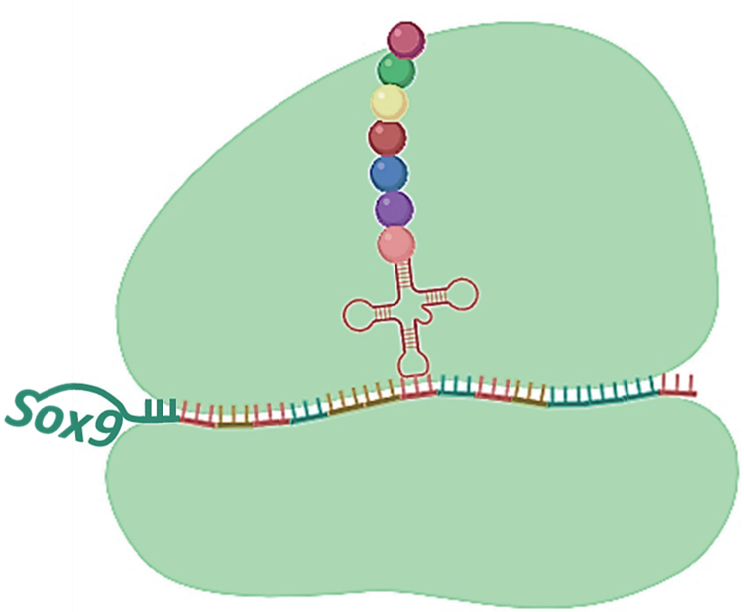

Adapted from:

Sox9 determines translational capacity during early chondrogenic differentiation by regulating expression of ribosome biogenesis factors and ribosomal proteins

Caron MMJ*, Eveque-Mourroux MR*, Cillero-Pastor B, Heeren RMA, Housmans B, Cremers A, Peffers MJ, Van Rhijn LW, Van der Akker G, Welting TJ.

Submitted to Frontiers in Cell and Developmental Biology (**2021**)

5. Sox9 determines translational capacity during early chondrogenic differentiation by regulating expression of ribosome biogenesis factors and ribosomal proteins

5.1. Abstract

In our previous research, we found that in addition to the well-known extracellular matrix-related expression of Sox9, chondrogenic differentiation of progenitor cells is driven by a sharply defined bi-phasic expression of Sox9: an immediate early and a late (extracellular matrix associated) phase expression. The early phase Sox9 expression appeared to be essential in the initiation of chondrogenic differentiation and in this study, we aimed to determine what biological processes are driven by Sox9 during the early phase of chondrogenic differentiation.

Sox9 expression in ATDC5 cells was knocked-down by siRNA transfection at the day before chondrogenic differentiation started or at day 6 in differentiation. Samples were harvested at 2 hours, and 7 days in differentiation. The transcriptome (RNA-seq) and proteome (label-free proteomics) were compared using pathway and network analyses. Total protein translational capacity was evaluated with the SuNSET assay, active ribosomes with polysome profiling and ribosome modus with bicistronic reporter assays.
Early Sox9 knockdown severely inhibited chondrogenic differentiation weeks later. Sox9 expression during the immediate early phase of ATDC5 chondrogenic differentiation regulates the expression of ribosome biogenesis factors and ribosomal protein subunits. To validate functional consequences of siSox9 treatment for ribosome function, we evaluated total translational capacity, polysome profiles and ribosome modus. Translational capacity was decreased by siSox9 treatment and this correlated to lower amounts of active mono- and polysomes. Finally, cap- versus IRES-mediated translation was altered by Sox9 knockdown.

Here we identified an essential new function for Sox9 during early chondrogenic differentiation.

5.2. Introduction

Chondrogenesis, or chondrogenic differentiation, is the cellular process that describes the differentiation path of progenitor cells via early mesenchymal condensation into chondrocytes that synthesize a cartilage extracellular matrix (ECM). [199-201] Aside from articular cartilage formation and maintenance, skeletal development also depends on chondrogenic differentiation. Formation of the long bones of the mammalian skeleton depends on the activity of growth plates; cartilaginous entities at the ends of developing bones in which chondrocytes differentiate from progenitor cells. In contrast to articular

chondrocytes, differentiating growth plate chondrocytes are predestined to undergo hypertrophic differentiation and apoptosis. The remaining cartilage matrix is subsequently remodeled by osteoclastic/osteocytic activity, resulting in *de novo* synthesized bone.[199-201] *In vivo*, chondrogenic differentiation is almost exclusively initiated from local mesenchymal progenitor cells that reside in the cartilaginous tissue (growth plate resting zone[202], articular cartilage superficial layer[203]) or in surrounding fibrous tissues (e.g. periosteum[204, 205]). *In vitro* however, chondrogenic differentiation has been reported from various primary (mesenchymal) progenitor cell sources including synovial fluid/membrane, bone marrow, adipose tissue and induced pluripotent stem cells. [206, 207] In addition to high amounts of oligosaccharides (hyaluronic acid, heparan sulphate, chondroitin sulfate, etc.), important cartilage ECM proteins are type II collagen (Col2a1) and aggrecan (Acan).[200, 208, 209]

The master regulator of chondrogenic differentiation is the transcription factor SRY (sex determining region Y)-box 9 (Sox9). Mutations in *SOX9* were originally identified as the cause for campomelic dysplasia[210, 211], a severe skeletal dysplasia associated with XY sex reversal and disproportionally short stature as well as general lack of cartilaginous tissue formation. *SOX9* was found to be essential for murine early chondrogenic lineage determination.[212] Upon nuclear translocation [213, 214], Sox9 binds as a homodimer to its consensus DNA recognition sequence (A/T)(A/T)CAA(A/T)G[215], which includes the highly conserved AACAAT motif recognized by the HMG-box domain shared amongst Sox and Sry protein family members. In chondrogenic differentiation Sox9 drives the transcription of and cooperates with L-Sox5 and Sox6 for efficient transcription of the *COL2A1* and *ACAN* genes.[212, 216-219] Other ECM genes have also been shown to be under transcriptional control of Sox9; including *COL9A1*[220], *COL27A1*[221], and *MATN1*.[222] [223] Besides L-Sox5 and Sox6, another important factor for Sox9-mediated transcription is Smad3, which modulates the interaction between Sox9 and CBP/p300[224], thereby possibly explaining the pro-chondrogenic effect of BMPs and TGFβs on chondrogenic differentiation.

During chondrogenic differentiation of progenitor cells *in vitro*, induction of Sox9 expression is biphasic.[225] In the first hours after initiation of chondrogenic differentiation Sox9 expression is transiently induced (immediate early Sox9 induction), together with the other members of the "Sox-trio". Sox9 expression increases a second time in parallel with the synthesis of ECM molecules (late Sox9 induction). Previously, we showed that this immediate early Sox9 expression is in part regulated by the immediate early response gene 1 (Egr1)[226] as well as by NFκB/p65.[227] Similar expression patterns were also found in growth plate sections.[227] The function of the early Sox9 induction itself remains elusive at present. In the present work we therefore determined the transcriptomic and proteomic consequences of the abrogation of early Sox9 expression during ATDC5 chondrogenic

differentiation, and uncovered the biological processes that are driven by Sox9 during the early phase of chondrogenic differentiation.

5.3. Materials and methods

ATDC5 cell culture

ATDC5 cells (RIKKEN BRC, Japan)[228] were cultured in a humidified atmosphere at 37°C and 5% CO_2 in culture media consisting of Dulbecco's Modified Eagle Medium (DMEM)/F12 (Life Technologies, MA, USA), 5% fetal calf serum (Life Technologies), 1% antibiotic/antimycotic (Life Technologies) and 1% non-essential amico acids (NEAA) (Life Technologies). ATDC5 cells provide a good model system to understand chondrogenic differentiation as they produced cartilage-specific proteoglycan and type II collagen. The Chondrogenic differentiation was induced by plating the cells in triplicates at 6.400 cells/cm^2, or 20.000 cells/cm^2 in transfection experiments, and addition culture media with differentiation supplements 10 µg/ml insulin (Sigma-Aldrich, MO, USA), 10 µg/ml transferrin (Roche, Basel, Switzerland), and 30 nM sodium selenite (Sigma–Aldrich). Medium was refreshed every two days. A small interfering RNA (siRNA) duplex for Sox9 ("Sox9 RNAi") (sense: 5'-GACUCACAUCUCUCCUAAUTT-3', anti-sense: 5'-AUUAGGAGAGAUGUGAGUCTT-3') and a scrambled siRNA duplex ("Control RNAi", Eurogentec, Seraing, Belgium) were transfected (100 nM) one day prior to initiation of chondrogenic differentiation or at day 6 in differentiation using HiPerFECT according to manufacturers' protocol (Qiagen, Hilden, Germany).

RNA isolation

RNA was isolated using TRIzol reagent (Life Technologies) and collecting the aqueous phase after centrifugation. RNA was precipitated with isopropanol (-80°C) and pellet by centrifugation. RNA pellets were washed in 80% ethanol and dried. RNA was dissolved in DNase/RNase-free pure water. RNA quantity and purity were determined spectrophotometrically (Biodrop, Isogen Life Sciences, Utrecht, The Netherlands).

Quantitative real time PCR

Total RNA was reverse transcribed to cDNA using standard procedures and random hexamer priming as previously described.[229] Real-time quantitative PCR (RT-qPCR) was performed using Mesagreen qPCR master mix plus for SYBR Green (Eurogentec). A CFX96 Real-Time PCR Detection System (Biorad, CA, USA) was used for amplification: initial denaturation 95°C for 10 minutes, followed by 40 cycles of amplification (denaturing 15 seconds at 95°C and annealing 1 minute at 60°C). Validated primer sequences are shown in table 5.1. Data were analyzed using the standard curve method,

mRNA expression was normalized to a reference gene (β-Actin) and gene expression was calculated as fold change as compared to control conditions or t=0.

Table 5.1. Primer sequences for RT-Qpcr. The 5′ to 3′ forward and reverse oligonucleotide sequences used for RT-qPCR are listed in the table.

Oligo sets	Forward	Reverse
Col2a1	TGGGTGTTCTATTTATTTATTGTCTTCCT	GCGTTGGACTCACACCAGTTAGT
Sox9	AGTACCCGCACCTGCACAAC	TACTTGTAGTCCGGGTGGTCTTTC
18S rRNA	AGTCCCTGCCCTTTGTACACA	GATCCGAGGGCCTCACTAAAC
28S rRNA	GCCATGGTAATCCTGCTCAGTAC	GCTCCTCAGCCAAGCACATAC
5.8S rRNA	CACTCGGCTCGTGCGTCGAT	CGCTCAGACAGGCGTAGCCC
β-Actin	GACAGGATGCAGAAGGAGATTACTG	CCACCGATCCACACAGAGTACTT

RNA-sequencing and analysis

Isolated RNA was checked for quality and integrity on the Agilent 2100 Bioanalyzer (TM) via 2100 an Expert Eukaryote Total RNA Nano chip according manufacturer's protocol. The mRNA sequencing library was generated using TruSeq mRNA sample preparation kit (Illumina, CA, USA). In short, mRNA was enriched using magnetic beads coated with poly-dT, followed by fragmentation. The fragmented mRNA enriched samples were subjected to cDNA synthesis by reverse transcriptase, followed by dA-tailing and ligation of specific double-stranded bar-coded adapters. Next, the library was amplified and after cleanup the sizes of the libraries were determined on an Agilent 2100 Bioanalyzer (TM) via an DNA 1000 chip according manufacturer's protocol. Pooled libraries consisting of equal molar samples were sequenced on a high-output 75bp single read on the NextSeq500 (Illumina). For each sample, the number of reads covering one or more exons of a given transcript were extracted. Triplicates of samples that were treated with either Scrambled or Sox9 siRNAs, at two different time points, were grouped separately. A transcript was defined as expressed when all replicates of a group had at least 5 reads extracted within the transcript's region. After which the grouped data were compared to one another. The fold change difference and the p-value were calculated using R-package edgeR [230, 231], after which the p-value was corrected for multiple testing (false discovery rate (FDR)-corrected). Transcripts having an FDR-corrected p-value <0.05, and a fold change of at least 1.5 were considered differentially expressed transcripts. EnrichR[163] software was used to display the pathways of interest obtained from the enrichment of down or up-regulated proteins. The top three pathways of interest were considered from both Wikipathways and KEGG software (version 2019, Human) based on the combined score of the p-value and the adjusted p-value scores.

Label-free proteomics – Protein extraction, reduction and alkylation

At indicated time points, plates were rinsed 3 times with 1% phosphate buffered saline (PBS). A mixture containing cOmplete Mini Protease Inhibitor Cocktail (Roche) in 25 mM ammonium bicarbonate (ABC) buffer (Sigma-Aldrich) and 6M urea (GE Healthcare, Eindhoven, The Netherlands) was added to the plates. Cells were collected by scraping with a rubber policeman and the samples were transferred to Eppendorf tubes. Triplicates were pooled and sonicated for 10 minutes and centrifuged at 12.000g for 10 min in 4°C. the supernatant containing proteins was finally transferred into new tubes and stored at -80° until further analysis. Bradford assay (Biorad) was performed to assess protein concentration. The concentrations were adjusted to 0.2µg/µL in order to normalize for the following steps.
Samples were reduced with 20mM of DTT (Sigma-Aldrich) in 100 mM ABC for 45 min and alkylated with 40 mM of IAM (Sigma-Aldrich) in 100 mM ABC for 45 minutes in the dark. The alkylation step was stopped by adding 20 mM of DTT. Samples were then digested by a mixture of LysC and trypsin (Promega, Leiden, The Netherlands) added at a ratio of 1:25 (enzyme:protein) and incubated for 2h at 37°C in a water bath. Finally, 200 µL of 25 mM ABC buffer was added to the samples before overnight incubation at 37°C. The digestion was stopped by adding formic acid (FA) (Sigma-Aldrich) and acetonitrile (Biosolve, Valkenswaard, the Netherlands) at a final concentration of 1% and 2%, respectively.

Label-free proteomics – Data acquisition and processing

200 ng of each sample were injected in duplicate for liquid-chromatography mass spectrometry (LC-MSMS) analysis. The separation of the peptides was performed on a Thermo Fisher Scientific Dionex Ultimate 3000 Rapid Separation ultrahigh-performance liquid-chromatography (HPLC) system (Thermo Scientific, MA, USA) equipped with an Acclaim PepMap C18 analytical column (2µm, 75µm*150 mm, 100Å). The samples were first trapped on an online C18 column for desalting. The peptides were then separated on the analytical column with a 90-min linear gradient from 5% to 35% acetonitrile/0.1% FA and a flow rate set at 300 nL/min. The HPLC system was coupled to a high-mass resolution orbitrap MS Q-exactive instrument (Thermo Scientific). The mass spectrometer was operated in data-dependent acquisition (DDA) mode with the following settings: Full MS scan of the mass range *m/z* 350-1,650 at a resolution of 120,000 at *m/z* 400, followed by tandem mass spectrometry (MS/MS) scans for the fragmentation of the 15 most intense ions at a resolution of 30,000. The ions already selected for fragmentation were dynamically excluded for 20s. External calibration of the instrument was performed using a standard calibration solution for positive ion mode (Thermo Scientific).

For protein identification, raw files were processed within the Proteome Discoverer software version 2.2 (Thermo Scientific) using the search engine Sequest with the Swiss-Prot database *Mus musculus* version 2017-10-25 (TaxID 10090). The following parameters

were used for the database search: Carbamidomethylation of C for fixed modifications; oxidation of M and acetylation of protein *N*-term for variable modifications; trypsin for enzyme with a maximum of two missed cleavages; the precursor mass tolerance was set at 10 ppm and the fragment tolerance at 0.02 Da; minimum and maximum peptide length of 6 and 144 amino acids, respectively. Normalization of the data was performed on the total peptide amount. Percolator was used for the decoy database search and the FDR was fixed at 1% maximum. For protein quantitation, the Minora Feature Detector node in the processing step and the Feature Mapper node combined with the Precursor Ions Quantifier node in the consensus step were used with default settings. Finally, a list of 23 commonly detected contaminants were removed manually (Table 5.2).

Table 5.2. List of the 23 contaminants.

Protein ID	Protein Name
Q8IUC1	Keratin-associated protein 11-1
P78385	Keratin, type II cuticular Hb3
A0A075B6S5	Immunoglobulin kappa variable 1-27
Q8N1N4	Keratin, type II cytoskeletal 78
P01859	Immunoglobulin heavy constant gamma 2
O95678	Keratin, type II cytoskeletal 75
P01860	Immunoglobulin heavy constant gamma 3
A0A0C4DH68	Immunoglobulin kappa variable 2-24
P48668	Keratin, type II cytoskeletal 6C
O76013-1	Keratin, type I cuticular Ha6
A0A0C4DH31	Immunoglobulin heavy variable 1-18
P01824	Immunoglobulin heavy variable 4-39
P0DOX5	Immunoglobulin gamma-1 heavy chain
P13645	Keratin, type I cytoskeletal 10
Q04695	Keratin, type I cytoskeletal 17
P68871	Hemoglobin subunit beta
P0DOX7	Immunoglobulin kappa light chain
P04264	Keratin, type II cytoskeletal 1
P35908	Keratin, type II cytoskeletal 2 epidermal
A0A0B4J1X5	Immunoglobulin heavy variable 3-74
P80748	Immunoglobulin lambda variable 3-21
P01614	Immunoglobulin kappa variable 2D-40
A0A0B4J1V1	Immunoglobulin heavy variable 3-21

Label-free proteomics – Data analysis

ANOVA test and principal component analysis (PCA) were performed within the Proteome Discoverer software. ANOVA test was used to analyze the statistical significance of variation observed in protein abundance between the two conditions. PCA

was performed on the abundance of all quantified protein to confirm and visualize the statistical significance of the protein abundance changes. The proteins were considered modulated with a p-value ≤ 0.05 and a fold change (FC) cut-off set at 2-fold. The modulated proteins were then imported within the EnrichR software [163] to display the top 3 pathways of down or up-regulated proteins ranked by the combined score. WikiPathways and KEGG were used as databases (version 2019, Mouse).

Immunoblotting

Cells were lysed in RIPA buffer (150 mM NaCl, 1% NP-40, 0,5% Sodium deoxycholate, 0,1% SDS, 50 mM Tris pH 8.0, 5.0 mM Ethylenediaminetetraacetic acid (EDTA) pH 8.0, 0.5 mM dithiothreitol (DTT) supplemented with cOmplete Mini Protease Inhibitor Cocktail (Roche) and PhosSTOP phosphatase inhibitor (Sigma-Aldrich)). Extracts were sonicated and protein concentrations were determined with a bicinchoninic acid assay (BCA) assay (Sigma-Aldrich). Proteins were separated by SDS-PAGE and transferred to nitrocellulose membranes by electroblotting. Primary antibodies for immunodetection were anti-Sox9 (Abcam, Cambridge, UK) and anti-Tubulin (Sigma-Aldrich). Bound primary anti-bodies were detected using immunoglobulins conjugated with HRP (DakoCytomation, Glostrup, Denmark) and visualized by enhanced chemoluminescence (ECL).

sGAG assay

The sulphated glycosaminoglycan (GAG) content was measured using a modified dimethyl methylene blue (DMB) assay.[232] The absorbance of samples was read at 540 and 595 nm using a spectrophotometer (Multiskan FC, Life Technologies) and GAG concentrations were calculated using a chondroitin sulfate standard curve (Sigma-Aldrich) and corrected for total protein content with a BCA assay.

SUnSET assay

Protein translational capacity of ATDC5 cultures (in sextuplicates) was assessed with the SUnSET assay.[233, 234] 5.4 µM puromycin (Sigma-Aldrich) was incubated for 15 minutes in the cell culture medium, immediately followed by washing in PBS and fixation for 20 minutes with 10% formalin (VWR, Radnor, PA, USA). Permeabilization was performed for 10 minutes with 0.1% Triton X-100. Wells were rinsed with PBS with 0.1% Tween (PBS-T) and blocked for 1.5 hour with 1% (m/v) skimmed milk powder (ELK, Campina, Zaltbommel, the Netherlands) in PBS-T, followed by overnight incubation at 4°C with the primary anti-puromycin antibody 12D10 (Sigma-Aldrich). After washing with PBS-T, wells were incubated for 1 hour at room temperature with the secondary goat anti-mouse Alexa488 antibody (Life Technologies). The fluorescent signal intensity was determined using a Tristar LB942 (Berthold, Bad Wildbad, Germany) equipped with excitation filter F485 and emission filter F353. Fluorescent data was normalized to DNA-content from the

same well.[235] To this end, wells were washed with HEPES-Buffered Saline (HBS), followed by 1 hour incubation with 5 µg/mL DAPI (Life Technologies) plus 5 µg/mL HOECHST 33342 (Life Technologies) in HBS. After subsequent washing steps with HBS, fluorescent signal intensity was determined using a Tristar LB942 (Berthold), using the excitation filter F355 and emission filter F460.

Polysome fractionation

Polyosome fractionation was performed basically as described previously. [236] Three 15 cm plates with ATDC5 cells were used to generate a single sample. At the day of sample collection, cells were differentiated for 2 hours, then pre-treated for 5 minutes with 100 µg/ml Cycloheximide (Sigma-Aldrich), washed twice in 0.9% NaCl with Cycloheximide and collected by scraping with a rubber policeman in cold 0.9% NaCl. Pelleted cells were lysed for 10 minutes in 1.8 ml polysome extraction buffer (20 mM Tris-HCl (pH7.5), 100 mM KCl, 5 mM MgCl2, 0.5% Nonidet P-40, 100 µg/ml Cycloheximide, complete protease inhibitor cocktail (Roche) and RNasin (Promega, 40U/ml)) on ice. Nuclei and cellular debris were removed by centrifugation at 12.000x g for 10 minutes at 4□C and 9/10th of the total volume was transferred to fresh tubes and measured spectrophotometrically (Nanodrop). Total yield was the same for siCtrl and siSox9 treated cells. Sucrose gradients (linear 10-50%) were made with the Gradient Master (BioComp, Fredericton, Canada) in ultracentrifuge tubes (Seton, SW41 tubes). Cytoplasmic extracts (250 µg/sample) were loaded to each gradient in a fixed volume (400 µl). Gradients were run on an ultra-centrifuge (Beckman L60) at 39.000 rpm for 1.5 hours at 4□C with max acceleration and deceleration 9. Samples were fractionated into 24 x 0.5 ml fractions using a Piston Gradient fractionator (BioComp) and fraction collector (Gilson FC203B, WI, USA) with continuous A_{260} monitoring.

Bicistronic reporter assay

Reporter constructs for the CrPv IGR IRES, the CrPv CCGG IGR IRES mutant, the HCV and the P53 IRES were a kind gift of Dr. S. Thompson. One day post plating, maxi-prep DNA (0.5 µg/well) and 100 nM siRNA were transfected into 24-wells wells (n=3/group) using Mirus Transit-X2 according to manufacturer's instructions. The next day differentiation was induced for 24 hours, samples were collected by washing cells with 0.9% NaCl and incubation in 100 µl passive lysis buffer for 15 minutes (Promega). Subsequently, samples were transferred to Eppendorf tubes and centrifuged for 10 minutes at 12.000x g in a tabletop centrifuge. Next, 50 µl lysate was used for dual luciferase measurements (Promega) using a Berthold injection system (10 seconds counting time per cistron). Data is represented as fold change (FC) of the ratio Fluc/Rluc in control cells for each IRES.

Statistics in other than proteomics or transcriptomic analysis

Statistical significance was determined by two-tailed student t-tests using Graphpad PRISM 5.0 (Graphpad, CA, USA). Due to small sample size (n=3 samples) normal distribution of input data was assumed. Error bars in graphs represent mean ± standard error of the mean. Significance for all tests was set at $p \leq 0.05$.

5.4. Results and discussion

Early chondrogenic lineage commitment during mesenchymal condensation is driven by Sox9.[212, 237, 238] Following lineage commitment, Sox9 is a key regulator of cartilage extracellular matrix (ECM) synthesis, by driving expression of ECM molecules like Acan, Col2a1 and others.[212, 216-223] Sox9 also safeguards maintenance of cartilage homeostasis by influencing chondrocyte Nkx3-2 levels, a transcriptional repressor of chondrocyte hypertrophy.[239, 240] This dual action of Sox9 is recapitulated in in vitro models of chondrogenic differentiation, as we have previously reported on bi-phasic expression dynamics of Sox9 in ATDC5 and BMSC chondrogenic differentiation.[225, 226] In this earlier work we demonstrated that early (hours) transient induction of Sox9 expression by NFκB/p65 or Egr1 in ATDC5 chondrogenic differentiation is a prerequisite for late-stage (days) expression of cartilage ECM genes. As key transcription factor for cartilage, the vast majority of investigations on the downstream function of Sox9 have mainly focused on its role in the transcriptional regulation of cartilage ECM genes.[212, 216-223] In addition, a function in epigenetic reprogramming has been suggested for early Sox9 [226] , as well as a role for Sox9 in activating super-enhancers in chondrocyte cells.[241] However, its downstream cell biological consequences during early chondrogenic differentiation are incompletely understood. The present study demonstrates that Sox9 expression during the early phase of ATDC5 chondrogenic differentiation regulates the expression of ribosomal protein subunits, as well as proteins that are involved in ribosome biogenesis that modulates ribosome activity and translation mode. These data, for the first time, connect the Sox9 transcription factor to regulation of protein translation during chondrogenic differentiation.

Early Sox9 peak in ATDC5 chondrogenic differentiation

During chondrogenic differentiation of progenitor cells in vitro, induction of Sox9 expression is bi-phasic.[225, 226] In the first (2-4) hours after initiation of chondrogenic differentiation of ATDC5 cells, Sox9 expression is transiently induced on mRNA (Figure 5.1A) and protein level (Figure 5.1B). Sox9 expression increased a second time in differentiation around day 7 in differentiation (Figure 5.1A), in parallel with the expression of the important Sox9 transcriptional target Col2a1[218] (Figure 5.1C) and glycosaminoglycan (GAG) content (Figure 5.1D).[200, 216] The immediate early transient Sox9 expression peak at 2 hours in differentiation does not correlate with the induction of expression of well-known Sox9 transcriptional targets such as Col2a1. Hence, we

questioned what the function of the early Sox9 expression peak (2 hours) is and how it differs from the later Sox9 activity (day 7) by performing a loss-of-function experiment and comparing the transcriptome and proteome in an unbiased manner.

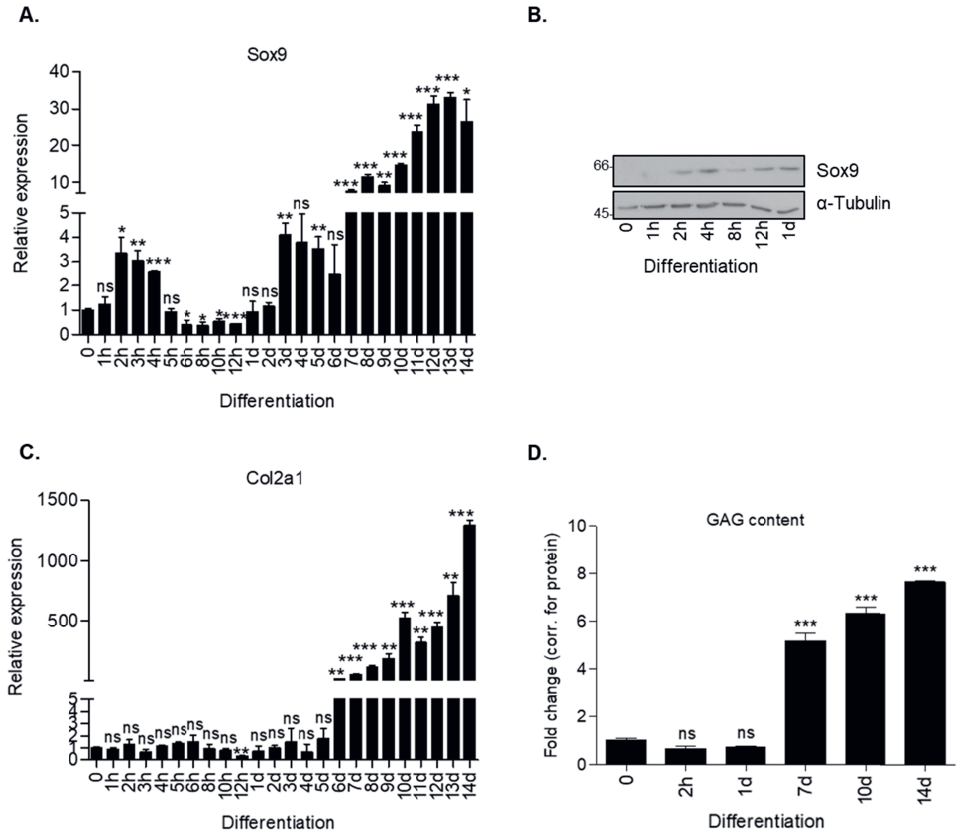

Figure 5.1. Sox9 expression has a bi-phasic peak expression during chondrogenic differentiation of ATDC5 cells. (**A**) Sox9 mRNA expression showed bi-phasic peak pattern during ATDC5 differentiation (h=hours, d=days) as measured by RT-qPCR. Results were normalized to β-Actin RNA expression and presented relative to t=0. (**B**) Sox9 protein expression peak during early ATDC5 differentiation as measured by immunoblotting. α-Tubulin was used as loading control. Molecular weight markers (in kDa) are shown on the left. (**C**) In similar samples from (**A**), Col2a1 mRNA expression was measured during ATDC5 differentiation by RT-qPCR and showed an increase in expression from day 6 onwards. (**D**) GAG content (by Alcian Blue staining and corrected for total protein expression) was determined during ATDC5 differentiation. Experiments were performed in triplicates, bars represent mean±SEM. ns= not significant, *=p<0.05, **=p<0.01, p=<0.0001.

Transcriptome and proteome analysis at 2 hours and 7 days in ATDC5 differentiation under Sox9 knockdown

To specifically target early Sox9 expression, an siRNA for Sox9 or scrambled control siRNA were transfected one day prior to initiation of differentiation (t = -1d) (Figure 5.2A). At t=0 chondrogenic differentiation was induced and cells were differentiated for 14 days. We established effective knockdown of Sox9 at t=0 and t=2 hours in differentiation, while at day 5, 7 and 14 in differentiation Sox9 mRNA levels were back to scrambled siRNA control conditions (Figure 5.2B; black bars and Figure 5.2C). In parallel, ATDC5 cells were differentiated and an siRNA for Sox9 or control scrambled siRNA were transfected at day 6 in differentiation, to specifically target "late" Sox9 induction. Effective knockdown of Sox9 at day 7 and day 14 at mRNA level was observed (Figure 5.2B; grey bars) and on protein level (Figure 5.2C). To understand the function of the immediate early Sox9 expression at 2 hours in differentiation as compared to the late Sox9 induction present at day 7 in differentiation, we now used an unbiased transcriptomics and proteomics approach. Differential expression of mRNAs and proteins was determined between the control scrambled siRNAs condition versus Sox9 siRNA knockdown condition at 2 hours and at 7 days in ATDC5 differentiation (Figure 5.2D).

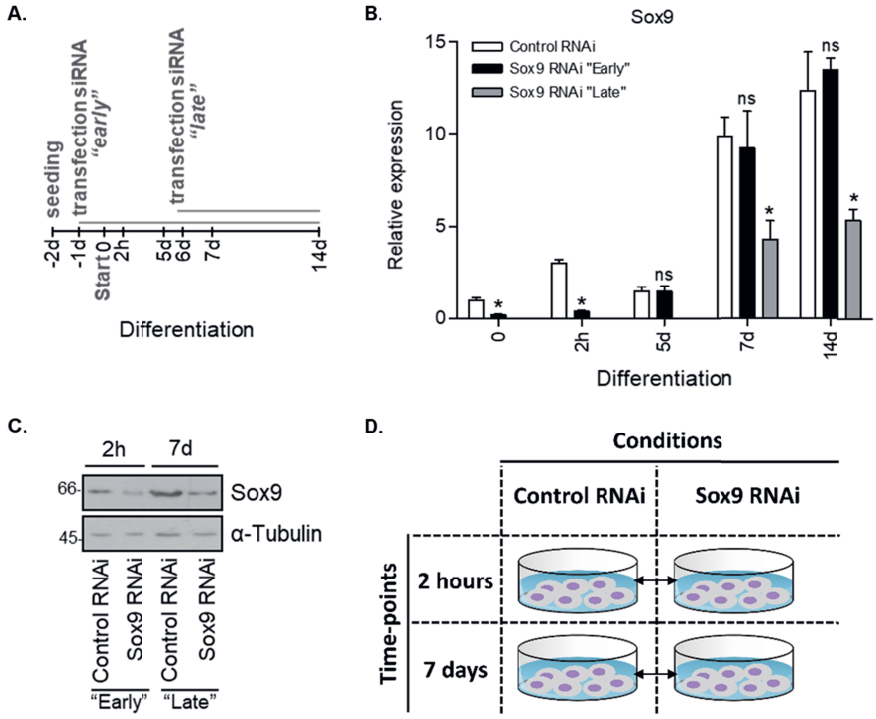

Figure 5.2. Elucidating the function of early Sox9 expression by transcriptome and proteome analyses. (**A**) Schematic representation of experimental set-up for Sox9 knockdown experiment. Specific Sox9 RNAi (100 nM) or scrambled control RNAi (100 nM) were transiently transfected "early" at t=-1d or "late" t=6d. ATDC5 cells were differentiated from day 0 onwards and harvested for transcriptome and proteome analysis at t=0, 2h, 5d, 7d, 14d. (**B**) Sox9 mRNA expression during ATDC5 differentiation in Control and Sox9 RNAi conditions (h=hours, d=days) as measured by RT-qPCR. Results were normalized to β-Actin

RNA expression and presented relative to t=0. Bars represent mean±SEM. ns= not significant, *=p<0.05, **=p<0.01, p=<0.0001. (**C**) Sox9 protein expression at t=2h (for "early knockdown condition) and t=7d (for "late" knockdown conditions) time point in Control and Sox9 RNAi conditions as measured by immunoblotting. α□Tubulin was used as loading control. Molecular weight markers (in kDa) are shown on the left. (**D**) Schematic representation of time points and comparisons for transcriptomics and proteomics analysis.

The extracted RNA was used for RNA sequencing and Principal Component Analysis (PCA) confirmed that samples from control scrambled siRNA conditions at 2 hours and at 7 days were separated from Sox9 siRNA knockdown samples at 2 hours and 7 days (Figure 5.3A).

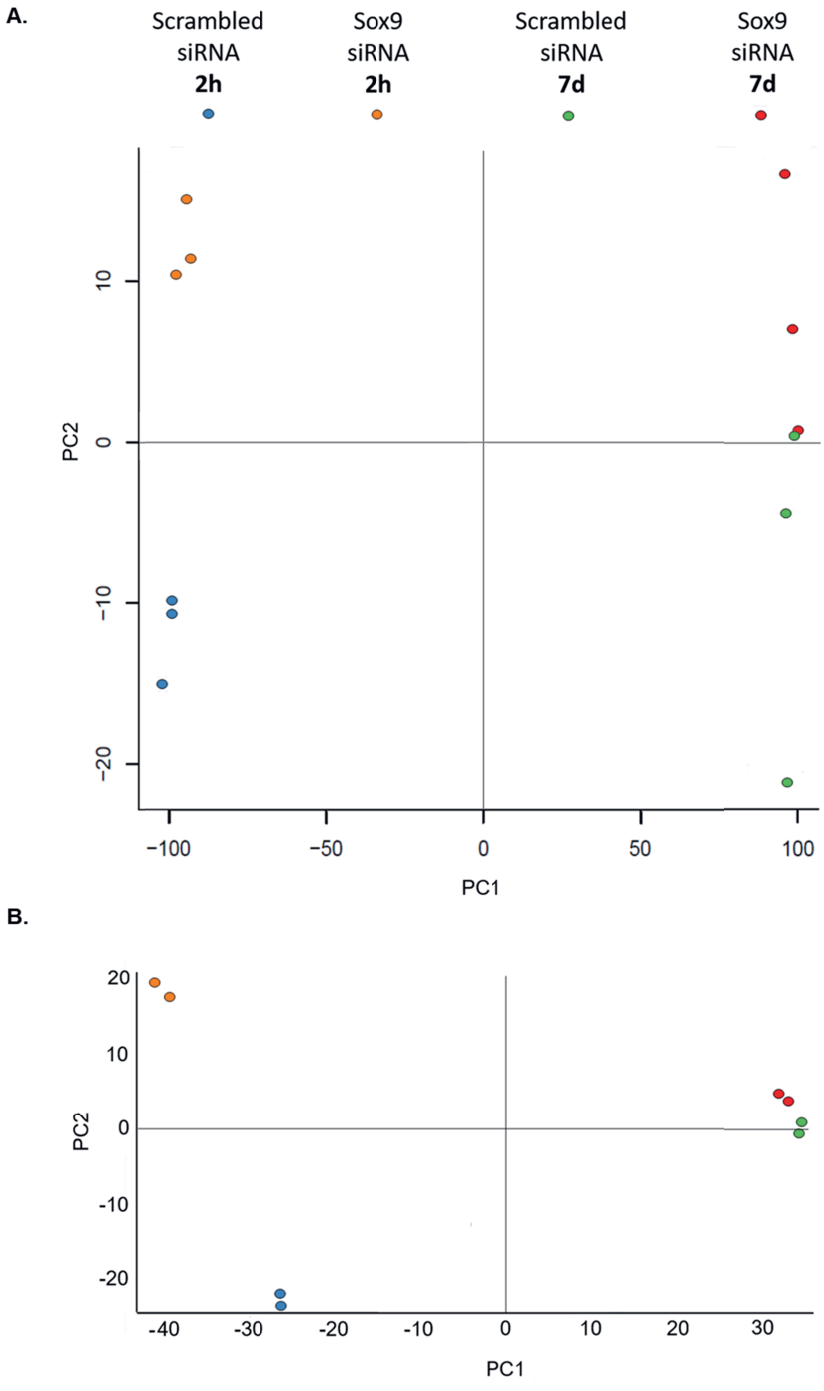

Figure 5.3. PCA analysis. PCA plots of (**A**) RNAseq dataset and (**B**) proteomics dataset. T=2h; Control siRNA (100nM) vs T=2h; Sox9 siRNA (100nM) and T=7d; Control siRNA (100nM) vs T=7d; Sox9 siRNA (100nM).

Noteworthy, the separation between the scrambled siRNA and Sox9 siRNA conditions was particularly evident at 2 hours, while separation between the scrambled siRNA and Sox9 siRNA conditions at 7 days was less obvious. At 2 hours in ATDC5 chondrogenic differentiation, knockdown of Sox9 induced the differential expression of 2422 genes, with 1235 upregulated genes and 1187 downregulated genes (Figure 5.4A, B). At 7 days in differentiation 493 genes were differentially expressed due to knockdown of Sox9. From these differentially expressed genes, 203 genes were upregulated (only 15 overlapped with the 2 hours time point) and 290 genes were downregulated (49 genes overlapped with the 2 hours condition) (Figure 5.4A, B). All genes that were differentially expressed ($FC \geq 2$; $p < 0.05$) at 2 hours and at 7 days in ATDC5 chondrogenic differentiation following Sox9 knockdown, are not shown in this thesis.

Extracted protein samples from control conditions and Sox9 knockdown conditions at 2 hours and 7 days in ATDC5 differentiation were used for LC MS/MS with label free quantification. PCA plotting confirmed that control samples at 2 hours clearly separated from the Sox9 knockdown samples at 2 hours in ATDC5 differentiation. In addition, and in concert with the PCA plot of the RNA sequencing data (Figure 5.3A), the separation between control and Sox9 knockdown conditions appeared to be most obvious at 2 hours in differentiation than at 7 days (Figure 5.3B). At 2 hours in differentiation, knockdown of Sox9 caused the differential expression of 90 proteins, with the expression of 29 proteins being upregulated and 61 proteins downregulated ((Figure 5.4C, D). At 7 days in differentiation, the knockdown of Sox9 induced differential expression of 19 proteins. Of these 19 proteins, the expression of 9 proteins was upregulated and 10 proteins were downregulated (p-value ≤ 0.05; FC cut-off set at 2-fold). There was no overlap between the Sox9-dependent differentially expressed proteins at 2 hours or at 7 days in differentiation (Figure 5.4C, D).

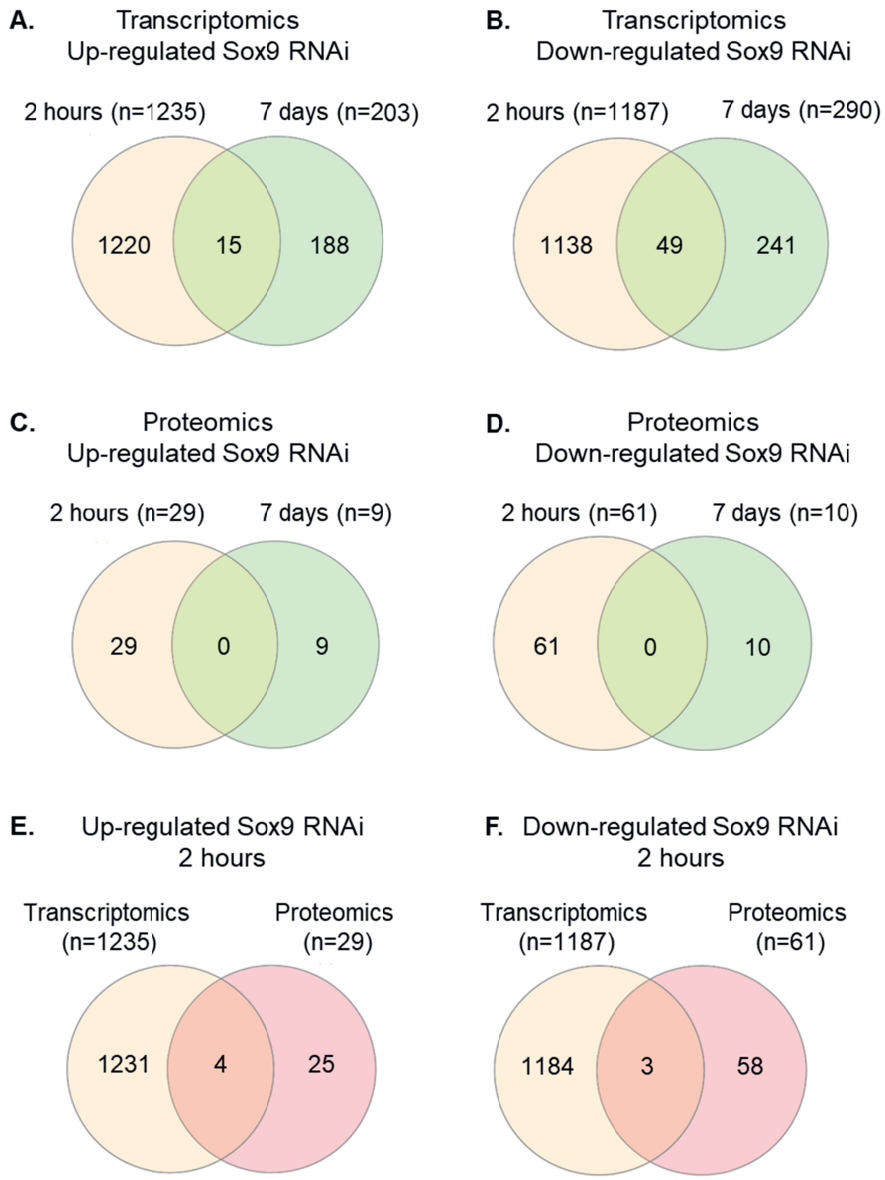

Figure 5.4. Venn diagrams information from the transcriptomic and proteomics analysis. (**A**) Venn diagram showing the numbers of genes whose expression was significantly upregulated upon Sox9 knockdown at 2 hours versus 7 days condition. (**B**) Venn diagram showing the numbers of genes whose expression was significantly downregulated upon Sox9 knockdown at 2 hours versus 7 days condition. (**C**) Venn diagram showing the numbers of proteins whose expression was significantly upregulated upon Sox9 knockdown at 2 hours versus 7 days condition. (**D**) Venn diagram showing the numbers of proteins whose expression was significantly downregulated upon Sox9 knockdown at 2 hours versus 7 days condition. (**E**) Venn diagram showing the upregulated genes versus proteins at 2 hours in differentiation. (**F**) Venn diagram showing the downregulated genes versus proteins at 2 hours in differentiation.

The proteins that were differentially expressed (FC≥2; p<0.05) at 2 hours and at 7 days in ATDC5 chondrogenic differentiation following Sox9 knockdown, are shown in tables 5.3 and 5.4.

Table 5.3. Significantly up and down-regulated proteins found in control siRNA compared to Sox9 RNAi at 2 hours condition in ATDC5 differentiation (protein discoverer, cut-off is > 2-fold and < 0,05).

Protein ID	Gene name	Protein Name	Fold change	p-value
Q99PG2-1	Ogfr	opioid growth factor receptor	0.01	1.00E-17
Q80VJ2	Sra1	Steroid receptor RNA activator 1	0.01	1.00E-17
P23927	Cryab	Alpha-crystallin B chain	0.24	7.41E-05
Q8K274	Fn3krp	Ketosamine-3-kinase	0.25	8.66E-05
P63280	Ube2i	SUMO-conjugating enzyme ubc9	0.28	4.86E-04
Q922W5	Pycr1	Pyrroline-5-carboxylate reductase 1, mitochondrial	0.30	9.65E-04
Q3UPH1	Prrc1	protein PRRC1	0.31	1.10E-03
Q9CZH3	Psmg3	Proteasome assembly chaperone 3	0.34	3.02E-03
Q571I9	Aldh16a1	Aldehyde dehydrogenase family 16 member A1	0.34	3.20E-03
P97346	Nxn	nucleoredoxin	0.35	4.23E-03
P47964	Rpl36	60S ribosomal protein L36	0.35	4.39E-03
P62892	Rpl39	60S ribosomal protein L39	0.37	6.39E-03
Q91VR2	Atp5f1c	ATP synthase subunit gamma, mitochondrial	0.37	6.67E-03
Q9CYG7	Tomm34	Mitochondrial import receptor subunit TOM34	0.38	9.11E-03
P61079	Ube2d3	Ubiquitin-conjugating enzyme E2 D3	0.39	9.56E-03
P21126	Ubl4a	Ubiquitin-like protein 4A	0.39	1.09E-02
Q9D172	Gatd3a	ES1 protein homolog, mitochondrial	0.39	1.11E-02
Q8K4L3-1	Svil	Supervillin	0.40	1.20E-02
Q60932-1	Vdac1	voltage-dependent anion-selective channel protein 1	0.40	1.22E-02
Q920Q6-1	Msi2	RNA-binding protein Musashi homolog 2	0.40	1.23E-02
Q9CQQ7	Atp5pb	ATP synthase F(0) complex subunit B1, mitochondrial	0.40	1.39E-02
Q9R0P3	Esd	S-formylglutathione hydrolase	0.41	1.49E-02
O88696	Clpp	ATP-dependent Clp protease proteolytic subunit, mitochondrial	0.41	1.49E-02
Q60931	Vdac3	Voltage-dependent anion-selective channel protein 3	0.41	1.51E-02
P50518	Atp6v1e1	V-type proton ATPase subunit E 1	0.41	1.58E-02
Q9JLV5	Cul3	Cullin-3	0.42	1.78E-02
P97765	Wbp2	WW domain-binding protein 2	0.42	1.79E-02
P51881	Slc25a5	ADP/ATP translocase 2	0.42	1.85E-02
P53995	Anapc1	anaphase-promoting complex subunit 1	0.42	1.91E-02
Q9CQS2	Nop10	H/ACA ribonucleoprotein complex subunit 3	0.42	2.01E-02
Q9CZ30-1	Ola1	obg-like ATPase 1	0.42	2.02E-02
Q99LS3	Psph	phosphoserine phosphatase	0.42	2.02E-02
Q9DCA5	Brix1	Ribosome biogenesis protein BRX1 homolog	0.43	2.16E-02
Q32MW3	Acot10	Acyl-coenzyme A thioesterase 10, mitochondrial	0.43	2.34E-02
Q9D0I8	Mrto4	mRNA turnover protein 4 homolog	0.43	2.46E-02
P06151	Ldha	L-lactate dehydrogenase A chain	0.43	2.51E-02
Q9DB20	Atp5po	ATP synthase subunit O, mitochondrial	0.44	2.57E-02
Q9CQ65	Mtap	S-methyl-5'-thioadenosine phosphorylase	0.44	2.62E-02
Q8BFR5	Tufm	elongation factor Tu, mitochondrial	0.44	2.65E-02
Q9D7G0	Prps1	ribose-phosphate pyrophosphokinase 1	0.44	2.70E-02
Q80VD1	Fam98b	Protein Fam98b	0.44	2.71E-02
Q8K4J6-1	Mrtfa	MKL/myocardin-like protein 1	0.44	2.82E-02
Q6PER3	Mapre3	Microtubule-associated protein RP/EB family member 3	0.44	2.83E-02
Q9D0T1	Snu13	NHP2-like protein 1	0.44	3.01E-02
Q64105	Spr	Sepiapterin reductase	0.45	3.04E-02
Q99JR5	Tinagl1	Tubulointerstitial nephritis antigen-like	0.45	3.06E-02
P35486	Pdha1	Pyruvate dehydrogenase E1 component subunit alpha, somatic form, mitochondrial	0.45	3.11E-02
Q9WTP7	Ak3	GTP:AMP phosphotransferase AK3, mitochondrial	0.45	3.20E-02

Q61205	Pafah1b3	Platelet-activating factor acetylhydrolase IB subunit gamma	0.45	3.27E-02
Q3B7Z2	Osbp	Oxysterol-binding protein 1	0.45	3.47E-02
P35979	Rpl12	60S ribosomal protein L12	0.46	3.61E-02
P70122	Sbds	Ribosome maturation protein SBDS	0.46	3.62E-02
Q9D819	Ppa1	Inorganic pyrophosphatase	0.46	3.73E-02
Q9JLM8	Dclk1	serine/threonine-protein kinase DCLK1	0.46	3.76E-02
P62962	Pfn1	profilin-1	0.47	4.23E-02
O89023	Tpp1	Tripeptidyl-peptidase 1	0.47	4.27E-02
P48962	Slc25a4	ADP/ATP translocase 1	0.47	4.36E-02
Q9Z1R2	Bag6	Large proline-rich protein BAG6	0.47	4.49E-02
Q5FWK3	Arhgap1	rho GTPase-activating protein 1	0.47	4.64E-02
Q3V3R1	Mthfd1l	Monofunctional C1-tetrahydrofolate synthase, mitochondrial	0.47	4.65E-02
Q9D0T2	Dusp12	Dual specificity protein phosphatase 12	0.47	4.82E-02
Q9WUU7	Ctsz	Cathepsin Z	2.02	2.11E-02
P47739	Aldh3a1	Aldehyde dehydrogenase, dimeric NADP-preferring	2.02	2.08E-02
Q8C1M2	Znf428	Zinc finger protein 428	2.04	1.94E-02
Q9JJI8	Rpl38	60s ribosomal protein l38	2.06	1.78E-02
P18608	Hmgn1	Non-histone chromosomal protein HMG-14	2.12	1.42E-02
Q922U1	Prpf3	U4/U6 small nuclear ribonucleoprotein Prp3	2.13	1.38E-02
P62862	Fau	40S ribosomal protein S30	2.14	1.28E-02
Q6WKZ8-1	Ubr2	E3 ubiquitin-protein ligase UBR2	2.15	1.27E-02
O70326	Grem1	Gremlin-1	2.17	1.17E-02
Q9D9K3	Aven	Cell death regulator Aven	2.19	1.10E-02
P43274	H1-4	Histone H1.4	2.19	1.07E-02
P15864	H1-2	Histone H1.2	2.24	8.91E-03
Q8R180	Ero1a	ERO1-like protein alpha	2.24	8.79E-03
Q4KML4	Abracl	Costars family protein ABRACL	2.26	8.33E-03
Q9CU62	Smc1a	structural maintenance of chromosomes protein 1a	2.27	7.89E-03
Q8R0P4	Aamdc	Mth938 domain-containing protein	2.28	7.75E-03
P43275	H1-1	Histone H1.1	2.28	7.60E-03
Q9CPY7-1	Lap3	cytosol aminopeptidase	2.33	6.20E-03
Q6NSR8	Npepl1	Probable aminopeptidase NPEPL1	2.34	6.13E-03
Q8C8T8	Tsr2	pre-rRNA-processing protein TSR2 homolog	2.36	5.56E-03
P43276	H1-5	Histone H1.5	2.37	5.45E-03
P63089	Ptn	Pleiotrophin	2.38	5.28E-03
P09602	Hmgn2	Non-histone chromosomal protein HMG-17	2.57	2.51E-03
Q99JF8	Psip1	PC4 and SFRS1-interacting protein	2.89	7.55E-04
P62204	Calm	Calmodulin	2.95	5.95E-04
Q9JHW4	Eefsec	selenocysteine-specific elongation factor	3.17	2.74E-04
Q3SXD3	Hddc2	HD domain-containing protein 2	5.86	4.75E-08
Q9CY58-2	Serbp1	Isoform 2 of Plasminogen activator inhibitor 1 RNA-binding protein	6.88	2.96E-09
Q61164	Ctcf	Transcriptional repressor CTCF	100.00	1.00E-17

Table 5.4. Significantly up and down-regulated proteins found in control siRNA compared to Sox9 RNAi at 7 days condition in ATDC5 differentiation (protein discoverer, cut-off is > 2-fold and < 0,05).

Protein ID	Gene name	Protein Name	Fold change	p-value
Q9Z1E4	Gys1	glycogen [starch] synthase, muscle	0.01	1.00E-17
P21460	Cst3	Cystatin-C	0.31	7.10E-07
O54782	Man2b2	Epididymis-specific alpha-mannosidase	0.32	2.27E-05
P51660	Hsd17b4	peroxisomal multifunctional enzyme type 2	0.37	4.37E-13
Q99KV1	Dnajb11	DnaJ homolog subfamily B member 11	0.39	1.36E-09
Q9D125	Mrps25	28S ribosomal protein S25, mitochondrial	0.41	7.72E-08
Q60648	Gm2a	Ganglioside GM2 activator	0.42	1.08E-07
Q9CQD1	Rab5a	Ras-related protein Rab-5A	0.47	5.65E-03
Q99M71	Epdr1	Mammalian ependymin-related protein 1	0.47	1.64E-08
P24270	Cat	catalase	0.48	9.68E-09
Q3TIV5-1	Zc3h15	Zinc finger CCCH domain-containing protein 15	2.11	3.46E-04
P35282	Rab21	Ras-related protein Rab-21	2.19	3.38E-03
Q9DCX2	Atp5pd	ATP synthase subunit d, mitochondrial	2.26	1.17E-05
Q60996-1	Ppp2r5c	Serine/threonine-protein phosphatase 2A 56 kDa regulatory subunit gamma isoform	2.29	7.93E-06
P45952	Acadm	medium-chain specific acyl-CoA dehydrogenase, mitochondrial	2.30	3.83E-06
Q9CQX8	Mrps36	28S ribosomal protein S36, mitochondrial	2.37	1.16E-04
Q99JR5	Tinagl1	Tubulointerstitial nephritis antigen-like	2.75	1.37E-04
Q8BFS6-1	Cpped1	Serine/threonine-protein phosphatase CPPED1	3.06	2.14E-13
P84228	Hist1h3b	histone H3.2	100.00	1.00E-17

These data indicate that at 2 hours in chondrogenic differentiation the knockdown of Sox9 induces different changes in the ATDC5 transcriptome and proteome when compared to knockdown of Sox9 at 7 days in differentiation. In addition, the consequences of Sox9 siRNA treatment appears to be stronger at 2 hours than at 7 days of differentiation, as indicated by larger separation in the PCA plots and larger number of differentially expressed genes and proteins. The role of the immediate early Sox9 expression was further investigated by comparing the Sox9-dependent differentially expressed mRNAs and proteins at 2 hours in differentiation, since differences in mRNA expression are expected to reflect on differences in protein expression. Figure 5.4E and F shows 4 overlapping mRNAs and proteins upregulated in the early Sox9 knockdown condition (Rps30/Fau, Avan, Eefsec, Rpl38) and 3 overlapping mRNAs and proteins downregulated in the early Sox9 knockdown condition (Ube2d3, Dclk1, Svil).

Immediate early Sox9 expression is involved in ribosomal protein expression

To determine which prominent pathways link to the Sox9-dependent differential transcriptome and proteome at 2 hours in differentiation, we performed pathway analyses. Both WikiPathways and KEGG Pathway analysis revealed that "Cytoplasmic Ribosomal Proteins" and "Ribosome" pathways were in the top three of identified enriched pathways (Table 5.5).

Table 5.5. Early Sox9 expression is involved in ribosomal pathways. Top 3 identified enriched pathways from WikiPathways 2019 and KEGG2019 pathway analysis in control RNAi compared to Sox9 RNAi at 2 hours condition in ATDC5 differentiation for transcriptome and proteome data sets.

WikiPathways database (Mouse) - Transcriptome (2h condition)

Pathway ID	Pathway description	P-value (p)	Adjusted p-value (q)	Combined score
WP163	Cytoplasmic Ribosomal Proteins	3.67E-11	6.46E-09	77.64
WP1248	Oxidative phosphorylation	3.86E-07	2.26E-05	45.24
WP295	Electron Transport Chain	2.74E-07	2.41E-05	38.77

KEGG database (Mouse) - Transcriptome (2h condition)

Name	P-value (p)	Adjusted p-value (q)	Combined score
Ribosome	1.12E-10	3.39E-08	57.88
Huntington disease	1.25E-08	1.90E-06	40.69
Thermogenesis	3.69E-08	3.72E-06	35.49

WikiPathways database (Mouse) - Proteome (2h condition)

Pathway ID	Pathway description	P-value (p)	Adjusted p-value (q)	Combined score
WP163	Cytoplasmic Ribosomal Proteins	5.96E-05	1.05E-02	117.49
WP175	Acetylcholine Synthesis	3.11E-02	7.82E-01	110.19
WP298	G13 Signaling Pathway	1.33E-02	5.86E-01	49.21

KEGG database (Mouse) - Proteome (2h condition)

Name	P-value (p)	Adjusted p-value (q)	Combined score
Glycolysis / Gluconeogenesis	3.43E-03	5.20E-01	56.47
Pyruvate metabolism	1.27E-02	3.49E-01	51.09
Ribosome	1.03E-03	3.11E-01	44.98

Such strong overrepresentation of the "Cytoplasmic Ribosomal Proteins" and "Ribosome" pathways was not obvious in the Sox9-dependent differential transcriptome and proteome at day 7 in differentiation (Table 5.6).

Table 5.6. Top 3 identified enriched pathways from WikiPathways 2019 and KEGG2019 pathway analysis in control siRNA compared to Sox9 RNAi at 7 days condition in ATDC5 differentiation for transcriptome and proteome data sets.

WikiPathways database (Mouse) - Transcriptome (7d condition)

Pathway ID	Pathway description	P-value (p)	Adjusted p-value (q)	Combined score
WP1253	Type II interferon signaling (IFNG)	3.13E-10	5.51E-08	287.23
WP163	Cytoplasmic Ribosomal Proteins	8.22E-10	7.23E-08	147.60
WP222	Cytokines and Inflammatory Response	4.08E-03	1.44E-01	33.06

KEGG database (Mouse) - Transcriptome (7d condition)

Name	P-value (p)	Adjusted p-value (q)	Combined score
Epstein-Barr virus infection	1.01E-10	1.52E-08	106.03
Herpes simplex virus 1 infection	7.53E-13	2.28E-10	104.61
Measles	1.73E-08	1.75E-06	90.63

WikiPathways database (Mouse) - Proteome (7d condition)

Pathway ID	Pathway description	P-value (p)	Adjusted p-value (q)	Combined score
WP2318	Fatty acid oxidation	9.46E-03	8.33E-01	490.58
WP317	Glycogen Metabolism	4.71E-04	8.29E-02	474.34
WP55	Steroid Biosynthesis	1.32E-02	7.76E-01	325.25

KEGG database (Mouse) - Proteome (7d condition)

Name	P-value (p)	Adjusted p-value (q)	Combined score
Primary bile acid biosynthesis	1.51E-02	1	275.87
Amyotrophic lateral sclerosis (ALS)	1.10E-03	3.34E-01	275.73
Other glycan degradation	1.70E-02	1	238.38

Further analysis of the 2 hours Sox9-dependent transcriptome datasets revealed the differential expression of 29 ribosomal proteins from the large (60S) ribosomal subunit (Rpls) and 10 ribosomal proteins from the small (40S) ribosomal subunit (Rpss) in the Sox9 knockdown condition at 2 hours in differentiation (Figure 5.5A). In addition, the 2 hours proteomics datasets demonstrated the differential expression of 5 ribosomal Rpl and Rps proteins (Figure 5.5A and table 5.2). Notably, the 4 overlapping mRNAs and proteins (Rps30/Fau, Avan, Eefsec, Rpl38) that were found to be upregulated in the Sox9 knockdown condition at 2 hours in ATDC5 chondrogenic differentiation (Figure 5.4E) are all linked to protein translation and represent either ribosomal protein subunits or factors with a known function in ribosome biogenesis. Additional factors involved in ribosome biogenesis, but only differentially expressed in either the 2 hours transcriptomics or proteomics datasets were SBDS, Nop10 and Brix1 (Data not shown). Since ribosomes consist of protein and ribosomal RNA (rRNA), we next investigated by RT-qPCR whether rRNA levels are also affected by the Sox9 knockdown at 2 hours in differentiation in ATDC5. Expression of 18S rRNA, 28S rRNA and 5.8S rRNA was not significantly different between the conditions (Figure 5.5B). Together, these data indicate that the immediate early Sox9 expression during ATDC5 chondrogenic differentiation is involved in ribosomal protein expression and ribosome biogenesis.

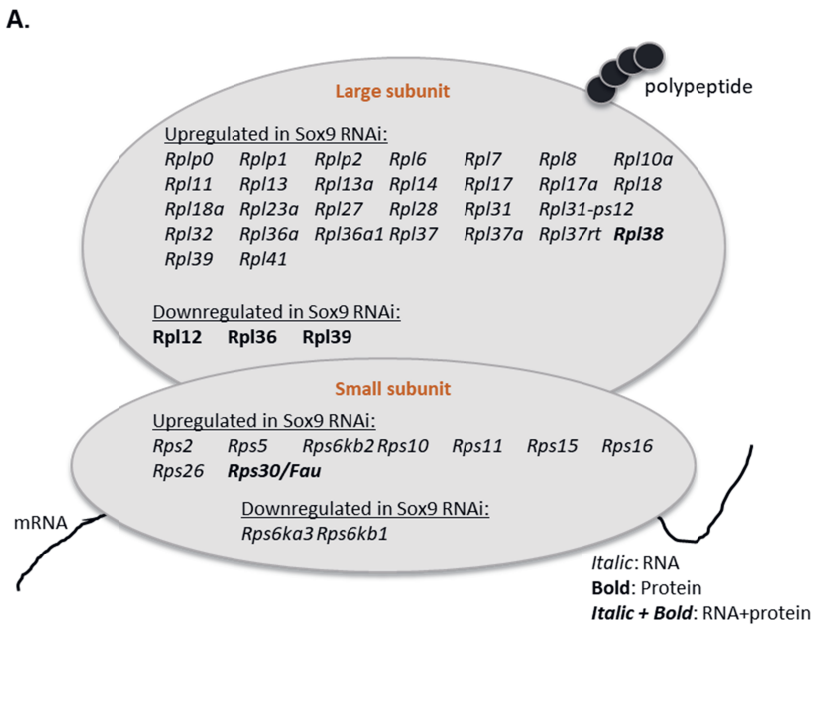

Figure 5.5. Early Sox9 regulates ribosomal protein expression. (**A**) Schematic representation of significantly differentially expressed ribosomal proteins from transcriptome and proteome datasets. (**B**) 18S rRNA, 28S rRNA and 5.8S rRNA expression at 2 hours in ATDC5 differentiation in Control and Sox9 RNAi conditions as measured by RT-qPCR. Results were normalized to β-Actin RNA expression and presented relative to t=0. Bars represent mean±SEM. ns= not significant, *=p<0.05, **=p<0.01, p=<0.0001.

Early Sox9 expression regulates protein translation capacity and ribosome translation modus

Since we found differential expression of ribosomal protein subunits and ribosome biogenesis factors, combined with unaltered rRNA expression levels, we hypothesized that ribosomes of early Sox9 knockdown ATDC5 cells are functionally distinct. To address this hypothesis, we measured total translational capacity, performed polysome fractionation and evaluated ribosome translation modus in Sox9 knockdown and control ATDC5 cells. Following the knockdown of immediate early Sox9 expression a reduction of the total protein translational capacity was observed at 2 hours (Figure 5.6A).

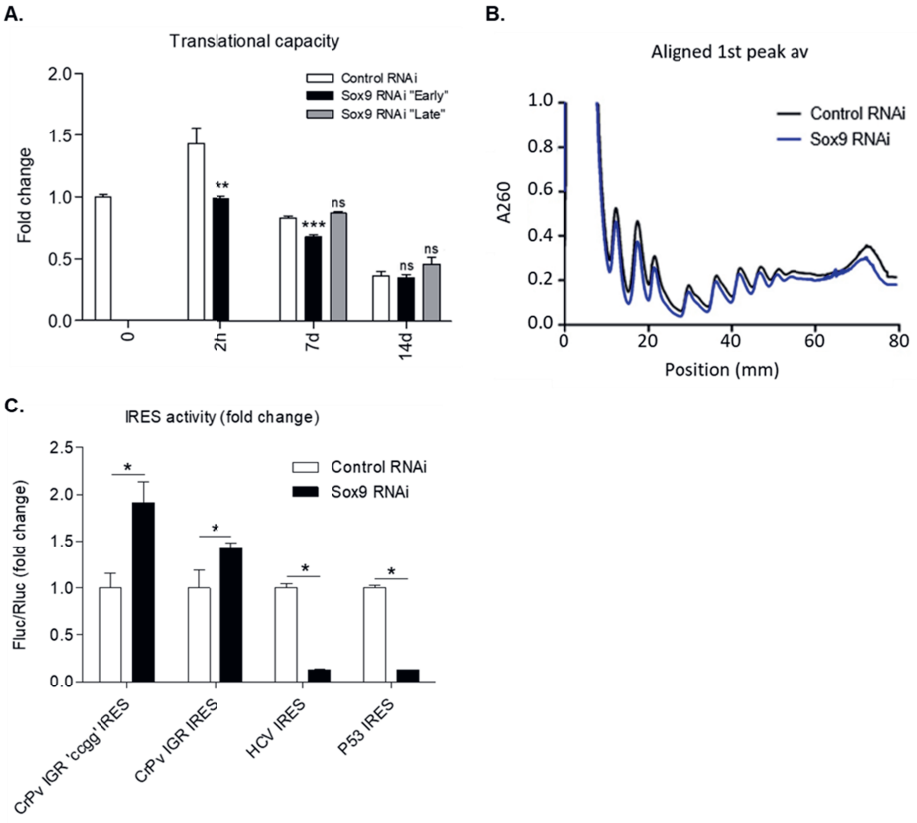

Figure 5.6. Knockdown of early Sox9 expression leads to a reduced translational capacity, lower amount of ribosomes and alters ribosome modus. (**A**) Total protein translation measurements based on puromycin incorporation was normalized to total DNA content per well (Mean±SEM, n=6/group) at indicated time points. (**B**) Polysome fractionation of control and Sox9 knock-down cells (Mean only, n=3/group) after 2 hours of differentiation. (**C**) Ribosome modus was assessed for the CrPv IGR CCGG mutant IRES, the intact CrPv IGR IRES, the HCV IRES and the P53 IRES after 24 hours of differentiation. Bars represent mean±SEM. ns= not significant, *=p<0.05, **=p<0.01, p=<0.0001.

The abrogation of early Sox9 expression also caused a reduction of total protein translational capacity at day 7 in differentiation (while Sox9 levels normalize at 7 days following the early knockdown (Figure 5.2B)). This impact on translation capacity was lost at day 14 in differentiation (Figure 5.6A). In contrast, late knockdown of Sox9 expression did not affect ATDC5 translational capacity at 7 days in differentiation. This is consistent with transcriptome and proteome data. To assess if Sox9 knock-down had a specific effect on active monosomal or polysomal ribosomes, we performed sucrose gradient density separation of ribosomal subunits (40S and 60S), 80S monosomes and polysomes. With equal loading of cytoplasmic extracts, knockdown of the immediate early Sox9 expression resulted in an overall lower level of ribosomal subunits, monosomes and polysomes at 2 hours in ATDC5 chondrogenic differentiation (Figure 5.6B). In addition to total ribosome translation capacity, the modus of translation is also subject to regulation. Thus, we evaluated the activity of IRES (internal ribosome entry site)- over cap-mediated protein translational activity using well-known IRES bicistronic reporter constructs (CrPv IGR, HCV and P53) [242-244]. We found a 1.5-fold induction of the ITAF (IRES trans-acting factors) independent CrPv IGR IRES and 5-fold down regulation of both the HCV and P53 IRES in Sox9 knockdown ATDC5 cells compared to controls (Figure 5.6C and figure 5.7).

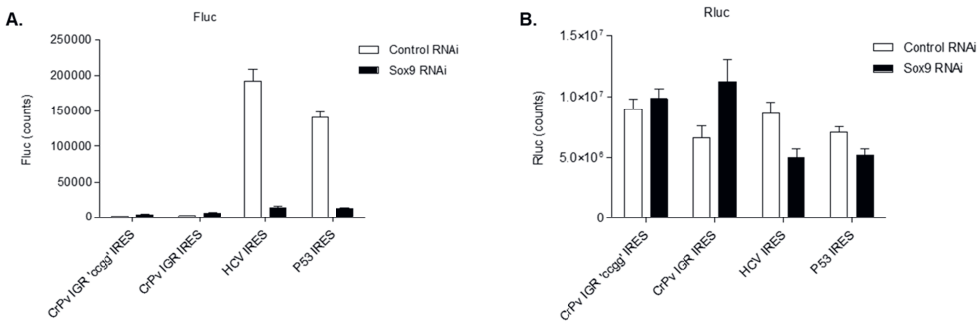

Figure 5.7. Raw data of individual cistrons in the bicistronic reporter assay. Ribosome modus was assessed at 24 hours of differentiation and two days after transfection. (A) Raw firefly luciferase counts following reporter plasmid transfections. (**B**) Raw renilla luciferase counts following reporter plasmid transfections. Mean±SEM, n=3/group.

Knockdown of early Sox9 expression during ATDC5 chondrogenic differentiation reduced protein translational activity over a seven-day time period, which was reflected by a general reduction of A_{260} signal in a polysome fractionation experiment at 2 hours in differentiation. In addition, this had a differential effect on ribosome modus during the first day of differentiation.

Ribosomopathies are severe genetic diseases caused by mutations in genes involved in ribosome biogenesis and function and are, amongst others, associated with developmentally-related skeletal malformations, caused by impairment of chondrogenic development of the growth plates.[245] This indicates that chondrogenic differentiation is

particularly susceptible for disturbances in ribosome protein translation activity. Indeed, during chondrogenesis, a large amount of proteinaceous cartilage ECM is produced by the developing growth plate and disturbances in ribosome activity are likely to impair ECM synthesis, with consequences for the development of skeletal elements. It should however be noted that the link between Sox9 and chondrocyte translation activity in the present work was particularly present during early differentiation rather than late differentiation. This is highlighted by deregulated expression of ribosomal subunits following Sox9 knockdown in early ATDC5 chondrogenic differentiation (Figure 5.5 and table 5.4). In addition, the knockdown of Sox9 specifically impacted total protein translation throughout differentiation when knocked-down early, while not having an effect on protein translation when knocked-down during late chondrogenic differentiation (Figure 5.6). The link between early Sox9 and chondrocyte protein translation suggests that protein translation is likely to be paced through Sox9 during early chondrogenic differentiation However, it remains to be determined how early Sox9 is specifically able to influence chondrocyte translational capacity. Our present data suggest that expression of ribosomal protein subunits, ribosome biogenesis factors and ancillary ribosomal factors (such as IRES trans-acting factors (ITAFs)) depends on Sox9 during early chondrogenic differentiation, with downstream consequences for translation in the later differentiation program. Since we found these ribosomal genes and proteins differentially expressed after Sox9 knockdown, we studied supplemental data of previously published Sox9 ChIP-seq and Sox9$^{-/-}$ mouse studies.[238, 241] In supplementary data of a Sox9 ChIP-seq study we found 24 Rps and Rpl genes that were enriched in Sox9 occupancy and 14 with Sox6 occupancy of which 10 overlapped.[241] Notably, this included Rpl38, which we found to be differentially expressed at the mRNA and protein level in our Sox9 knockdown condition.

Aside from ribosome core components, we found differential expression of several factors regulating the mode of protein translation. The rate-limiting step of cap-mediated translation is eukaryotic initiation factor 4. Interestingly, EIF4BP2 was downregulated at the protein level at 2 hours of differentiation in Sox9 knockdown cells. EIF4 binding proteins were shown to regulate cell proliferation, but not cell size.[246] Unexpectedly, we found strong differences in IRES activity upon early Sox9 knockdown after 24 hours of differentiation. Of note, the CrPv IGR IRES (Type IV) does not require ITAFs and is able to recruit the ribosome directly.[247] The activity of this IRES was increased and might be regulated by specific Rps/Rpls that transiently interact with the core ribosome components. The HCV (Type III) and P53 IRES do require additional ITAF co-factors.[248] Based on the increased expression of the ITAF Rpl38, it is tempting to speculate that other ITAFs that facilitate HCV/P53 IRES translation are down regulated and may contribute to alternative use of ribosome translation modus. Rpl10a, Rpl11, Rpl38 and Pdcd4 were shown to regulate IRES-mediated translation.[248] Rpl10a is known to activate the *IGF2*, *APP*, *Chmp2A* and *Bcl-2* IRES. Gain and loss of function studies in the fruit fly showed that *Rpl10a* regulates insulin signaling.[249] Moreover, *Rpl10a* mRNA was found to be

preferentially translated by a subpool of ribosomes in embryonic stem cells that required ribosome-associated *Rpl10a* protein.[250] Insulin and IGF1 signaling are crucial for ATDC5 differentiation[228] Rpl11 induced the *BAG1*, *CSDE1* and *LamB1* IRESes, while *Rpl38* activated a Hox gene IRES. Up regulation of *Rpl11* led to stabilization of P53 and reduced proliferation of breast cancer cell-lines.[251] In contrast, we found a reduction in *P53* IRES activity. Of note, P53 and ribosome biogenesis were recently coupled through SBDS.[252] In our dataset, SBDS was down regulated at the protein level at 2 hours in differentiation in siSox9 treated cells, which matches with the observed reduction in ribosomes and/or ribosome activity. Pdcd4 activated or inhibited the P53, INR, IGF1R, BcL-XL and XIAP IRESes.[248] The IGF1R IRES might again be relevant for the ATDC5 differentiation model. Finally, Rpl38 was the only ITAF that was found to be up regulated at both the mRNA and protein level. It was found to control HOX gene translation during murine embryonic development [253] and knockout led to ectopic mineralization in certain soft tissues.[254]

Together we identified multiple connections between immediate early Sox9 expression in ATDC5 chondrogenic differentiation and downstream consequences for expression of ribosomal protein subunits, ribosome biogenesis factors and ITAFs. This connection between Sox9 expression and protein translation appears to be centered in early chondrogenic differentiation with consequences for protein translation in later stages. This suggests a role for early Sox9 in the priming of the progenitor cell in the chondrogenic differentiation program for cartilaginous ECM production later in differentiation. This provides a new level of understanding how Sox9 controls the fate of chondrogenic differentiation at the level of protein synthesis. In this respect it is tempting to speculate on the classification of campomelic dysplasia [255], as links between Sox9 and genes involved in ribosomopathies [245, 256] were identified in the present work (SBDS, Rpl11, Rps26).

5.5. Chapter conclusions

In conclusion, we here collected essential new data on the regulation by Sox9 during early chondrogenic differentiation, uncovering an unanticipated role of Sox9 in ribosome biogenesis and protein translational capacity.

Acknowledgements
This work was financially supported by the Dutch Arthritis Association (grant LLP14) and by the Dutch Province of Limburg through the "LINK" program and by the MUMC+ institutional grant for clinical collaborative research.

CHAPTER 6

Valorization

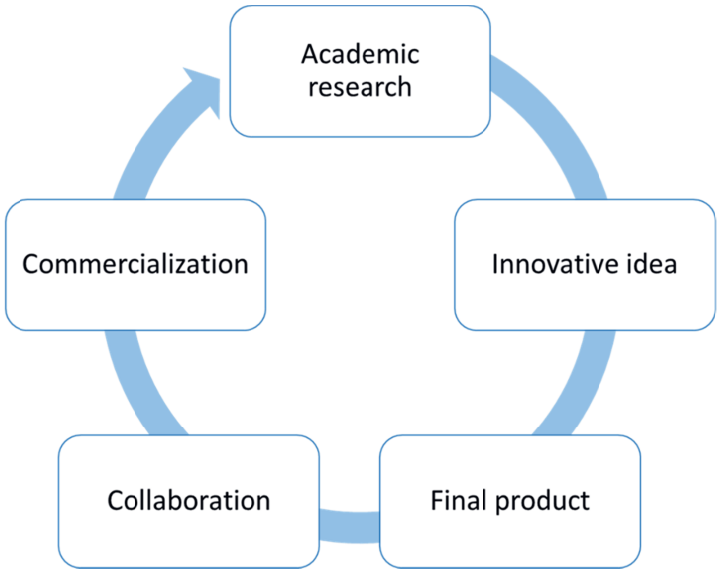

6. Valorization

OA is becoming more prevalent as the world population ages. In 2032, at least an additional 26 thousand of people per one million population older than 45 years are estimated to have consulted for OA in a peripheral joint compared to 2012.[257] This increase in OA leads to challenges for health care and public health systems. We need to address this problem with new, personalized treatments.

One of the main goals of this thesis is to employ MS-based approaches on human knee cartilage to help for the classification of different OA phenotypes.

A multimodal approach can improve the classification of phenotypes

The importance and need to consider different OA phenotypes have been extensively discussed in this thesis and described in the literature. Deciphering the biomolecular profiles of each OA phenotype will improve the classification models as well as the development, design, and efficacy of OA-phenotype-specific drugs. Combined with physician-advised and preventive lifestyle choices (healthy lifestyle, low-impact exercise, healthy diet…), the research and approach discussed in this thesis will ultimately improve patient care and have an effect on general health outcomes.

In this thesis, the combination of MALDI-MSI and bottom-up proteomic approaches is described as a powerful methodology to study the knee cartilage tissue and improve the classification of two different OA phenotypes. The protocol presented herein enabled us to discover inflammatory proteins and lipids associated to either OA or T2DM disease. Although our results need further investigation through functional studies, this fundamental knowledge is the first step towards new pharmaceutical interventions. Importantly, the same protocol we used could also be considered to classify i) other OA phenotypes described in the literature or ii) OA patients based on other variables such as gender, age, post-traumatic vs non-post-traumatic, or BMI. For this last purpose, the access to patient´s clinical history remains crucial.

Additionally, the cross-tissue data collected at different areas from the joint of the same patients could also improve the classification of OA phenotypes. Indeed, the approach presented could be reproduced in other tissues involved in the OA disease, such as Hoffa's fat pad, bone or synovium membrane. As a consequence, the complementary biological information obtained on such tissues could significantly improve or validate the data from the study described in **chapter 4**.

The experimental design as a new methodology to optimize a MALDI-MSI approach

The optimization of methodologies is also an essential factor to be considered in all scientific fields. In this thesis we described a new strategy to optimize the MALDI-MSI protocols for the detection of endogenous metabolites in cartilage tissues. Our experimental design revealed the most important parameters for method optimization and consequently improved the quality of MSI data. This optimized workflow could then be further used to either investigate the metabolic changes of different OA-phenotypes or on cartilage tissues displaying another pathology such as the rheumatoid arthritis disease.

Our experimental design methodology could also be considered in any scientific field where optimized protocols are needed. As an example, the use of the experimental design could be useful to create standard operating protocols (SOP) within research laboratories.

The heat stabilization process improves the detection of fast-degrading compounds and other biomolecules

Tissue degradation starts when a tissue is removed from its native environment. Alteration at the molecular level can occur within seconds. In a biological project involving a large cohort of patients, tissue degradation could lead to inter-sample variation, incorrect data interpretation, and misleading conclusions. In this thesis, the heat stabilization process was performed immediately before the snap-freezing process of the cartilage tissues. This heat stabilization process may prevent artificial biological changes and ensure accurate downstream MALDI-MSI results. The implementation of this process into pharmaceutical companies' workflows could help companies to assess the abundance of analytes in their products.

The suggested stratification of OA patients and the MALDI-MSI developments presented in the thesis can be predominantly applied in biomedical studies and health care fields. The identified lipidomic and proteomic markers for improved stratification of OA phenotypes can be used for personalized therapies but could also be investigated as potential biomarkers for diagnosis of OA disease. Moreover, our studies revealed the possibility to rapidly process and prevent biological changes (e.g. degradation) of clinical knee cartilage samples. Our heat stabilization process should also be considered in every clinical study, where MSI is needed as a biomarker discovery tool.

The project also initiated a strong collaboration between scientists and clinicians working on OA disease, which is key for translational research.

CHAPTER 7

General discussion

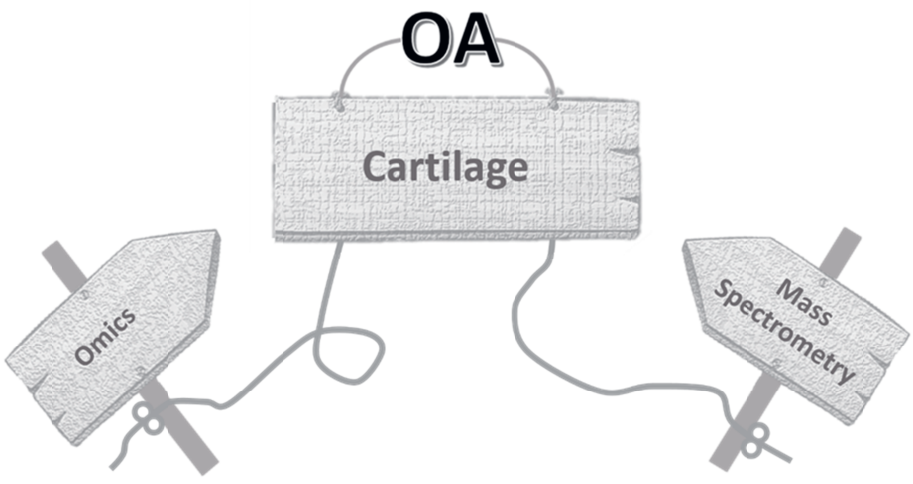

7. General discussion

Mass spectrometry imaging (MSI) has generated enormous momentum over the past decade. MSI covers a wide range of biomedical applications such as biomarker discovery and tissue classification. MALDI-MSI remains the most applied MSI technique in the rheumatology field.

In this thesis, we developed and optimized MALDI-MSI methods for studying cartilage and deployed several -omics approaches to decipher OA disease at a molecular level.

7.1. Sample preparation

Sample preparation is one of the most critical steps in analytical chemistry. **Chapter 3** demonstrates that the detection of endogenous metabolites in human cartilage by MALDI-MSI would not be possible without an optimized workflow, from sampling to data analysis. In particular, the combination of the Denator system and the design-of-experiments approach has enabled better detection of metabolites in cartilage. When properly applied, the Denator system immediately and permanently prevents biological changes, and therefore allows samples to reflect the *in vivo* state as closely as possible. The Denator system was also used in **chapter 4**, as we demonstrated its efficiency to preserve endogenous lipid species. The design-of-experiments concept has a great potential to reduce the number of experiments and to provide the most significant parameters for high quality results. The workflow presented here could be applied to any other biomolecular class and could be considered before dealing with precious samples.

Additional sample preparation steps were also developed for dealing with difficult tissue types, such as articular cartilage. Articular cartilage is difficult to work with for several reasons. First, the amount of cartilage tissue obtained after the knee surgery differs from patient to patient. This is mainly due to the different OA grades, which reflects the severity of the disease. Moreover, articular cartilage tissue is negatively charged and thus tends to detach from the slide or sample holder when using high pressure mass spectrometers. Different solutions have been implemented to overcome these weak points. The use of 8mm punches was a method introduced to standardize the sample collection and ensure the collection of the different cartilage layers. Double-sided copper tape was applied to slides before the thaw mounting of cartilage tissues. The use of double-sided copper tape was a simple way to avoid adhesion trouble. However, the use of double-sided copper tape compromised the optical visualization of any staining protocol performed after the MALDI-MSI. A

more optimal solution that allows for optical visualization and staining and also prevents cartilage tissue sample adhesion problems needs to be developed.

7.2. The need of a multimodal approach

Bottom-up proteomics is a mass spectrometry-based methodology that was used in the research conducted in **chapters 4 and 5**. The main goal of bottom-up proteomics is to identify and quantify proteins across different samples. The workflow for bottom-up proteomics is well established in the proteomic community, but sample preparation can differ slightly between applications. In this thesis, the sample preparation of articular cartilage (**chapter 4**) is different from the one used for ATDC5 cells (**chapter 5**). More importantly, both sample preparation techniques highlight the necessity to combine the bottom-up, label free proteomics approach with other techniques to have a more complete understanding of the biological processes. The workflow used in **chapter 4** combined the bottom-up approach with MALDI-MSI for lipid analysis. The workflow results in a specific panel of distinctive proteins and lipids between OA/T2DM$^-$ and OA/T2DM+ phenotypes that need to be validated in a larger cohort. The work presented in **chapter 5** combined label free proteomics with transcriptomics and revealed that the ribosomal protein synthesis system is regulated by Sox9 gene expression during early chondrogenic differentiation of ATDC5 cells.

7.3. Molecular phenotypes of OA

OA is a heterogeneous disease with multiple molecular phenotypes. The classification of these phenotypes could drastically transform clinical trials and improve their efficiency. The classification also supposes the need to access patient clinical history as much as possible. In **chapter 4**, we showed the possibility to classify OA/T2DM$^-$ from OA/T2DM+ patients based on relevant metabolic pathways such as lipid regulation. Interestingly, the other pathways described in **chapter 4**, such as cellular oxidative stress or extracellular matrix (ECM) pathways, could also be considered for future studies. Another future direction is to compare more OA-related disease classification parameters than just OA/T2DM$^-$ to OA/T2DM+. For instance, BMI based classification, age, or gender might result in the discovery of other molecules of interest. Moreover, OA subclassification in relation to the other diseases linked to the MetS phenotype, previously described in the introduction, could reveal additional and more specific molecular markers. As an example, classification of OA/dyslipidemia$^-$ and OA/dyslipidemia+ phenotypes could be considered. As an additional note, in **chapter 4**, ten patients were used per

group, but validation of potential prognostic and diagnostic markers should be evaluated in a larger cohort.

7.4. Perspective of MSI in the OA field

The results in **chapter 2** demonstrated the potential of the imaging technologies and their applications in the OA field. We showed how MSI, LESA and LMD could be applied to spatially resolve the proteins on cartilage tissue but more importantly, all the approaches described could also be used to investigate other biomolecules (lipids, metabolites or glycans, for instance). Moreover, **chapter 2** showed that enzymes other than trypsin, the gold standard for peptide analysis, can be used in some applications in the OA field. This is the case for the collagenase family, which could be used to improve the protein coverage of MS-based experiments. The combination of different enzymes could also be considered to improve protein identification in cartilage tissue.

SUMMARY (Samenvatting)

Summary

In **chapter 2**, we reviewed different proteomic approaches and their applications in the OA field. The chapter also highlighted the recent imaging technologies, such as MSI, LESA, and LMD, which are not yet fully applied by the OA community. The advantages, disadvantages, and recent applications of MSI, LESA, and LMD are described in **chapter 2**. Mass cytometry and multiplexed ion beam imaging are also presented as spatially-resolved approaches to consider for targeted analyses.

An optimized MALDI-MSI approach for the detection of endogenous metabolites in human OA cartilage is described in **chapter 3**. In particular, we demonstrated the importance of heat stabilization to preserve the endogenous metabolites and lipids within the cartilage samples. We showed the potential of a design-of-experiments approach to optimize the spraying step. This design-of-experiments approach also revealed how small changes can drastically improve or reduce the data quality. Finally, the validation of the optimized MALDI-MSI approach was performed using a high mass resolution instrument and showed higher metabolic activity in the superficial layer of the cartilage.

In **chapter 4**, the MALDI-MSI technology for lipid analysis was combined with a label-free proteomics approach to reveal different molecular cartilage profiles between OA/T2DM^{-} and OA/T2DM^{+} phenotypes. Our work showcased specific lipids associated to each phenotype as well as differences in phospholipid content between superficial and deep layers of the cartilage. We also highlighted the need to examine apolipoprotein A-1 and phospholipase A2 in a larger cohort study as well as for further functional analysis.

In **chapter 5**, we combined label-free proteomics and transcriptomics to uncover a potential new role of Sox9 gene, known to be involved in the chondrogenesis process. We proposed new functions of Sox9 during early chondrogenic differentiation and showed its implication in ribosomal translation as well as in the protein translation capacity. Our data also suggest a role for early Sox9 expression in the priming of the progenitor cells in the chondrogenic differentiation program for cartilaginous ECM.

The valorization of this thesis is presented in **chapter 6**. The need to consider a multimodal approach to improve the classification of phenotypes is highlighted. Then, the design of experiments is described as a new strategy to optimize a MALDI-

MSI approach. Finally, we showcased the heat stabilization process for the prevention of biological changes, which ensures accurate and reproducible results.

Samenvatting

In **hoofdstuk 2** bespreken we verschillende proteomische benaderingen en hun toepassingen in het OA-veld. Ook belicht dit hoofdstuk de recente beeldvormende technologieën, zoals MSI, LESA en LMD, die nog relatief onbekend zijn binnen de OA-gemeenschap. Daarnaast worden de voordelen, nadelen en recente toepassingen van MSI, LESA en LMD beschreven. Ten slotte worden massacytometrie en gemultiplexte ionenbundelbeeldvorming gepresenteerd als ruimtelijk opgeloste benaderingen voor gerichte analyses.

Een geoptimaliseerde MALDI-MSI methode voor de detectie van endogene metabolieten van artrose in humaan kraakbeen wordt beschreven in **hoofdstuk 3**. In het bijzonder hebben we het belang aangetoond van warmtestabilisatie om de endogene metabolieten en lipiden in de kraakbeenmonsters te behouden. Ook lieten we de potentie zien van een experimenteel ontwerp methodiek om de stabilisatiestap te optimaliseren. Deze aanpak liet ook zien hoe kleine veranderingen de datakwaliteit drastisch kunnen verbeteren of verminderen. Tenslotte werd de geoptimaliseerde MALDI-MSI methode gevalideerd met behulp van een instrument met hoge massa resolutie en vertoonde een hogere metabolische activiteit in de oppervlakkige laag van het kraakbeen.

In **hoofdstuk 4** werd de MALDI-MSI technologie toegepast voor lipidenanalyse en gecombineerd met labelvrije proteoom analyses om de verschillende moleculaire kraakbeenprofielen van OA/T2DM^{-} en OA/T2DM^{+} fenotypes te onthullen. Ons werk toonde specifieke lipiden geassocieerd met elk fenotype, evenals verschillen in fosfolipidengehaltes tussen oppervlakkige en diepe lagen van het kraakbeen. We benadrukten ook de noodzaak om apolipoproteïne A1 en fosfolipase A2 te onderzoeken in een grotere cohortstudie en voor verdere functionele analyse.

In **hoofdstuk 5** hebben we labelvrije proteomics en transcriptomics gecombineerd om een mogelijke nieuwe rol van het SOX9 gen te ontdekken, waarvan bekend is dat het betrokken is bij het chondrogenese proces. We wezen op een nieuwe functie van het SOX9 gen tijdens vroege stadia van chondrogene differentiatie en toonden de betrokkenheid bij zowel ribosomale translatie als bij het translatievermogen van eiwitten. Onze gegevens suggereren ook een rol voor vroege SOX9 bij de priming

van de voorlopercellen in het chrondogene differentiatieproces voor kraakbeenachtige ECM.

De valorisatie van dit proefschrift wordt gepresenteerd in **hoofdstuk 6**. Hier wordt de noodzaak om een multimodale aanpak te overwegen om de classificatie van fenotypes te verbeteren benadrukt. Vervolgens wordt het ontwerp van de experimenten beschreven als een nieuwe strategie om een MALDI-MSI methode te optimaliseren. Ten slotte hebben we het warmtestabilisatie proces gedemonstreerd om biologische veranderingen te voorkomen, wat bijdraagt aan nauwkeurigere en reproduceerbare resultaten.

APPENDIX

References

1. Fassbender, H.G. *The History of Rheumatic Diseases.* Pathology of Rheumatic Diseases, 1975.
2. Rothschild, B. *Contributions of paleorheumatology to understanding contemporary disease.* Reumatismo, 2002. **54**(3): p. 272-84.
3. Sacitharan, P.K. *Ageing and Osteoarthritis.* Subcell Biochem, 2019. **91**: p. 123-159.
4. Zhang, Y.Q. and J.M. Jordan. *Epidemiology of Osteoarthritis.* Clinics in Geriatric Medicine, 2010. **26**(3): p. 355-+.
5. Haq, I., E. Murphy, and J. Dacre. *Osteoarthritis.* Postgrad Med J, 2003. **79**(933): p. 377-83.
6. Dell'Isola, A., et al. *Identification of clinical phenotypes in knee osteoarthritis: a systematic review of the literature.* BMC Musculoskelet Disord, 2016. **17**(1): p. 425.
7. Herrero-Beaumont, G., et al. *Clinical settings in knee osteoarthritis: Pathophysiology guides treatment.* Maturitas, 2017. **96**: p. 54-57.
8. Mobasheri, A., et al. *Recent advances in understanding the phenotypes of osteoarthritis.* F1000Res, 2019. **8**.
9. da Cunha, V.R., et al. *Rheumatoid arthritis and metabolic syndrome.* Rev Bras Reumatol, 2011. **51**(3): p. 260-8.
10. Courties, A., J. Sellam, and F. Berenbaum. *Metabolic syndrome-associated osteoarthritis.* Curr Opin Rheumatol, 2017. **29**(2): p. 214-222.
11. Le Clanche, S., et al. *Inter-relations between osteoarthritis and metabolic syndrome: A common link?* Biochimie, 2016. **121**: p. 238-252.
12. Sherling, D.H., P. Perumareddi, and C.H. Hennekens. *Metabolic Syndrome: Clinical and Policy Implications of the New Silent Killer.* Journal of Cardiovascular Pharmacology and Therapeutics, 2017. **22**(4): p. 365-367.
13. Mendrick, D.L., et al. *Metabolic Syndrome and Associated Diseases: From the Bench to the Clinic.* Toxicol Sci, 2018. **162**(1): p. 36-42.
14. Courties, A., F. Berenbaum, and J. Sellam. *The Phenotypic Approach to Osteoarthritis: A Look at Metabolic Syndrome-Associated Osteoarthritis.* Joint Bone Spine, 2018.
15. Louati, K., et al. *Association between diabetes mellitus and osteoarthritis: systematic literature review and meta-analysis.* Rmd Open, 2015. **1**(1).
16. Williams, M.F., et al. *Type 2 diabetes and osteoarthritis: a systematic review and meta-analysis.* Journal of Diabetes and Its Complications, 2016. **30**(5): p. 944-950.
17. Veronese, N., et al. *Type 2 diabetes mellitus and osteoarthritis.* Seminars in Arthritis and Rheumatism, 2019. **49**(1): p. 9-19.
18. Courties, A. and J. Sellam. *Osteoarthritis and type 2 diabetes mellitus: What are the links?* Diabetes Research and Clinical Practice, 2016. **122**: p. 198-206.
19. Macdonald, I.A. *A review of recent evidence relating to sugars, insulin resistance and diabetes.* European Journal of Nutrition, 2016. **55**: p. S17-S23.
20. Sears, B. and M. Perry. *The role of fatty acids in insulin resistance.* Lipids in Health and Disease, 2015. **14**.

21. Heidari, B. *Knee osteoarthritis prevalence, risk factors, pathogenesis and features: Part I.* Caspian J Intern Med, 2011. **2**(2): p. 205-12.
22. Cretu, D., E.P. Diamandis, and V. Chandran. *Delineating the synovial fluid proteome: recent advancements and ongoing challenges in biomarker research.* Crit Rev Clin Lab Sci, 2013. **50**(2): p. 51-63.
23. Buckwalter, J.A. and L.C. Rosenberg. *Electron microscopic studies of cartilage proteoglycans.* Electron Microsc Rev, 1988. **1**(1): p. 87-112.
24. Sophia Fox, A.J., A. Bedi, and S.A. Rodeo. *The basic science of articular cartilage: structure, composition, and function.* Sports Health, 2009. **1**(6): p. 461-8.
25. Huang, Y.Z., et al. *Mesenchymal Stem/Progenitor Cells Derived from Articular Cartilage, Synovial Membrane and Synovial Fluid for Cartilage Regeneration: Current Status and Future Perspectives.* Stem Cell Rev Rep, 2017. **13**(5): p. 575-586.
26. Revell, P.A., et al. *Extracellular matrix of the synovial intimal cell layer.* Ann Rheum Dis, 1995. **54**(5): p. 404-7.
27. Smith, M.D. *The normal synovium.* Open Rheumatol J, 2011. **5**: p. 100-6.
28. de Sousa, E.B., et al. *Synovial fluid and synovial membrane mesenchymal stem cells: latest discoveries and therapeutic perspectives.* Stem Cell Res Ther, 2014. **5**(5): p. 112.
29. Tamer, T.M. *Hyaluronan and synovial joint: function, distribution and healing.* Interdiscip Toxicol, 2013. **6**(3): p. 111-25.
30. Ward, P.C. *Interpretation of synovial fluid data.* Postgrad Med, 1980. **68**(3): p. 175-9, 182-4.
31. Tercic, D. and B. Bozic. *The basis of the synovial fluid analysis.* Clin Chem Lab Med, 2001. **39**(12): p. 1221-6.
32. Suri, S. and D.A. Walsh. *Osteochondral alterations in osteoarthritis.* Bone, 2012. **51**(2): p. 204-11.
33. Lyons, T.J., et al. *The normal human chondro-osseous junctional region: evidence for contact of uncalcified cartilage with subchondral bone and marrow spaces.* BMC Musculoskelet Disord, 2006. **7**: p. 52.
34. Walsh, D.A., et al. *Angiogenesis in the synovium and at the osteochondral junction in osteoarthritis.* Osteoarthritis Cartilage, 2007. **15**(7): p. 743-51.
35. Suri, S., et al. *Neurovascular invasion at the osteochondral junction and in osteophytes in osteoarthritis.* Ann Rheum Dis, 2007. **66**(11): p. 1423-8.
36. Nakano, T., et al. *Chemical composition of the infrapatellar fat pad of swine.* J Anat, 2004. **204**(4): p. 301-6.
37. Wang, X., et al. *The importance of synovial inflammation in osteoarthritis: current evidence from imaging assessments and clinical trials.* Osteoarthritis Cartilage, 2018. **26**(2): p. 165-174.
38. Li, G.Y., et al. *Subchondral bone in osteoarthritis: insight into risk factors and microstructural changes.* Arthritis Research & Therapy, 2013. **15**(6).
39. Goldring, M.B. and M. Otero. *Inflammation in osteoarthritis.* Curr Opin Rheumatol, 2011. **23**(5): p. 471-8.
40. Ioan-Facsinay, A. and M. Kloppenburg. *An emerging player in knee osteoarthritis: the infrapatellar fat pad.* Arthritis Res Ther, 2013. **15**(6): p. 225.

41. Di Girolamo, F., et al. *The Role of Mass Spectrometry in the "Omics" Era.* Curr Org Chem, 2013. **17**(23): p. 2891-2905.
42. Ojanpera, I., M. Kolmonen, and A. Pelander. *Current use of high-resolution mass spectrometry in drug screening relevant to clinical and forensic toxicology and doping control.* Analytical and Bioanalytical Chemistry, 2012. **403**(5): p. 1203-1220.
43. Gan, H.H., C. Soukoulis, and I. Fisk. *Atmospheric pressure chemical ionisation mass spectrometry analysis linked with chemometrics for food classification - A case study: Geographical provenance and cultivar classification of monovarietal clarified apple juices.* Food Chemistry, 2014. **146**: p. 149-156.
44. Hopfgartner, G., D. Tonoli, and E. Varesio. *High-resolution mass spectrometry for integrated qualitative and quantitative analysis of pharmaceuticals in biological matrices.* Analytical and Bioanalytical Chemistry, 2012. **402**(8): p. 2587-2596.
45. Cohen, A. *Mass Spectrometry, Review of the Basics: Electrospray, MALDI and Commonly Used Mass Analyzers (vol 44, pg 210, 2009).* Applied Spectroscopy Reviews, 2009. **44**(4): p. 362-362.
46. Norris, J.L. and R.M. Caprioli. *Analysis of tissue specimens by matrix-assisted laser desorption/ionization imaging mass spectrometry in biological and clinical research.* Chem Rev, 2013. **113**(4): p. 2309-42.
47. Caprioli, R.M., T.B. Farmer, and J. Gile. *Molecular imaging of biological samples: localization of peptides and proteins using MALDI-TOF MS.* Anal Chem, 1997. **69**(23): p. 4751-60.
48. Gemperline, E., B. Chen, and L. Li. *Challenges and recent advances in mass spectrometric imaging of neurotransmitters.* Bioanalysis, 2014. **6**(4): p. 525-40.
49. Buchberger, A.R., et al. *Mass Spectrometry Imaging: A Review of Emerging Advancements and Future Insights.* Anal Chem, 2018. **90**(1): p. 240-265.
50. Bowman, A.P., et al. *Evaluation of lipid coverage and high spatial resolution MALDI-imaging capabilities of oversampling combined with laser post-ionisation.* Anal Bioanal Chem, 2020. **412**(10): p. 2277-2289.
51. Bakker, B., et al. *Oxygen-Dependent Lipid Profiles of Three-Dimensional Cultured Human Chondrocytes Revealed by MALDI-MSI.* Anal Chem, 2017. **89**(17): p. 9438-9444.
52. Rocha, B., et al. *Characterization of lipidic markers of chondrogenic differentiation using mass spectrometry imaging.* Proteomics, 2015. **15**(4): p. 702-13.
53. Cillero-Pastor, B., et al. *Protein classification and distribution in osteoarthritic human synovial tissue by matrix-assisted laser desorption ionization mass spectrometry imaging.* Anal Bioanal Chem, 2015. **407**(8): p. 2213-22.
54. Briggs, M.T., et al. *MALDI mass spectrometry imaging of N-glycans on tibial cartilage and subchondral bone proteins in knee osteoarthritis.* Proteomics, 2016. **16**(11-12): p. 1736-41.
55. Cillero-Pastor, B., et al. *Matrix-assisted laser desorption ionization-imaging mass spectrometry: a new methodology to study human osteoarthritic cartilage.* Arthritis Rheum, 2013. **65**(3): p. 710-20.
56. Cillero-Pastor, B., et al. *Time-of-flight secondary ion mass spectrometry-based molecular distribution distinguishing healthy and osteoarthritic human cartilage.* Anal Chem, 2012. **84**(21): p. 8909-16.
57. Wu, S. and F. De Luca. *Role of cholesterol in the regulation of growth plate chondrogenesis and longitudinal bone growth.* J Biol Chem, 2004. **279**(6): p. 4642-7.

58. Lawrence, R.C., et al. *Estimates of the prevalence of arthritis and other rheumatic conditions in the United States.* Arthritis and Rheumatism, 2008. **58**(1): p. 26-35.
59. Lin, Y., et al. *Plasma MicroRNA-34a as a Potential Biomarker for Early Diagnosis of Esophageal Cancer.* Clin Lab, 2019. **65**(11).
60. Underwood, P.W., et al. *Protein Signatures and Tissue Diagnosis of Pancreatic Cancer.* J Am Coll Surg, 2019.
61. Ourradi, K. and M. Sharif. *Opportunities and challenges for the discovery and validation of proteomic biomarkers for common arthritic diseases.* Biomarkers in Medicine, 2017. **11**(10): p. 877-892.
62. Ruiz-Romero, C., et al. *Lessons from the proteomic study of osteoarthritis.* Expert Rev Proteomics, 2015. **12**(4): p. 433-43.
63. Ruiz-Romero, C. and F.J. Blanco. *Proteomics role in the search for improved diagnosis, prognosis and treatment of osteoarthritis.* Osteoarthritis Cartilage, 2010. **18**(4): p. 500-9.
64. Peng, J. and S.P. Gygi. *Proteomics: the move to mixtures.* J Mass Spectrom, 2001. **36**(10): p. 1083-91.
65. Steen, H. and M. Mann. *The ABC's (and XYZ's) of peptide sequencing.* Nat Rev Mol Cell Biol, 2004. **5**(9): p. 699-711.
66. Zhang, Y., et al. *Protein analysis by shotgun/bottom-up proteomics.* Chem Rev, 2013. **113**(4): p. 2343-94.
67. Richards, A.L., et al. *One-hour proteome analysis in yeast.* Nat Protoc, 2015. **10**(5): p. 701-14.
68. Nesvizhskii, A.I. *Protein identification by tandem mass spectrometry and sequence database searching.* Methods Mol Biol, 2007. **367**: p. 87-119.
69. Tsiatsiani, L. and A.J. Heck. *Proteomics beyond trypsin.* FEBS J, 2015. **282**(14): p. 2612-26.
70. Glatter, T., et al. *Large-scale quantitative assessment of different in-solution protein digestion protocols reveals superior cleavage efficiency of tandem Lys-C/trypsin proteolysis over trypsin digestion.* J Proteome Res, 2012. **11**(11): p. 5145-56.
71. Folkesson, E., et al. *Differences in Protein Expression Using Data-Dependent and Data-Independent Acquisition Mass Spectrometry in the Analysis of Human Knee Articular Cartilage and Menisci: A Pilot Analysis.* Osteoarthritis and Cartilage, 2017. **25**: p. S383-S383.
72. Liao, W.X., et al. *Proteomic analysis of synovial fluid in osteoarthritis using SWATH-mass spectrometry.* Molecular Medicine Reports, 2018. **17**(2): p. 2827-2836.
73. Luo, H.L., et al. *Liquid chromatography-mass spectrometry-based quantitative proteomics analysis reveals chondroprotective effects of astragaloside IV in interleukin-1 beta-induced SW1353 chondrocyte-like cells.* Biomedicine & Pharmacotherapy, 2017. **91**: p. 796-802.
74. Lourido, L., et al. *Secretome analysis of human articular chondrocytes unravels catabolic effects of nicotine on the joint.* Proteomics Clinical Applications, 2016. **10**(6): p. 671-680.
75. Moradian, A., et al. *The top-down, middle-down, and bottom-up mass spectrometry approaches for characterization of histone variants and their post-translational modifications.* Proteomics, 2014. **14**(4-5): p. 489-97.

76. Meyer, B., D.G. Papasotiriou, and M. Karas. *100% protein sequence coverage: a modern form of surrealism in proteomics.* Amino Acids, 2011. **41**(2): p. 291-310.
77. Han, X., A. Aslanian, and J.R. Yates, 3rd. *Mass spectrometry for proteomics.* Curr Opin Chem Biol, 2008. **12**(5): p. 483-90.
78. Patrie, S.M. *Top-Down Mass Spectrometry: Proteomics to Proteoforms.* Adv Exp Med Biol, 2016. **919**: p. 171-200.
79. Smith, L.M., N.L. Kelleher, and P. Consortium for Top Down. *Proteoform: a single term describing protein complexity.* Nat Methods, 2013. **10**(3): p. 186-7.
80. Ge, H.X., et al. *JNK pathway in osteoarthritis: pathological and therapeutic aspects.* Journal of Receptors and Signal Transduction, 2017. **37**(5): p. 431-436.
81. Luck, K., et al. *Proteome-Scale Human Interactomics.* Trends Biochem Sci, 2017. **42**(5): p. 342-354.
82. Huttlin, E.L., et al. *The BioPlex Network: A Systematic Exploration of the Human Interactome.* Cell, 2015. **162**(2): p. 425-440.
83. Rolland, T., et al. *A proteome-scale map of the human interactome network.* Cell, 2014. **159**(5): p. 1212-1226.
84. Hein, M.Y., et al. *A human interactome in three quantitative dimensions organized by stoichiometries and abundances.* Cell, 2015. **163**(3): p. 712-23.
85. Wan, C., et al. *Panorama of ancient metazoan macromolecular complexes.* Nature, 2015. **525**(7569): p. 339-44.
86. Holding, A.N. *XL-MS: Protein cross-linking coupled with mass spectrometry.* Methods, 2015. **89**: p. 54-63.
87. Chughtai, K. and R.M. Heeren. *Mass spectrometric imaging for biomedical tissue analysis.* Chem Rev, 2010. **110**(5): p. 3237-77.
88. Passarelli, M.K., et al. *The 3D OrbiSIMS-label-free metabolic imaging with subcellular lateral resolution and high mass-resolving power.* Nat Methods, 2017. **14**(12): p. 1175-1183.
89. Kriegsmann, K., et al. *Combined Immunohistochemistry after Mass Spectrometry Imaging for Superior Spatial Information.* Proteomics Clin Appl, 2019. **13**(1): p. e1800035.
90. Groseclose, M.R., et al. *Identification of proteins directly from tissue: in situ tryptic digestions coupled with imaging mass spectrometry.* J Mass Spectrom, 2007. **42**(2): p. 254-62.
91. Lemaire, R., et al. *Direct analysis and MALDI imaging of formalin-fixed, paraffin-embedded tissue sections.* J Proteome Res, 2007. **6**(4): p. 1295-305.
92. Peffers, M.J., et al. *Matrix assisted laser desorption ionization mass spectrometry imaging identifies markers of ageing and osteoarthritic cartilage.* Arthritis Res Ther, 2014. **16**(3): p. R110.
93. Kriegsmann, M., et al. *MALDI MS imaging as a powerful tool for investigating synovial tissue.* Scand J Rheumatol, 2012. **41**(4): p. 305-9.
94. Klein, O., et al. *Unraveling local tissue changes within severely injured skeletal muscles in response to MSC-based intervention using MALDI Imaging mass spectrometry.* Sci Rep, 2018. **8**(1): p. 12677.
95. Powers, T.W., et al. *Matrix assisted laser desorption ionization imaging mass spectrometry workflow for spatial profiling analysis of N-linked glycan expression in tissues.* Anal Chem, 2013. **85**(20): p. 9799-806.

96. Urita, A., et al. *Alterations of high-mannose type N-glycosylation in human and mouse osteoarthritis cartilage.* Arthritis Rheum, 2011. **63**(11): p. 3428-38.
97. Heijs, B., et al. *Multimodal Mass Spectrometry Imaging of N-Glycans and Proteins from the Same Tissue Section.* Anal Chem, 2016. **88**(15): p. 7745-53.
98. Angel, P.M., et al. *Mapping Extracellular Matrix Proteins in Formalin-Fixed, Paraffin-Embedded Tissues by MALDI Imaging Mass Spectrometry.* J Proteome Res, 2018. **17**(1): p. 635-646.
99. Wisztorski, M., et al. *Microproteomics by liquid extraction surface analysis: application to FFPE tissue to study the fimbria region of tubo-ovarian cancer.* Proteomics Clin Appl, 2013. **7**(3-4): p. 234-40.
100. Quanico, J., et al. *Development of liquid microjunction extraction strategy for improving protein identification from tissue sections.* J Proteomics, 2013. **79**: p. 200-18.
101. Espina, V., et al. *Laser-capture microdissection.* Nat Protoc, 2006. **1**(2): p. 586-603.
102. Hondius, D.C., et al. *Profiling the human hippocampal proteome at all pathologic stages of Alzheimer's disease.* Alzheimers Dement, 2016. **12**(6): p. 654-68.
103. Valleix, S., et al. *D25V apolipoprotein C-III variant causes dominant hereditary systemic amyloidosis and confers cardiovascular protective lipoprotein profile.* Nat Commun, 2016. **7**: p. 10353.
104. Nijholt, D.A., C. Stingl, and T.M. Luider. *Laser capture microdissection of fluorescently labeled amyloid plaques from Alzheimer's disease brain tissue for mass spectrometric analysis.* Methods Mol Biol, 2015. **1243**: p. 165-73.
105. Ezzoukhry, Z., et al. *Combining laser capture microdissection and proteomics reveals an active translation machinery controlling invadosome formation.* Nat Commun, 2018. **9**(1): p. 2031.
106. Hsueh, M.F., V.B. Kraus, and P. Onnerfjord. *Cartilage matrix remodelling differs by disease state and joint type.* Eur Cell Mater, 2017. **34**: p. 70-82.
107. Dilillo, M., et al. *Mass Spectrometry Imaging, Laser Capture Microdissection, and LC-MS/MS of the Same Tissue Section.* J Proteome Res, 2017. **16**(8): p. 2993-3001.
108. Dewez, F., et al. *Precise co-registration of mass spectrometry imaging, histology, and laser microdissection-based omics.* Anal Bioanal Chem, 2019. **411**(22): p. 5647-5653.
109. Alberts, D., et al. *MALDI Imaging-Guided Microproteomic Analyses of Heterogeneous Breast Tumors-A Pilot Study.* Proteomics Clin Appl, 2018. **12**(1).
110. Parra, E.R. *Novel platforms of multiplexed immunofluorescence for study of paraffin tumor tissues.* J Cancer Treat Diagnosis, 2018. **2**: p. 42-53.
111. Chang, Q., et al. *Biodistribution of cisplatin revealed by imaging mass cytometry identifies extensive collagen binding in tumor and normal tissues.* Sci Rep, 2016. **6**: p. 36641.
112. Giesen, C., et al. *Highly multiplexed imaging of tumor tissues with subcellular resolution by mass cytometry.* Nat Methods, 2014. **11**(4): p. 417-22.
113. Angelo, M., et al. *Multiplexed ion beam imaging of human breast tumors.* Nat Med, 2014. **20**(4): p. 436-42.
114. Bodenmiller, B. *Multiplexed Epitope-Based Tissue Imaging for Discovery and Healthcare Applications.* Cell Syst, 2016. **2**(4): p. 225-38.
115. Paleja, B., et al. *Microenvironmental and Systematic Evaluation of the Immunome in Osteoarthritis.* Arthritis & Rheumatology, 2017. **69**.

116. Nair, N., et al. *Mass cytometry as a platform for the discovery of cellular biomarkers to guide effective rheumatic disease therapy.* Arthritis Res Ther, 2015. **17**: p. 127.
117. Lahiri, S., et al. *MALDI imaging mass spectrometry as a novel tool for detecting histone modifications in clinical tissue samples.* Expert Rev Proteomics, 2016. **13**(3): p. 275-84.
118. Gonzalez Gil, A.B., R. Llombart Blanco, and P. Diaz de Rada. *Validity of magnetic resonance arthrography as a diagnostic tool in femoroacetabular impingement syndrome.* Rev Esp Cir Ortop Traumatol, 2015. **59**(4): p. 281-6.
119. Helmick, C.G., et al. *Estimates of the prevalence of arthritis and other rheumatic conditions in the United States. Part I.* Arthritis Rheum, 2008. **58**(1): p. 15-25.
120. Vos, T., et al. *Global, regional, and national incidence, prevalence, and years lived with disability for 328 diseases and injuries for 195 countries, 1990-2016: a systematic analysis for the Global Burden of Disease Study 2016.* Lancet, 2017. **390**(10100): p. 1211-1259.
121. Bhattaram, P. and U. Chandrasekharan. *The joint synovium: A critical determinant of articular cartilage fate in inflammatory joint diseases.* Semin Cell Dev Biol, 2017. **62**: p. 86-93.
122. Braun, H.J. and G.E. Gold. *Diagnosis of osteoarthritis: imaging.* Bone, 2012. **51**(2): p. 278-88.
123. Hasegawa, A., et al. *Anterior cruciate ligament changes in the human knee joint in aging and osteoarthritis.* Arthritis Rheum, 2012. **64**(3): p. 696-704.
124. Aho, O.M., et al. *Subchondral bone histology and grading in osteoarthritis.* PLoS One, 2017. **12**(3): p. e0173726.
125. Mobasheri, A., et al. *The role of metabolism in the pathogenesis of osteoarthritis.* Nat Rev Rheumatol, 2017. **13**(5): p. 302-311.
126. Ruiz-Romero, C., I. Rego-Perez, and F.J. Blanco. *What did we learn from 'omics' studies in osteoarthritis.* Current opinion in rheumatology, 2018. **30**(1): p. 114-120.
127. Cillero-Pastor, B., et al. *Time-of-Flight Secondary Ion Mass Spectrometry-Based Molecular Distribution Distinguishing Healthy and Osteoarthritic Human Cartilage.* Analytical Chemistry, 2012. **84**(21): p. 8909-8916.
128. Cillero-Pastor, B. and R.M. Heeren. *Matrix-assisted laser desorption ionization mass spectrometry imaging for peptide and protein analyses: a critical review of on-tissue digestion.* J Proteome Res, 2014. **13**(2): p. 325-35.
129. Fagerer, S.R., et al. *Matrix-assisted laser desorption/ionization matrices for negative mode metabolomics.* Eur J Mass Spectrom (Chichester), 2013. **19**(1): p. 39-47.
130. Cerruti, C.D., et al. *MALDI imaging and structural analysis of rat brain lipid negative ions with 9-aminoacridine matrix.* Anal Chem, 2012. **84**(5): p. 2164-71.
131. Amantonico, A., et al. *Mass spectrometric method for analyzing metabolites in yeast with single cell sensitivity.* Angew Chem Int Ed Engl, 2008. **47**(29): p. 5382-5.
132. Vaidyanathan, S. and R. Goodacre. *Quantitative detection of metabolites using matrix-assisted laser desorption/ionization mass spectrometry with 9-aminoacridine as the matrix.* Rapid Commun Mass Spectrom, 2007. **21**(13): p. 2072-8.
133. Guillaume-Gentil, O., et al. *Single-Cell Mass Spectrometry of Metabolites Extracted from Live Cells by Fluidic Force Microscopy.* Anal Chem, 2017. **89**(9): p. 5017-5023.
134. Hennebelle, M., et al. *Brain oxylipin concentrations following hypercapnia / ischemia: effects of brain dissection and dissection time.* J Lipid Res, 2018.

135. Alashmali, S.M., et al. *Maternal dietary n-6 polyunsaturated fatty acid deprivation does not exacerbate post-weaning reductions in arachidonic acid and its mediators in the mouse hippocampus.* Nutr Neurosci, 2017: p. 1-12.
136. Pawlosky, R.J., et al. *Alterations in brain glucose utilization accompanying elevations in blood ethanol and acetate concentrations in the rat.* Alcohol Clin Exp Res, 2010. **34**(2): p. 375-81.
137. Murphy, E.J. *Brain fixation for analysis of brain lipid-mediators of signal transduction and brain eicosanoids requires head-focused microwave irradiation: an historical perspective.* Prostaglandins Other Lipid Mediat, 2010. **91**(3-4): p. 63-7.
138. Svensson, M., et al. *Heat stabilization of the tissue proteome: a new technology for improved proteomics.* J Proteome Res, 2009. **8**(2): p. 974-81.
139. Boren, M. *Preservation of Specific Protein Signaling States Using Heat Based Stabilizor System.* Methods Mol Biol, 2017. **1554**: p. 143-153.
140. Esteve, C., et al. *Mass spectrometry imaging of amino neurotransmitters: a comparison of derivatization methods and application in mouse brain tissue.* Metabolomics, 2016. **12**: p. 30.
141. Barre, F.P.Y., et al. *Specific lipid and metabolic profiles of R-CHOP-resistant diffuse large B-cell lymphoma elucidated by matrix-assisted laser desorption ionization mass spectrometry imaging and in vivo imaging.* Anal Chem, 2018.
142. Caffrey, R.E. *A review of experimental design best practices for proteomics based biomarker discovery: focus on SELDI-TOF.* Methods Mol Biol, 2010. **641**: p. 167-83.
143. Hibbert, D.B. *Experimental design in chromatography: a tutorial review.* J Chromatogr B Analyt Technol Biomed Life Sci, 2012. **910**: p. 2-13.
144. Duke, F. and K. Jen. *Response to Protocol Review Scenario: The answers are in experimental design.* Lab Anim (NY), 2016. **45**(1): p. 14.
145. Aexd.net. *Alleviating Science, Heerlen, The Netherlands,* . version 1.0.32, Alleviating Science, Heerlen, The Netherlands, 2018; software available at https://aexd.net.
146. Eijkel, G.B., et al. *Correlating MALDI and SIMS imaging mass spectrometric datasets of biological tissue surfaces.* Surface and Interface Analysis, 2009. **41**(8): p. 675-685.
147. Blatherwick, E.Q., et al. *Localisation of adenine nucleotides in heat-stabilised mouse brains using ion mobility enabled MALDI imaging.* International Journal of Mass Spectrometry, 2013. **345**: p. 19-27.
148. Morikawa-Ichinose, T., et al. *Improvement of Sensitivity and Reproducibility for Imaging of Endogenous Metabolites by Matrix-Assisted Laser Desorption/Ionization-Mass Spectrometry.* J Am Soc Mass Spectrom, 2019.
149. Hartler, J., et al. *Bioinformatics tools and challenges in structural analysis of lipidomics MS/MS data.* Briefings in Bioinformatics, 2013. **14**(3): p. 375-390.
150. Sparvero, L.J., et al. *Mapping of phospholipids by MALDI imaging (MALDI-MSI): realities and expectations.* Chemistry and Physics of Lipids, 2012. **165**(5): p. 545-562.
151. Hiraide, T., et al. *Accumulation of arachidonic acid-containing phosphatidylinositol at the outer edge of colorectal cancer.* Scientific Reports, 2016. **6**.

152. Taylor, A.J., A. Dexter, and J. Bunch. *Exploring Ion Suppression in Mass Spectrometry Imaging of a Heterogeneous Tissue.* Anal Chem, 2018. **90**(9): p. 5637-5645.
153. Huang, Y.Z., et al. *Mesenchymal Stem/Progenitor Cells Derived from Articular Cartilage, Synovial Membrane and Synovial Fluid for Cartilage Regeneration: Current Status and Future Perspectives.* Stem Cell Rev, 2017. **13**(5): p. 575-586.
154. Helmick, C.G., et al. *Estimates of the prevalence of arthritis and other rheumatic conditions in the United States.* Arthritis and Rheumatism, 2008. **58**(1): p. 15-25.
155. Loeser, R.F. *Aging and osteoarthritis.* Current Opinion in Rheumatology, 2011. **23**(5): p. 492-496.
156. Bruyere, O., et al. *Can We Identify Patients with High Risk of Osteoarthritis Progression Who Will Respond to Treatment? A Focus on Epidemiology and Phenotype of Osteoarthritis (vol 32, pg 179, 2015).* Drugs & Aging, 2017. **34**(5): p. 411-411.
157. Van Spil, W.E., et al. *Osteoarthritis phenotypes and novel therapeutic targets.* Biochemical Pharmacology, 2019. **165**: p. 41-48.
158. Dell'Isola, A., et al. *Identification of clinical phenotypes in knee osteoarthritis: a systematic review of the literature.* Bmc Musculoskeletal Disorders, 2016. **17**.
159. Courties, A. and J. Sellam. *Osteoarthritis and type 2 diabetes mellitus: What are the links?* Diabetes Res Clin Pract, 2016. **122**: p. 198-206.
160. Eveque-Mourroux, M.R., et al. *Spatially resolved endogenous improved metabolite detection in human osteoarthritis cartilage by matrix assisted laser desorption ionization mass spectrometry imaging.* Analyst, 2019. **144**(20): p. 5953-5958.
161. Kultima, K., K. Skold, and M. Boren. *Biomarkers of disease and post-mortem changes - Heat stabilization, a necessary tool for measurement of protein regulation.* J Proteomics, 2011. **75**(1): p. 145-59.
162. Jerneren, F., M. Soderquist, and O. Karlsson. *Post-sampling release of free fatty acids - effects of heat stabilization and methods of euthanasia.* J Pharmacol Toxicol Methods, 2015. **71**: p. 13-20.
163. Chen, E.Y., et al. *Enrichr: interactive and collaborative HTML5 gene list enrichment analysis tool.* BMC Bioinformatics, 2013. **14**: p. 128.
164. Barre, F., et al. *Faster raster matrix-assisted laser desorption/ionization mass spectrometry imaging of lipids at high lateral resolution.* International Journal of Mass Spectrometry, 2019. **437**: p. 38-48.
165. Ellis, S.R., et al. *Automated, parallel mass spectrometry imaging and structural identification of lipids.* Nat Methods, 2018. **15**(7): p. 515-518.
166. Tortorella, S., et al. *LipostarMSI: Comprehensive, Vendor-Neutral Software for Visualization, Data Analysis, and Automated Molecular Identification in Mass Spectrometry Imaging.* Journal of the American Society for Mass Spectrometry, 2020. **31**(1): p. 155-163.
167. Pauling, J.K., et al. *Proposal for a common nomenclature for fragment ions in mass spectra of lipids.* PLoS One, 2017. **12**(11): p. e0188394.
168. Attie, A.D., J.P. Kastelein, and M.R. Hayden. *Pivotal role of ABCA1 in reverse cholesterol transport influencing HDL levels and susceptibility to atherosclerosis.* Journal of Lipid Research, 2001. **42**(11): p. 1717-1726.

169. de Seny, D., et al. *Apolipoprotein-A1 as a Damage-Associated Molecular Patterns Protein in Osteoarthritis: Ex Vivo and In Vitro Pro-Inflammatory Properties.* Plos One, 2015. **10**(4).
170. Lourido, L., et al. *Identification of a Serum Protein Biomarker Panel for the Diagnosis of Knee Osteoarthritis.* Osteoarthritis and Cartilage, 2016. **24**: p. S23-S23.
171. Wu, X., et al. *Low levels of ApoA1 improve risk prediction of type 2 diabetes mellitus.* J Clin Lipidol, 2017. **11**(2): p. 362-368.
172. Higgins, A.J. and P. Lees. *The acute inflammatory process, arachidonic acid metabolism and the mode of action of anti-inflammatory drugs.* Equine Vet J, 1984. **16**(3): p. 163-75.
173. Monroy-Munoz, I.E., et al. *PLA2G2A polymorphisms are associated with metabolic syndrome and type 2 diabetes mellitus. Results from the genetics of atherosclerotic disease Mexican study.* Immunobiology, 2017. **222**(10): p. 967-972.
174. Lopes, M.B., et al. *mRNA-miRNA integrative analysis of diabetes-induced cardiomyopathy in rats.* Front Biosci (Schol Ed), 2017. **9**: p. 194-229.
175. Zhai, G.J., et al. *Activation of The Phosphatidylcholine to Lysophosphatidylcholine Pathway Is Associated with Osteoarthritis Knee Cartilage Volume Loss Over Time.* Scientific Reports, 2019. **9**.
176. Lourido, L., et al. *Proteomics Analysis Of Cartilage Secretome: A Powerful Tool For The Discovery Of OA Biomarkers.* Arthritis and Rheumatism, 2013. **65**: p. S800-S800.
177. Poulet, B. and F. Beier. *Targeting oxidative stress to reduce osteoarthritis.* Arthritis Res Ther, 2016. **18**: p. 32.
178. Lepetsos, P. and A.G. Papavassiliou. *ROS/oxidative stress signaling in osteoarthritis.* Biochim Biophys Acta, 2016. **1862**(4): p. 576-591.
179. Zhu, S.A., et al. *Glutathione as a mediator of cartilage oxidative stress resistance and resilience during aging and osteoarthritis.* Connective Tissue Research, 2020. **61**(1): p. 34-47.
180. Lugrin, J., et al. *The role of oxidative stress during inflammatory processes.* Biol Chem, 2014. **395**(2): p. 203-30.
181. Fukai, T., et al. *Extracellular superoxide dismutase and cardiovascular disease.* Cardiovascular Research, 2002. **55**(2): p. 239-249.
182. Voziyan, P., et al. *Site-specific AGE modifications in the extracellular matrix: a role for glyoxal in protein damage in diabetes.* Clin Chem Lab Med, 2014. **52**(1): p. 39-45.
183. Kunjara, S., et al. *Pyrimidine nucleotide synthesis in the rat kidney in early diabetes.* Biochem Med Metab Biol, 1991. **46**(2): p. 215-25.
184. Bauer, J.A. *The urea cycle as a source of nitric oxide implicated in the pathogenesis of insulin-dependent diabetes mellitus.* Med Hypotheses, 1998. **51**(1): p. 71-3.
185. Yin, J., et al. *Metabolic Regulation of Methionine Restriction in Diabetes.* Mol Nutr Food Res, 2018. **62**(10): p. e1700951.
186. Merrill, A.H., Jr., et al. *Sphingolipids--the enigmatic lipid class: biochemistry, physiology, and pathophysiology.* Toxicol Appl Pharmacol, 1997. **142**(1): p. 208-25.
187. Harrell, C.R., et al. *Mesenchymal stem cell-based therapy of osteoarthritis: Current knowledge and future perspectives.* Biomed Pharmacother, 2019. **109**: p. 2318-2326.

188. Rocha, B., et al. *Characterization of lipidic markers of chondrogenic differentiation using mass spectrometry imaging.* Proteomics, 2015. **15**(4): p. 702-713.
189. van der Veen, J.N., et al. *The critical role of phosphatidylcholine and phosphatidylethanolamine metabolism in health and disease.* Biochimica Et Biophysica Acta-Biomembranes, 2017. **1859**(9): p. 1558-1572.
190. Matsumoto, T., T. Kobayashi, and K. Kamata. *Role of lysophosphatidylcholine (LPC) in atherosclerosis.* Curr Med Chem, 2007. **14**(30): p. 3209-20.
191. Zhang, W., et al. *Lysophosphatidylcholines to phosphatidylcholines ratio predicts advanced knee osteoarthritis.* Rheumatology (Oxford), 2016. **55**(9): p. 1566-74.
192. Rabini, R.A., et al. *Reduced Na(+)-K(+)-ATPase activity and plasma lysophosphatidylcholine concentrations in diabetic patients.* Diabetes, 1994. **43**(7): p. 915-9.
193. Han, M.S., et al. *Lysophosphatidylcholine as an effector of fatty acid-induced insulin resistance.* Journal of Lipid Research, 2011. **52**(6): p. 1234-1246.
194. Hsueh, M.F., et al. *Elucidating the Molecular Composition of Cartilage by Proteomics.* Journal of Proteome Research, 2016. **15**(2): p. 374-388.
195. Pruzanski, W., et al. *The role of phospholipase A2 in the physiopathology of osteoarthritis.* J Rheumatol Suppl, 1991. **27**: p. 117-9.
196. Sarma, A.V., G.L. Powell, and M. LaBerge. *Phospholipid composition of articular cartilage boundary lubricant.* J Orthop Res, 2001. **19**(4): p. 671-6.
197. Stockwell, R.A. *Chondrocytes.* J Clin Pathol Suppl (R Coll Pathol), 1978. **12**: p. 7-13.
198. Kosinska, M.K., et al. *Sphingolipids in human synovial fluid--a lipidomic study.* PLoS One, 2014. **9**(3): p. e91769.
199. Kronenberg, H.M. *Developmental regulation of the growth plate.* Nature, 2003. **423**(6937): p. 332-6.
200. Lefebvre, V. and P. Smits. *Transcriptional control of chondrocyte fate and differentiation.* Birth Defects Res C Embryo Today, 2005. **75**(3): p. 200-12.
201. Mackie, E.J., et al. *Endochondral ossification: how cartilage is converted into bone in the developing skeleton.* Int J Biochem Cell Biol, 2008. **40**(1): p. 46-62.
202. Abad, V., et al. *The role of the resting zone in growth plate chondrogenesis.* Endocrinology, 2002. **143**(5): p. 1851-7.
203. Karlsson, C. and A. Lindahl. *Articular cartilage stem cell signalling.* Arthritis research & therapy, 2009. **11**(4): p. 121.
204. Nakahara, H., et al. *In vivo osteochondrogenic potential of cultured cells derived from the periosteum.* Clin Orthop Relat Res, 1990(259): p. 223-32.
205. Emans, P.J., et al. *Cartilage Tissue Engineering; Lessons Learned From Periosteum.* Tissue Science & Engineering, 2011. **S2:002**.
206. Medvedev, S.P., et al. *Human induced pluripotent stem cells derived from fetal neural stem cells successfully undergo directed differentiation into cartilage.* Stem cells and development, 2011. **20**(6): p. 1099-112.
207. Barry, F.P. and J.M. Murphy. *Mesenchymal stem cells: clinical applications and biological characterization.* The international journal of biochemistry & cell biology, 2004. **36**(4): p. 568-84.

208. de Crombrugghe, B., V. Lefebvre, and K. Nakashima. *Regulatory mechanisms in the pathways of cartilage and bone formation.* Curr Opin Cell Biol, 2001. **13**(6): p. 721-7.
209. Mankin, H., V. Mow, and J. Buckwalter, *Articular cartilage structure, composition, and function*. Orthopaedic basic science, ed. J. Buckwalter, T. Einhorn, and S. Simon. 2000, Rosemont: AAOS. 443-470.
210. Foster, J.W., et al. *Campomelic dysplasia and autosomal sex reversal caused by mutations in an SRY-related gene.* Nature, 1994. **372**(6506): p. 525-30.
211. Wagner, T., et al. *Autosomal sex reversal and campomelic dysplasia are caused by mutations in and around the SRY-related gene SOX9.* Cell, 1994. **79**(6): p. 1111-20.
212. Akiyama, H., et al. *The transcription factor Sox9 has essential roles in successive steps of the chondrocyte differentiation pathway and is required for expression of Sox5 and Sox6.* Genes Dev, 2002. **16**(21): p. 2813-28.
213. Argentaro, A., et al. *A SOX9 defect of calmodulin-dependent nuclear import in campomelic dysplasia/autosomal sex reversal.* The Journal of biological chemistry, 2003. **278**(36): p. 33839-47.
214. Haudenschild, D.R., et al. *Rho kinase-dependent activation of SOX9 in chondrocytes.* Arthritis and rheumatism, 2010. **62**(1): p. 191-200.
215. Mertin, S., S.G. McDowall, and V.R. Harley. *The DNA-binding specificity of SOX9 and other SOX proteins.* Nucleic acids research, 1999. **27**(5): p. 1359-64.
216. Han, Y. and V. Lefebvre. *L-Sox5 and Sox6 drive expression of the aggrecan gene in cartilage by securing binding of Sox9 to a far-upstream enhancer.* Mol Cell Biol, 2008. **28**(16): p. 4999-5013.
217. Lefebvre, V., R.R. Behringer, and B. de Crombrugghe. *L-Sox5, Sox6 and Sox9 control essential steps of the chondrocyte differentiation pathway.* Osteoarthritis Cartilage, 2001. **9 Suppl A**: p. S69-75.
218. Lefebvre, V., et al. *SOX9 is a potent activator of the chondrocyte-specific enhancer of the pro alpha1(II) collagen gene.* Mol Cell Biol, 1997. **17**(4): p. 2336-46.
219. Lefebvre, V., P. Li, and B. de Crombrugghe. *A new long form of Sox5 (L-Sox5), Sox6 and Sox9 are coexpressed in chondrogenesis and cooperatively activate the type II collagen gene.* EMBO J, 1998. **17**(19): p. 5718-33.
220. Genzer, M.A. and L.C. Bridgewater. *A Col9a1 enhancer element activated by two interdependent SOX9 dimers.* Nucleic acids research, 2007. **35**(4): p. 1178-86.
221. Jenkins, E., et al. *The new collagen gene COL27A1 contains SOX9-responsive enhancer elements.* Matrix biology : journal of the International Society for Matrix Biology, 2005. **24**(3): p. 177-84.
222. Rentsendorj, O., et al. *Highly conserved proximal promoter element harbouring paired Sox9-binding sites contributes to the tissue- and developmental stage-specific activity of the matrilin-1 gene.* The Biochemical journal, 2005. **389**(Pt 3): p. 705-16.
223. Oh, C.D., et al. *Identification of SOX9 interaction sites in the genome of chondrocytes.* PLoS One, 2010. **5**(4): p. e10113.
224. Furumatsu, T., et al. *Smad3 induces chondrogenesis through the activation of SOX9 via CREB-binding protein/p300 recruitment.* The Journal of biological chemistry, 2005. **280**(9): p. 8343-50.
225. Caron, M.M., et al. *Activation of NF-kappaB/p65 Facilitates Early Chondrogenic Differentiation during Endochondral Ossification.* PloS one, 2012. **7**(3): p. e33467.

226. Spaapen, F., et al. *The immediate early gene product EGR1 and polycomb group proteins interact in epigenetic programming during chondrogenesis.* PLoS One, 2013. **8**(3): p. e58083.
227. Caron, M.M.J., et al. *Activation of NF-kappa B/p65 Facilitates Early Chondrogenic Differentiation during Endochondral Ossification.* Plos One, 2012. **7**(3).
228. Atsumi, T., et al. *A chondrogenic cell line derived from a differentiating culture of AT805 teratocarcinoma cells.* Cell Differ Dev, 1990. **30**(2): p. 109-16.
229. Welting, T.J., et al. *Inhibition of cyclooxygenase-2 impacts chondrocyte hypertrophic differentiation during endochondral ossification.* Eur Cell Mater, 2011. **22**: p. 420-36; discussion 436-7.
230. Robinson, M.D., D.J. McCarthy, and G.K. Smyth. *edgeR: a Bioconductor package for differential expression analysis of digital gene expression data.* Bioinformatics, 2010. **26**(1): p. 139-40.
231. McCarthy, D.J., Y. Chen, and G.K. Smyth. *Differential expression analysis of multifactor RNA-Seq experiments with respect to biological variation.* Nucleic Acids Res, 2012. **40**(10): p. 4288-97.
232. Farndale, R.W., C.A. Sayers, and A.J. Barrett. *A direct spectrophotometric microassay for sulfated glycosaminoglycans in cartilage cultures.* Connective tissue research, 1982. **9**(4): p. 247-8.
233. Goodman, C.A. and T.A. Hornberger. *Measuring protein synthesis with SUnSET: a valid alternative to traditional techniques?* Exerc Sport Sci Rev, 2013. **41**(2): p. 107-15.
234. Henrich, C.J. *A Microplate-Based Nonradioactive Protein Synthesis Assay: Application to TRAIL Sensitization by Protein Synthesis Inhibitors.* PLoS One, 2016. **11**(10): p. e0165192.
235. McCaffrey, T.A., L.A. Agarwal, and B.B. Weksler. *A rapid fluorometric DNA assay for the measurement of cell density and proliferation in vitro.* In Vitro Cell Dev Biol, 1988. **24**(3): p. 247-52.
236. Panda, A.C., J.L. Martindale, and M. Gorospe. *Polysome Fractionation to Analyze mRNA Distribution Profiles.* Bio-protocol, 2017. **7**(3): p. e2126.
237. Lefebvre, V., M. Angelozzi, and A. Haseeb. *SOX9 in cartilage development and disease.* Curr Opin Cell Biol, 2019. **61**: p. 39-47.
238. Liu, C.F., et al. *SOX9 is dispensable for the initiation of epigenetic remodeling and the activation of marker genes at the onset of chondrogenesis.* Development, 2018. **145**(14).
239. Caron, M.M., et al. *BAPX-1/NKX-3.2 acts as a chondrocyte hypertrophy molecular switch in osteoarthritis.* Arthritis Rheumatol, 2015. **67**(11): p. 2944-56.
240. Yamashita, S., et al. *Sox9 directly promotes Bapx1 gene expression to repress Runx2 in chondrocytes.* Exp Cell Res, 2009. **315**(13): p. 2231-40.
241. Liu, C.F. and V. Lefebvre. *The transcription factors SOX9 and SOX5/SOX6 cooperate genome-wide through super-enhancers to drive chondrogenesis.* Nucleic Acids Res, 2015. **43**(17): p. 8183-203.
242. Deniz, N., et al. *Translation initiation factors are not required for Dicistroviridae IRES function in vivo.* Rna, 2009. **15**(5): p. 932-46.
243. Collier, A.J., S. Tang, and R.M. Elliott. *Translation efficiencies of the 5' untranslated region from representatives of the six major genotypes of hepatitis C*

virus using a novel bicistronic reporter assay system. J Gen Virol, 1998. **79 (Pt 10)**: p. 2359-66.
244. Ray, P.S., R. Grover, and S. Das. *Two internal ribosome entry sites mediate the translation of p53 isoforms.* EMBO Rep, 2006. **7**(4): p. 404-10.
245. Trainor, P.A. and A.E. Merrill. *Ribosome biogenesis in skeletal development and the pathogenesis of skeletal disorders.* Biochim Biophys Acta, 2014. **1842**(6): p. 769-78.
246. Dowling, R.J., et al. *mTORC1-mediated cell proliferation, but not cell growth, controlled by the 4E-BPs.* Science, 2010. **328**(5982): p. 1172-6.
247. Jan, E. and P. Sarnow. *Factorless ribosome assembly on the internal ribosome entry site of cricket paralysis virus.* J Mol Biol, 2002. **324**(5): p. 889-902.
248. Godet, A.C., et al. *IRES Trans-Acting Factors, Key Actors of the Stress Response.* Int J Mol Sci, 2019. **20**(4).
249. Chaichanit, N., M. Wonglapsuwan, and W. Chotigeat. *Ribosomal protein L10A and signaling pathway.* Gene, 2018. **674**: p. 170-177.
250. Shi, Z., et al. *Heterogeneous Ribosomes Preferentially Translate Distinct Subpools of mRNAs Genome-wide.* Mol Cell, 2017. **67**(1): p. 71-83.e7.
251. Tong, D., et al. *MeCP2 facilitates breast cancer growth via promoting ubiquitination-mediated P53 degradation by inhibiting RPL5/RPL11 transcription.* Oncogenesis, 2020. **9**(5): p. 56.
252. Hao, Q., et al. *Dual regulation of p53 by the ribosome maturation factor SBDS.* Cell Death Dis, 2020. **11**(3): p. 197.
253. Xue, S., et al. *RNA regulons in Hox 5' UTRs confer ribosome specificity to gene regulation.* Nature, 2015. **517**(7532): p. 33-38.
254. Noben-Trauth, K. and J.R. Latoche. *Ectopic mineralization in the middle ear and chronic otitis media with effusion caused by RPL38 deficiency in the Tail-short (Ts) mouse.* The Journal of biological chemistry, 2011. **286**(4): p. 3079-3093.
255. Mortier, G.R., et al. *Nosology and classification of genetic skeletal disorders: 2019 revision.* Am J Med Genet A, 2019. **179**(12): p. 2393-2419.
256. Nakhoul, H., et al. *Ribosomopathies: mechanisms of disease.* Clin Med Insights Blood Disord, 2014. **7**: p. 7-16.
257. Turkiewicz, A., et al. *Current and future impact of osteoarthritis on health care: a population-based study with projections to year 2032.* Osteoarthritis Cartilage, 2014. **22**(11): p. 1826-32.

List of publications

*This thesis is based on the following four publications (*shared co-first authorship)*

• **Sox9 determines translational capacity during early chondrogenic differentiation by regulating expression of ribosome biogenesis factors and ribosomal proteins**
Caron MMJ*, Eveque-Mourroux MR*, Cillero-Pastor B, Heeren RMA, Housmans B, Cremers A, Peffers MJ, Van Rhijn LW, Van der Akker G, Welting TJ.
Submitted to Frontiers in Cell and Developmental Biology. **2021**.

• **Heterogeneity in lipid and protein cartilage profiles associated with human osteoarthritis with or without type 2 diabetes mellitus**
Eveque-Mourroux MR, Emans PJ, Boonen A, Claes BSR, Bouwman FG, Heeren RMA, Cillero-Pastor B.
Submitted to Journal of Proteome Research. **2020**. (In revision)

• **Spatially resolved proteomics in osteoarthritis: State of the art and new perspectives**
Eveque-Mourroux MR*, Rocha B*, Barré FPY, Heeren RMA, Cillero-Pastor B. Journal of Proteomics. **2020**, 215, 103637.

• **Spatially resolved endogenous improved metabolite detection in human osteoarthritis cartilage by matrix assisted laser desorption ionization mass spectrometry imaging**
Eveque-Mourroux MR, Emans PJ, Zautsen RRM, Boonen A, Heeren RMA, Cillero-Pastor B.
Analyst. **2019**, 144, 5953-5958.

Other publications

• **Comparative label-free proteomic analysis of equine osteochondrotic chondrocytes**
Chiaradia E, Pepe M, Sassi P, Mohren R, Orvietani PL, Paolantoni M, Tognoloni A, Sforna M, Eveque-Mourroux MR, Tombolesi N, Cillero-Pastor B.
Journal of Proteomics. **2020**, 228, 103927

Conferences – oral presentations

• **A multimodal mass spectrometry approach reveals specific cartilage molecular profiles associated to type 2 diabetic patients**
Eveque-Mourroux MR, Emans PJ, Claes BSR, Bouwman FG, Heeren RMA, Cillero-Pastor B.
[Online EULAR 2020].

• **Mass spectrometry imaging on human osteoarthritic cartilage reveals intra-tissue heterogeneity and specific molecular profiles associated to type 2 diabetic patients**
Eveque-Mourroux MR, Emans PJ, Claes BSR, Zautsen RRM, Heeren RMA, Cillero-Pastor B.
[OurCon VII 2019].

• **Mass spectrometry imaging reveals specific lipidomic profiles between osteoarthritis and type 2 diabetes patients**
Eveque-Mourroux MR, Emans PJ, Claes BSR, Heeren RMA, Cillero-Pastor B.
[EORS 2019].

Conferences – poster presentations

• **Specific metabolic association between osteoarthritis and type 2 diabetes revealed by mass spectrometry imaging**
Eveque-Mourroux MR, Emans PJ, Welting TJ, Boonen A, Heeren RMA, Cillero-Pastor B.
Osteoarthr Cartilage. 2018;26:S166-S **[OARSI 2018].**

• **Matrix assisted laser desorption ionization imaging mass spectrometry of human osteoarthritis cartilage reveals the intra-tissue metabolic heterogeneity**
Eveque-Mourroux MR, Emans PJ, Welting TJ, Boonen A, Heeren RMA, Cillero-Pastor B.
[ASMS 2017/EULAR 2017/MSBM 2017].

Other oral and poster presentations

• **Human Hoffa's fat pad lipid profiles as read out of cartilage damage**
Haartmans M, Eveque MR, Eijkel G, Emanuel K, Tuijthof G, Van Rhijn LW, Heeren RM, Emans PJ, Cillero-Pastor B.
[Online poster presentation - EORS 2020].

• Lipid profiles in Hoffa's fat pad as biomarker for cartilage regeneration and osteoarthritis development
Haartmans M, Eveque MR, Emanuel K, Tuijthof G, Heeren RM, Emans PJ, Cillero-Pastor B.
[Online poster presentation - OARSI 2020].

• Lipid profiles in Hoffa's fat pad of osteoarthritic vs osteochondral defect patients
Haartmans MJJ, Cillero-Pastor B, Emanuel KS, Eveque-Mourroux MR, Tuijthof GJ, Heeren RM, Emans PJ.
[Oral presentation - EORS 2019].

• Identifying lipid profiles in Hoffa's fat pad – detect before it melts!
Haartmans MJJ, Cillero-Pastor B, Eveque-Mourroux MR, Emans PJ, Emanuel KS, Heeren RM.
[Poster presentation - MSBM 2019].

• The development of an intraoperative tool based on the assessment of the regenerative capabilities of bone and cartilage using mass spectrometry for the prediction of post-traumatic osteoarthritis (PTOA) and non-unions
Nauta SP, Genangeli M, Van Holten MTE, Eveque-Mourroux MR, Blokhuis TJ, Heeren RMA, Poeze M, Porta T.
[Poster presentation - MSBM 2019].

• Distribution, quantification and effects of triamcinolone acetonide in human osteoarthritic cartilage
Barre FP, Paine M, Flinders B, Eveque-Mourroux MR, Garcia J, Ellis S, Heeren RMA, Creemers L, Cillero-Pastor B.
Osteoarthr Cartilage. 2018;26:S284-S5. **[Poster presentation - OARSI 2018].**

Acknowledgements

Nina, this adventure would not be the same without you. You made my PhD and later on my life much easier to deal with and you deserve to be the first to acknowledge. Thank you for all of the confidence and trust you put on me and on my work. You are the most amazing person I met during these four years and, as a scientist, one of the most dedicated and talented I know. I am really proud of you and I hope you are proud of me. I completed this PhD and I am happy to start a new adventure with you. You are my rock.

Flo, I would like to thank you for several things. First, the call you gave me one Friday evening, to apply for a PhD position here in Maastricht. I trusted you and now here I am, almost a doctor! It was nice working with you on some cartilage projects, especially where your creativity was needed. Second, to all of the fun we had during studying and working together. I remember all these funny Fortnite and Apex moments, the events you created in and out of the lab, and so on! There are so many things we went through, and it is impossible to talk about it all. Please continue spreading your energy and your jokes, as people really need it! Thank you again, and I wish you all the best in the future.

Ron, thank you for everything during these past four years! I remembered the first time we met; It was during my interview and I am still wondering sometimes how you could trust someone with such poor English! But you hired me anyways and now here we are. I dedicate the thesis to you because without you it would not have the same "taste". I appreciate your ideas, enthusiasm and your energy that kept me focused and motivated through all the problems I had along the road. Your optimism (sometimes extreme but always fruitful) was vital for my work but also for me. Your trust made me stronger and more confident. I grew in a really nice and healthy environment here at M4I. You take care of your employees like they were your own family. You have never been a boss, you have always been a leader, the most appreciable quality in your position. I wish you, your family and M4I all the best, with the hope to meet you around in some scientific events.

Berta, you have contributed a lot to make my PhD life easier. You are the most positive person I have ever met. I was working on cartilage using MSI for four years (and you know how difficult it was to stay calm), and despite my positivity, I had my ups and downs. But you were always there. Always there to talk, to smile, to encourage and boost my confidence. You trusted me from the beginning and this thesis is our work, not just mine. You won the best PhD supervisor contest three times in a row and that is not a surprise. It is a reflection of your work with the PhD

students. You are the best and I hope you won't forget the amazing "Frenches" in your cartilage team! Once you go French you can never come back. All the best for you and your family: Teo, Julia and Benny, who are lucky to have you in their lives.

Peter, it was a pleasure to work with you during these four years on this amazing project! As Ron, you were also full of energy and gave me good advice to motivate me through my research. I also remember my scarce visits to the operating room (where I was close to fainting) which were a great experience for me. Your devotion to patients as well as your work are incredible. Thank you again and I wish you good continuation in your work.

Fred, Fredo, the funniest guy at M4I… So many things to tell you! I spent an incredible time with you for the last 4 years! Our "Pause-Choco" at 15.00 everyday with Flo, your skills at the pool table and numerous jokes that make me ''laugh'' every time. We should talk about your "fondu", which was a disaster, or this "blblblblblb" sound that will probably ring a bell. You were always there for me and "tmtc" I can trust you with important things. Stay the way you are. You are a friend that everyone would love to have! I would just like to finish with a word that define you the most, a word that changed my perception about you, a word that show your potential: Maltesers.

Beaaaaaa Rochaaaa! I could not forget my office mate during the first 2 years at M4I! The one who made my PhD life easier. My Bea, it was such a pleasure to come to the office every morning and see your smile. You made my day! I was lucky to have you by my side during my doubts, and a part of this thesis would not be possible without you. I will never forget your "Bouaah" or your pronunciation of the word "syringe", as well as your positive energy! Thanks a lot my Beaaaaa! I wish you all the best in your career in Spain!

Cathy, Claire, I could not have found a better place in my thesis for you. With Bea we can say: We had the best office at M4I, period. It was really cool to spend time with you and have talks about life and work. Thanks again for your kindness. I wish you all the best in your career and hope we can grab a coffee at some point in Maastricht. Take care!

Min, Brenda and Philippe, thanks guys for this time I spent with you in the office. To Min, good luck with your thesis and a lot of success! Brenda & Philippe, I wish you all the best in the near future. I hope you will find your way!

To all of the people I spent most of my time with during the 4 years. The people I will miss the most, and they are not just colleagues (Like Marta would say, ahah). Thanks to all of you, guys: Marty, Tiff, Pmax, Marta, Britt (Thank you sooo much for your help through the paper, the summary and so on!), Naomi, Jianhua Caooooo (冥想是幸福的關鍵), Darya, Fabian (My climbing man), Ana Fonseca Pego (Miguuuuel), Isabeau and Lucia. You were/are the core of M4I! You were my family during this PhD, sharing happiness or doubts, and I grew up with you guys, personally and professionally. I will definitely miss watching P-max running all over the place, listening to Jianhua talking about philosophy of life or hearing the laugh of Britt and Lucia. Take care of you guys and keep spreading your positivity around: You are the best!

M4I is a big scientific family, and all the people have contributed to it: Pieter K, Keely, Silvia, Sylvia, Anton, Lieke, Helen, Mirella, Ronny, Kaj, Eva, Peiliang, Yuandi, Tim, Nils, Alex, Ian, Roel, Christel, Jo, Lennart, Greg, Ali, Gert, Ricky, Klara, Arnoud, Jonah, Rob, Livia, Sylvia, Charles, Stephanie, Saleh, Frans, Michele, Anjusha, Andrew, Shane, Anne, Maarten, Benjamin, Hang, Joel, Bryn(ou), Ian, Maria K, Abril, Axel and everyone else from the department. Thanks for everything, I hope you will find your way after this beautiful adventure at M4I.

I would also thank people from the orthopedic lab on the third floor, especially Tim, Marjolein and Guus. Tim, it was always a pleasure to talk sciences and OA related topics with you. Marjolein and Guus, thank you so much for the amazing work you performed on the project we collaborated on, it was really an exciting adventure. The chapter 5 would not be possible without you.
Thanks also to you, Annelies, for your help and kindness on different projects of this thesis. Your feedback and ideas were always useful to improve my knowledge in the OA field.

Finally, a special mention to Alain Creissen, for your kindness and all your good advice regarding the HTX technology, and to Charlotte Talbot, for the fun we had with Flo and the other Frenches during this PhD adventure. A big thanks also to all my ''roomies'' that I had the chance to live with the past 4 years, especially Lara, Sadie, Lisa and Kevin!

Cette dernière partie est en français et s'adresse particulièrement aux amis de longue date et à la famille.

Les potos, Théo, Paul, Malcolm, Charly, Rité, Lambert, Zinc, Coco, Maurine, Popo et Deuk. Vous n'imaginez pas à quel point vous comptez pour moi. C'est une fierté de

vous connaître et de continuer à partager tous ces bons moments ensemble. Je n'ai pas eu l'occasion de passer beaucoup de temps avec vous ces dernières années, mais promis, on va rattraper ça. Merci de rendre ma vie meilleure. Je peux compter sur vous, et vous pouvez compter sur moi. Prenez soin de vous les louloux!

Alexandre, Pauline. La famille. J'ai la chance de vous avoir comme grand frère et petite sœur. Vous avez toujours été là pour moi et je serai toujours là pour vous. On a toujours été liés et ce n'est pas près de s'arrêter. Merci de faire partie de ma vie, je vous aime! Je n'oublie évidemment pas Morgane et Kévin. Prenez soin de vous et de ma famille.

Les parents, Gitou et JP. Vous avez cru en moi dès le début. Sans vous, rien de tout cela n'aurait été possible. Je ne serai pas là aujourd'hui sans l'éducation que vous m'avez inculquée, sans toutes ces petites choses que vous m'avez apprises sur la vie. Je suis fier de vous avoir comme parents, fier d'avoir grandi dans une famille comme la nôtre. Je vous aime.

À Pépé, qui s'approche tout doucement de la centaine, et à Zoé, qui vient tout juste de pointer le bout de son nez. Bienvenue dans la famille. Ton parrain sera toujours là pour toi.

Papi, Mami, Mémé et tonton Roland, vous me manquez terriblement. Je pense à vous très fort en écrivant ces derniers mots. J'espère que de là-haut, vous êtes fier de moi.

Curriculum Vitae

I was born in Lille, France, on February 8th, 1992.

When I was 20 years old, I obtained a bioengineering diploma and began to work as a laboratory technician in France. Thanks to an opportunity provided by the ERASMUS program, I moved to Norway for three months and worked as an intern to phenotype lactic acid bacteria.

After the internship in Norway, I continued my scientific education by obtaining a bachelor in biology with a focus in biochemistry. After graduation, I worked as a laboratory technician in the mycology department in Lille, France.

After a summer, I joined the proteomics master program in Lille, France, where I learned the mass spectrometry basics and discovered the proteomics field. At the end of the first year of the program, I completed a five-month internship at the Faculty of Medicine in Geneva, Switzerland, in the Science of Human Proteins department, under the supervision of Dr. Annarita Farina. My project was focused on the proteome analysis of ascites and the identification of potential biomarkers for peritoneal carcinomatosis of pancreatic origin. In the second year of the master program, I moved to Grenoble for a six-month internship, where I worked for the French Alternative Energies and Atomic Energy Commission at their large-scale biology laboratory. I was part of the exploration of the dynamics of proteomes team and supervised by Dr. Christophe Masselon. My project was to develop top-down mass spectrometry protocols for the analysis of proteoforms.

After my graduation from the master program, I obtained an engineering position at the Hubert Curien Multi-disciplinary Institute, in the Bioorganic Mass Spectrometry department in Strasbourg. My projects were focused on new data analysis modalities in the mass spectrometry field such as data independent acquisition.

In 2016 I joined the Maastricht MultiModal Molecular Imaging Institute as a PhD student with Ron Heeren and Berta Cillero-Pastor as supervisors. There I researched the development and application of mass spectrometry imaging methods to study the OA disease at the molecular level and for the classification of OA phenotypes as described in this thesis.

Currently I work as a research engineer at the Pasteur Institute of Lille, where my projects focus on Tuberculosis disease.